POLITECNICO DI TORINO

Master's Degree in Biomedical Engineering

Master's Degree Thesis

Development of a wearable Pulse Wave Velocity estimation system using Force Sensing Resistor

Supervisors

Prof. Danilo DEMARCHI

Ph.D. Alessandro SANGINARIO

Ph.D. Irene BURAIOLI

Candidate

Simone MARRELLA

December 2022

Abstract

The main cause of death worldwide is cardiovascular disease (CVD), a group of diseases affecting the heart or blood vessels. The number of deaths from cardiovascular disease is estimated to be around 18 million per year, about 32% of all annual deaths worldwide. The chance of premature mortality due to CVD can be reduced by early disease diagnosis and analysis of several predictive parameters such as arterial stiffness, which is a significant aspect in cardiovascular physiology and is strongly related to Pulse Wave Velocity (PWV).

Pulse Wave Velocity (PWV) is a measure of arterial stiffness and represents the rate at which the blood pressure pulse spreads throughout the circulatory system. PWV is calculated non-invasively as the ratio of the distance and the time required for the pulse to propagate between two sensing sites, which are typically the carotid site and femoral site. Nowadays, PWV estimation is done using expensive technologies such as applanation tonometry and ultrasound, limiting their use in a clinical environment. Furthermore, some operational expertise is required to use applanation tonometry, the most widely used technology in this field, with the potential to influence the measurement as these devices are not wearable.

This thesis aims to develop a clinical low-cost and wearable device for Pulse Wave Velocity estimation. The transducer used in this study is a Force Sensing Resistor (FSR), which is a piezoresistive force sensor that can detect the small force variations caused by artery displacement due to the pulse wave transit. The sensor's response is based on changes in electrical resistance caused by external forces applied to it. Since FSR is a low-cost, flexible, and ultra-thin sensor and can interface with human skin, it is suitable for use in a wearable application such as the one discussed in this thesis.

The characterization of the various FSR product types available on the market and the selection of the best type of sensor for the application comprised the first step of the presented work. A read-out circuit that can pick up and amplify the

signal of interest has been studied and implemented around the chosen sensor. Subsequently, a Printed Circuit Board (PCB) has been realized to significantly reduce the dimension of the device. The PCB, connected to the sensor and encapsulated in a specifically developed holder, interfaces with the Discovery Kit produced by STMicroelectronics, for which a specific firmware has been developed that enables the acquisition and transmission of pulse wave data to the PC. On the PC side, a Graphical User Interface (GUI) has been developed to visualize in real-time the signals taken from the carotid and femoral sites in a user-friendly way and with the possibility of saving data for the subsequent analysis carried out on MATLAB®, implementing the intersecting tangent method for the PWV extraction.

Finally, the system has been validated on 28 volunteer subjects at "A.O.U. Città della Salute e della Scienza di Torino" and statistical analysis has been conducted to compare the obtained results with those provided by SphygmoCor®, the gold standard for PWV estimation. The results obtained showed how the proposed device's performance is consistent with the gold standard as there is a small offset error and a strong correlation that is noticeable with a high coefficient of determination.

Table of Contents

List of Tables

List of Figures

Acronyms

CVD Cardiovascular disease

PWV Pulse Wave Velocity

FSR Force Sensing Resistor

PCB Printed Circuit Board

GUI Graphical User Interface

WHO World Health Organization

NCD Non-communicable disease

MRI Magnetic Resonance Imaging

ATP Adenosine triphosphate

CVS Cardiovascular system

SP Systolic pressure

DP Diastolic pressure

MAP Mean arterial pressure

ECG Electrocardiogram

RBC Red blood cell

WBC White blood cell

AUC Area under curve

PWD Pulse Wave Distance

PTT Pulse Transit Time

MEMS Micro-electro-mechanical systems

ADC Analog-to-digital converter

IC Integrated circuits

I2C Inter-integrated circuit

SPI Serial peripheral interface

USB Universal serial bus

LCD Liquid crystal display

GPIO General purpose Input/Output

IDE Integrated development environment

DC Direct current

AC Alternating current

CAD Computer-aided design

PET Polyethylene terephthalate

SNR Signal-to-noise ratio

MCU Microcontroller unit

FPU Floating point unit

CS Chip select

MOSI Master Out Slave In

MISO Master In Slave Out

SCLK Serial Clock

DI/O Data Input/Output

DIN Data Input

RC Resistor–capacitor

ITP Intersecting tangent point

IIR Infinite impulse response

Chapter 1

Introduction

Worldwide, cardiovascular disease (CVD) is the leading cause of death, according to data from the World Health Organization (WHO), resulting in the deaths of about 18 million people annually, or 32% of all fatalities globally [1].

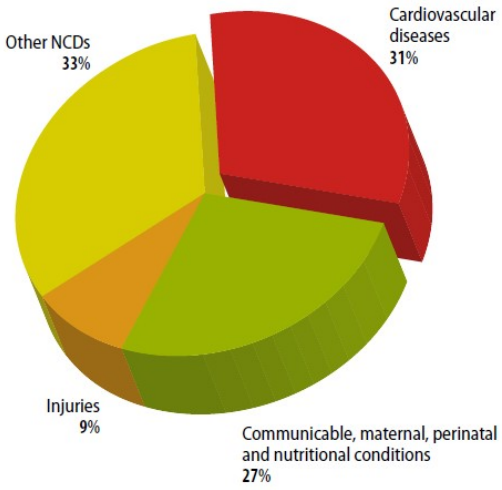

Figure 1.1: Picture of the global distribution of the leading causes of death, including CVDs (NCDs indicate non-communicable diseases) [2].

Heart, vascular, and blood vessel diseases all fall under the category of CVDs. Coronary artery disease, also known as ischemic heart disease (for example, a heart attack), cerebrovascular disease (for example, a stroke), and illnesses of the arteries and aorta are among the conditions specifically caused by atherosclerosis. Cardiomyopathies, congenital heart disease, rheumatic heart disease and cardiac arrhythmias are additional forms of cardiovascular disease [2].

Resulting from aging and population growth, prevalent cases and deaths of

cardiovascular diseases are likely to significantly rise in the upcoming years [3]. The global trend of CVDs has significant implications for clinical practices and healthcare costs. Analyzing the direct costs of cardiovascular disease, adult-related spending in the United States increased by more than $100 billion from 1996 to 2016, reaching a total direct expenditure of $320 billion [4]. In addition, the overall CVD costs are greater than the direct costs of hospitalization and care, since the reduction in income due to the labor force loss and early retirement also need to be considered.

Based on this situation, it is essential to implement practicable and cost-effective strategies for the prevention, early diagnosis and control of disorders and to monitor the outcomes in order to reduce premature mortality and limit other negative effects due to CVD. Early disease diagnosis is feasible thanks to the analysis of some predictive parameters, such as arterial stiffness, which is a significant aspect in cardiovascular physiology and is more widely acknowledged as a significant prognostic indicator and potential therapeutic target in hypertension patients [5]. High blood pressure (hypertension) is one of the risk factors for CVD that is associated with the highest evidence for causation and is the major preventable cause of cardiovascular disorder [6]. A high stiffness of the arterial tree could lead to arterial lesions and cardiac hypertrophy. According to recent studies, arterial stiffness is a reliable predictor of cardiovascular events.

The most established method of evaluating the arterial stiffness is Pulse Wave Velocity (PWV), that represents the rate at which the blood pressure pulse spreads throughout the circulatory system and is closely related to the elastic property of blood vessels. PWV is directly proportional to arterial stiffness, therefore higher velocity is associated with stiffer blood vessel walls. PWV is calculated as the ratio of the distance and time required for the pulse to propagate between two sites, which are typically the carotid and femoral sites.

Nowadays, PWV estimation is performed using expensive technologies such as applanation tonometry, photoplethysmography, ultrasound and Magnetic Resonance Imaging (MRI) and this has limited their use in a clinical environment [7]. Furthermore, some operational expertise is required to use applanation tonometry, the most widely used technology in this field, with the potential to influence the measurement as these devices are not wearable.

The aim of this thesis is the development of a clinical low-cost and wearable device for Pulse Wave Velocity estimation. The transducer used in this study is a Force Sensing Resistor (FSR), which is a piezoresistive force sensor suitable for biomedical applications since it can be applied to the skin close to a blood vessel and can detect the slight force variations brought on by artery displacement as a result of the pulse wave transit. The sensor's response is based on changes in electrical resistance caused by external forces applied to it. Since FSR is a low-cost, flexible, and ultra-thin sensor and can interface with human skin, it is suitable for

use in a wearable application such as the one discussed in this thesis.

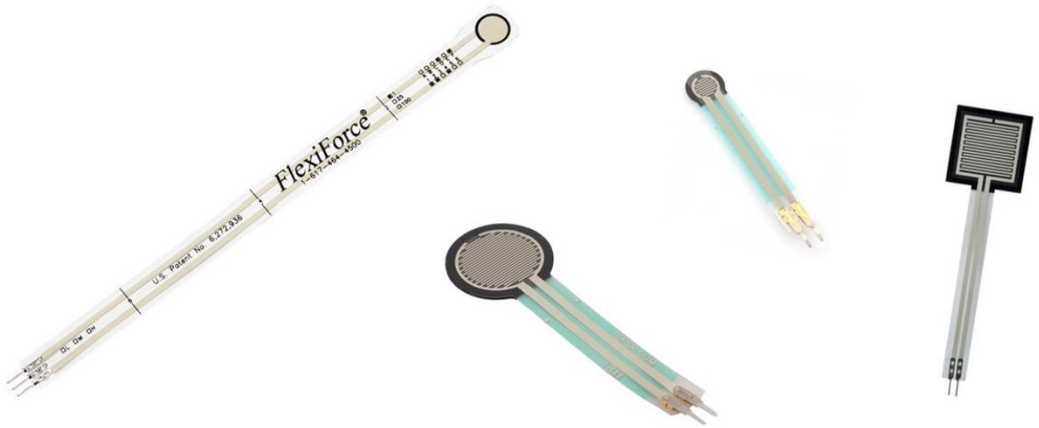

Figure 1.2: Different types of Force Sensing Resistor (FSR) on the market.

The characterization of the various FSR product types available on the market and the selection of the best type of sensor for the application comprised the first step of the presented work. A read-out circuit that can pick up and amplify the signal of interest has been studied and implemented around the chosen sensor. Subsequently, a Printed Circuit Board (PCB) has been realized to significantly reduce the dimension of the device. The PCB, connected to the sensor and encapsulated in a specifically developed holder, interfaces with the Discovery Kit STM32F429I produced by STMicroelectronics, for which a specific firmware has been developed that enables the acquisition and transmission of pulse wave data to the PC. On the PC side, a Graphical User Interface (GUI) has been developed to visualize in real-time the signals taken from the carotid and femoral sites in a user-friendly way and with the possibility of saving data for the subsequent analysis carried out on MATLAB®, implementing the intersecting tangent method for the PWV extraction.

Finally, the system has been validated on 28 volunteer subjects at "A.O.U. Città della Salute e della Scienza di Torino" and statistical analysis has been conducted to compare the obtained results with those provided by SphygmoCor®, the gold standard for PWV estimation. The results obtained showed how the proposed device's performance is consistent with the gold standard as there is a small offset error and a strong correlation that is noticeable with a high coefficient of determination.

Chapter 2

Background

This section provides a physiological background of the cardiovascular system and Pulse Wave Velocity. In addition, an overview of the PWV estimation technology currently available on the market is made and all the devices and software used during the thesis are described.

2.1 Cardiovascular system

The cardiovascular system, also known as the circulatory system, is a group of organs that consists of the heart, a muscular pump, blood vessels, channels through which the blood can flow, and blood, a fluid that travels throughout the body and enables the transport and exchange of nutrients, particularly oxygen, with the cells. The driving force behind blood's circulation through blood vessels is provided by the heart, which pressurizes blood.

The circulatory system is crucial because it delivers the oxygen and nutrients cells need to produce ATP while also transporting waste materials and carbon dioxide, removing them from organ systems and allowing them to be eliminated from the body. These nutrients and wastes must be transferred between the cells and the surrounding environment using a variety of exchange processes, such as capillary diffusion. [8]. Diffusion takes place when there is a concentration gradient and is a passive transport mechanism since it is fueled by the fast thermal motion of molecules rather than metabolic pumps. While diffusive transport is extremely slow over long distances, it is extremely quick over short distances. For example, the short distance between gas and blood in the pulmonary alveoli is traversed through diffusion. Absorbed O_2 needs to be carried rapidly throughout the body and this is done by moving along a stream of pumped fluid, covering a large distance in a

few seconds. This form of transport is called convective transport and it is one of the most important functions of CVS.

Therefore, the cardiovascular system serves three primary purposes, which are described below [8]:

- The fast *convective transport* of oxygen, vitamins, glucose, amino acids, drugs, fatty acids and water to the organs and tissues in addition to the fast removal of metabolic waste products such as carbon dioxide, urea and creatinine from the tissues.

- The *control system* action that works by secreting bioactive substances (natriuretic peptides, renin, nitric oxide, endothelin, prostaglandins) and distributing hormones to the tissues.

- The *homeostasis maintenance* and body temperature regulation. Homeostasis is the body's propensity to maintain all internal biological parameters constant while it responds to external changes in the environment and it is a fundamental mechanism for the self-regulation of the organism.

Through the course of the body, blood essentially moves in a circular motion. The two divisions of this circular path of the circulatory system are the pulmonary circulation, which comprises all blood vessels within the lungs and those connecting the lungs to the heart, and the systemic circulation, which comprises blood vessels connecting the heart to all body tissues. Different sides of the heart supply blood to the two divisions. While the right heart pumps deoxygenated blood to the lungs, the left heart pumps oxygenated blood to the body's tissues.

The pulmonary and systemic circuits carry out convective transport and allow the blood to be transported over long distances, while the transfer of materials between interstitial fluid of tissues and blood through diffusion takes place in the microcirculation, consisting of a dense network of capillaries.

As oxygen (O_2) enters the blood from the lungs' air in the pulmonary microcirculation, carbon dioxide (CO_2) leaves the blood. The blood is referred to as oxygenated blood because it is relatively rich in oxygen when it leaves pulmonary capillaries. With the exception of the lungs, all organs and tissues contain the systemic circuit's capillary beds. Because the cells in the organs and tissues need oxygen and produce carbon dioxide, as the blood passes through systemic capillaries, oxygen is released and carbon dioxide is picked up. Blood leaving the systemic capillaries is known as deoxygenated blood because it contains very little oxygen [9]. Thus, while the right heart pumps deoxygenated blood to the pulmonary circuit, the left heart pumps oxygenated blood to the systemic circuit and blood from one side of the heart never combines with blood from the other side.

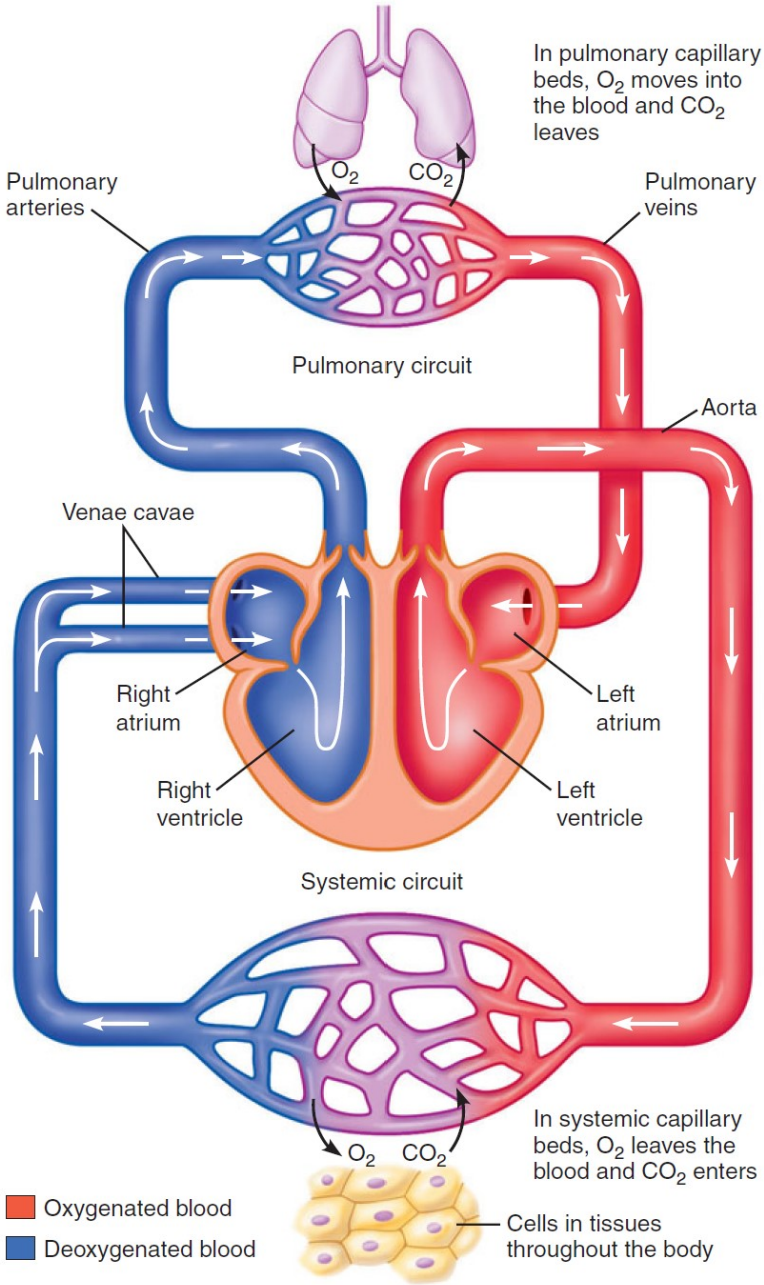

Figure 2.1: Blood's path through the cardiovascular system [9].

In the next sections, the main parts of the cardiovascular system are explored, which has been described in a general way previously.

2.1.1 Heart

The heart is a striated muscular organ placed behind and slightly to the left of the sternum, in the center of the thoracic cavity, between the lungs and above the diaphragm. The heart's objective is to produce the necessary force to push blood through blood vessels. The heart is divided into four chambers: two upper chambers, known as the atria, receive blood returning to the heart from the vascular system, and two lower chambers, known as the ventricles, receive blood from the upper chambers and produce the force necessary to push the blood through the vascular system and away from the heart [8].

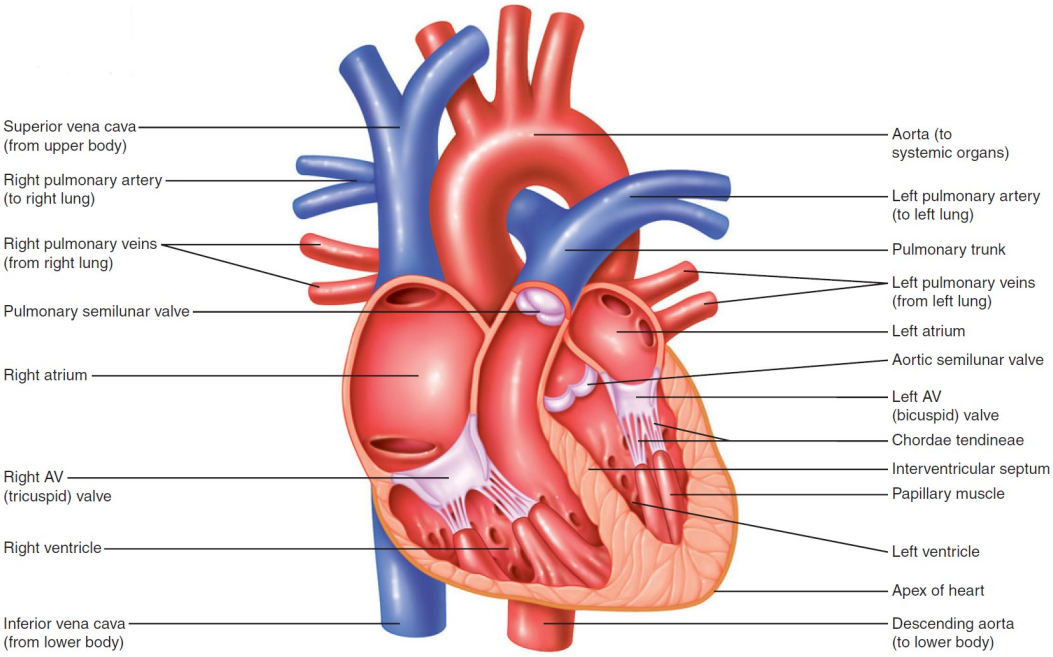

Figure 2.2: Section of the heart and its anatomy [9].

The heart wall consists of three layers. Starting from the inside, there is a layer of epithelial cells called the endothelium, while the middle layer is made up of cardiac muscle tissue and is called the myocardium. The protective outer layer of connective tissue is called the epicardium. A pericardium, a membrane sac that surrounds the cardiac muscle and contains pericardial fluid to lubricate the organ, surrounds the cardiac muscle. The rhythmic relaxation and contraction of the myocardium contribute to the heart's pumping action. The wall's ability to contract causes it to move inward and squeeze the blood within an atrial or ventricle. This tightening pushes the blood out of the chamber by raising internal pressure. The chamber enlarges and filled with blood when the muscle relaxes. Because the left ventricle pumps blood to all body organs except the lungs and the

right ventricle only pumps blood to the lungs, the thicker left heart muscle enables the left ventricle to generate more pressure than the right ventricle.

The heart can be divided into left and right functional halves: the left and right hearts are respectively made up of the left atrium and ventricle and the right atrium and ventricle. The septum, a muscular structure that divides the two sides of the heart, keeps blood from the left and right heart from mixing. The interventricular septum divides the left and right ventricles and the interatrial septum is the region that divides the left and right atria. In addition, an atrioventricular septum separates the ventricles from the atria.

Four valves cooperate to ensure proper blood flow through the heart and prevent backflow. Every heartbeat produces cyclic variations in pressure, which cause valves to passively open or close. The heart valves are as follows:

- *Atrioventricular valves* (AV valves), which on either side of the heart divide the atrium from the ventricle and allow blood to flow from the upper chambers to the lower chambers but not the other way around. The valves open when atrial pressure exceeds ventricular pressure, and they close when ventricular pressure exceeds atrial pressure. Because it is made up of two flaps or cusps of connective tissue, the left AV valve is known as the bicuspid valve or also the mitral valve. Instead, as regards the right AV valve, since it is made up of three cusps, it is called the tricuspid valve.

- *Semilunar valves*, which are situated in the middle of the arteries and ventricles. The pulmonary valve is situated between the right ventricle and the pulmonary blood arteries, whereas the aortic valve is situated between the left ventricle and the aorta. When ventricular pressure exceeds arterial pressure, which occurs when the ventricles contract and allow blood to flow from the ventricles into the arteries, the aortic and pulmonary valves open. When the ventricles relax and the ventricular pressure falls below the arterial pressure, the valves close to stop the flow of blood from the arteries back into the ventricles.

First, oxygenated blood leaves the left ventricle through the aortic valve and gets into the aorta, the main artery of the body, and from there it divides through the arteries to the capillary beds of all organs and tissues of the systemic circuit. Deoxygenated blood from capillaries is transported by the vena cavae up to the right atrium of the heart. Blood from the right atrium enters the right ventricle via the tricuspid valve. From the right ventricle, blood is propelled into the pulmonary circuit through the pulmonary semilunar valve, and from here the path immediately forks into the pulmonary arteries which carry deoxygenated blood to the lungs. The pulmonary veins carry blood to the left atrium after it has been oxygenated in the lungs. Finally, the bicuspid valve allows blood to pass through the left atrium into the left ventricle, where the blood starts its circular cycle again.

Cardiac cycle

The cardiac cycle is an organized, time-related series of electrical, mechanical, and valvular events that take place with heart contraction and relaxation [10]. Systole, which is represented by ventricular contraction, and diastole, which is represented by ventricular relaxation, are the two main stages of the cardiac cycle [11]. The entire cycle, starting from the middle of diastole, is divided into several phases:

1. *Ventricular filling* is the stage at which blood flows into the ventricles. In the course of diastole, blood gets into the relaxed atria via the pulmonary and systemic veins and then moves into the ventricles passing through the AV valves. When the pressure in the veins is greater than that in the atria, blood returns from the veins to the heart, a process known as venous return. Additionally, because ventricular pressure is lower than that of the aorta and pulmonary arteries, the pulmonary and aortic valves are closed. At the end of diastole, the atria constrict, increasing blood flow to the ventricles, and then quickly relax. Once the ventricles have been filled, systole starts.

2. *Isovolumetric contraction* is the phase where the ventricles contract with a constant blood volume. The ventricles constrict during the start of systole, increasing the pressure inside of them. Early in the systole, when the ventricular pressure exceeds the atrial pressure, the AV valves close. The semilunar valves remain closed because ventricular pressure is not yet high enough to force them open. Thus, at this stage none of the valves are open, preventing blood from entering or leaving the ventricles; the amount of blood inside the ventricles stays constant even when they are contracting. The end of this stage occurs when the semilunar valves are forced open by the ventricular pressure, allowing blood to exit the ventricles.

3. *Ventricular ejection* is the stage in which the ventricular volume decreases as blood passes through the open semilunar valves into the pulmonary trunk and aorta. It stands in for the remaining systole. A pressure peak and subsequent decrease occur as blood leaves the ventricles. Later, when the ventricular pressure drops below the aortic pressure, the semilunar valves close, interrupting ejection and ending the systole.

4. *Isovolumetric relaxation* is the stage in which the heart muscle relaxes and the diastole restarts. At this stage, there is still a small amount of blood inside the ventricles as it takes a short time for the tension in the ventricular muscle to ease. Specifically, ventricular pressure is both too high to allow the AV valves to open and too low to keep the semilunar valves open. This phase is referred to as isovolumic relaxation because all valves are closed and the blood volume within the relaxing ventricles stays constant. Blood enters the

ventricles from the atria after the ventricular pressure drops below the atrial pressure, allowing the AV valves to reopen. From this point, the cardiac cycle is restarted.

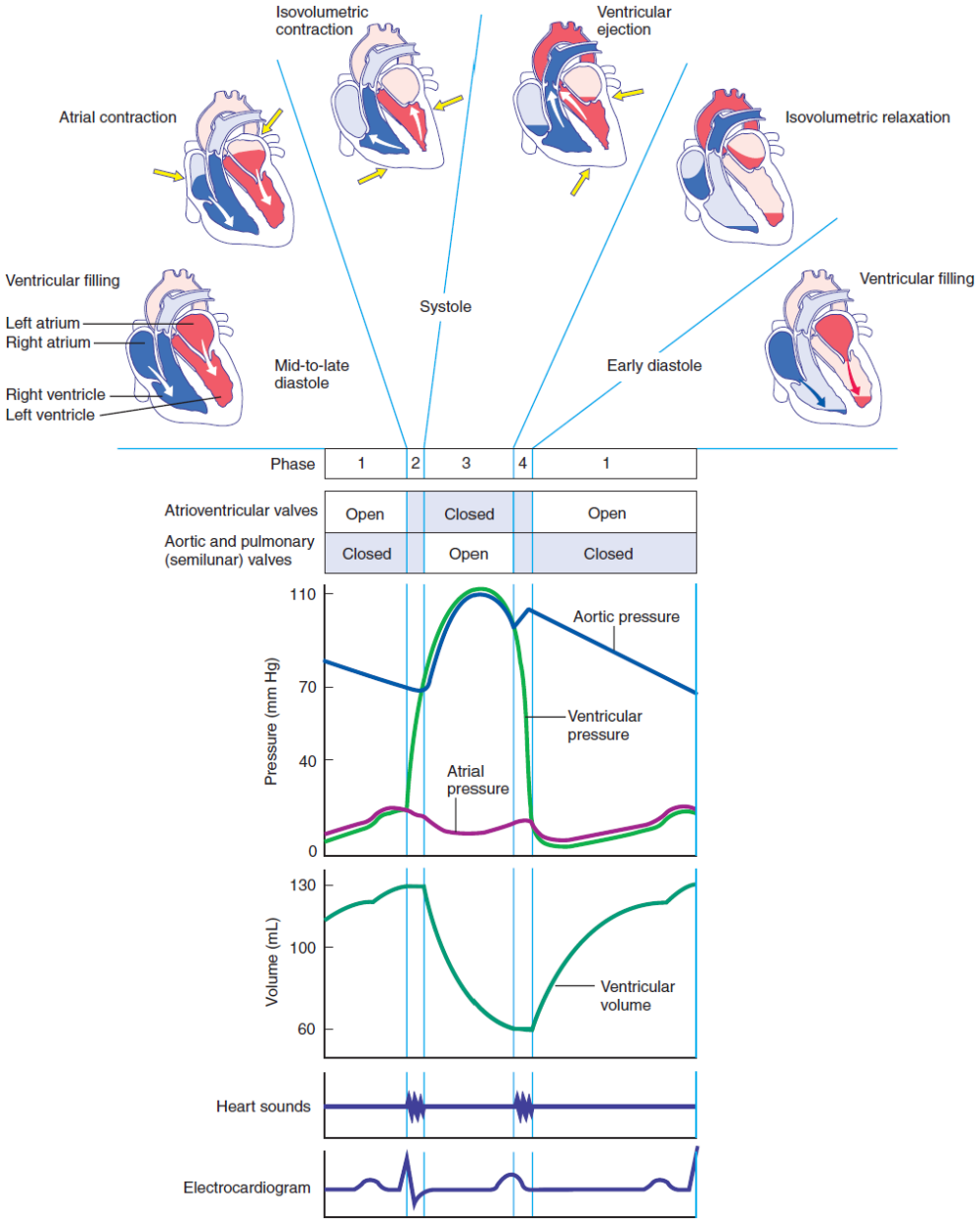

Figure 2.3: The cardiac cycle is shown, with its values in relation to the left heart. Heart sounds are related to the closing of the valves, and the mechanical functions of the heart are related to ECG waves [9].

The duration of systole and diastole for a heart beating at its average resting rate of about 72 beats per minute, or one beat every 0.8 seconds, is not equal. Diastole takes up roughly 65% of the cardiac cycle, or 0.5 seconds, and systole takes up the remaining 35%, or roughly 0.3 seconds. This gives the heart more time to fill with blood during diastole, which is crucial for efficient pumping. Furthermore, due to the longer duration of diastole compared to systole, the heart muscle has more time to relax, preventing muscle fatigue.

Ventricular pressure is very low during diastole and remains that way until the end of the phase, when it suddenly rises slightly. Atrial contraction, which increases the amount of blood in the ventricle, causes this increase. Shortly after, there is a noticeably larger rise in pressure indicative of ventricular systole. The pressure decreases to almost zero during early ventricular diastole, reflecting the myocardium's relaxation. Ventricular pressure gradually increases during the remainder of diastole as passive filling of the ventricle with blood returning from the pulmonary circulation occurs. In the late distole phase, atrial contraction begins with a consequent increase in atrial pressure. The pressure trend of the heart chambers is shown in the Figure 2.4a.

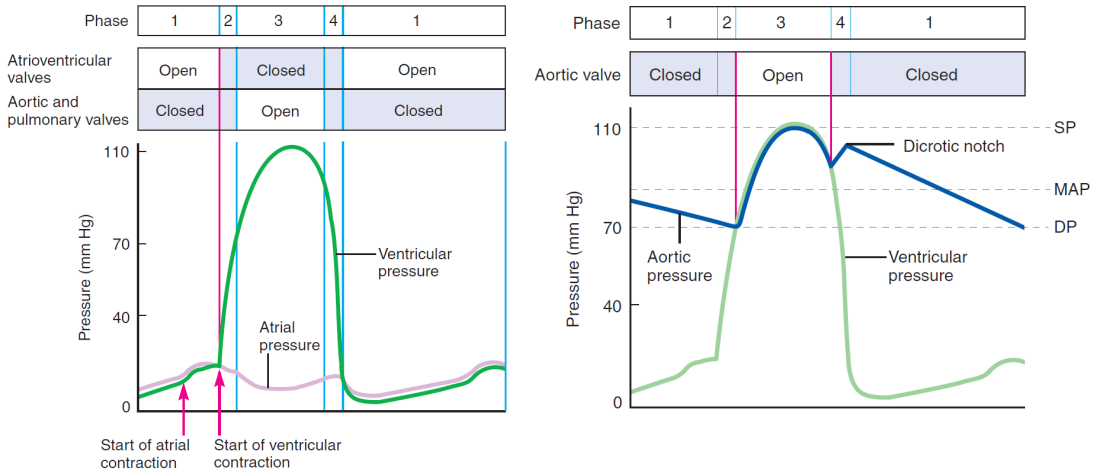

(a) Atrial and ventricular pressure

(b) Aortic pressure

Figure 2.4: The atrial, ventricular, and aortic pressures of the cardiac cycle are shown [9]. Systolic pressure (SP) represents the highest pressure during the cardiac cycle, while diastolic pressure (DP) is the lowest pressure in the aorta. Mean arterial pressure (MAP) represents the average pressure throughout the cardiac cycle.

During the diastole phase no more blood enters the aorta as the aortic semilunar valve is closed and this strongly influences the aortic pressure. However, the

systemic circuit's blood vessels downstream allow blood to leave the aorta, thus the amount of blood in the aorta decreases as a result of this continuous blood flow during diastole, which results in a gradual drop in aortic pressure (Figure 2.4b). The diastolic pressure (DP) is the lowest point of this fall in aortic pressure. Until the next onset of the systolic period, identified by the opening of the aortic valve caused by ventricular pressure being high enough to open it, the aortic pressure continues to decrease. As the aortic valve opens and the ejection stage starts, aortic pressure rises rapidly. The blood entering the aorta more quickly than it can be expelled is what causes this rise in pressure. Nevertheless, the rate of blood flow that exits the heart rapidly begins to slow down. The aortic pressure reflects this state by not continuing to climb but rather reaching a maximum, known as the systolic pressure (SP), and then beginning to descend. The dicrotic notch denotes the moment the aortic valve closes after systole, stopping blood flow from the heart into the aorta.

Because the aorta has the capacity to store pressure during systole and release it during diastole, aortic pressure is higher than ventricular pressure during diastole. The aorta grows and its wall stretches during ejection as the amount of blood it can hold increases. The aorta stores part of the energy generated by the contraction of the heart thanks to the increase in pressure. The heart no longer actively produces pressure during distole, but since the aorta has stored energy due to the stretch of the elastic tissue in its walls, the artery still pushes the flow forward and gradually decreases the pressure inside it. As blood leaves the aorta and the pressure drops, the wall contracts and, as a result, the aorta releases the energy it stored during systole. During diastole, this energy propels blood through downstream arteries. Therefore, even though no blood is being expelled from the heart during diastole, blood still flows through the vasculature. As a consequence, even though blood exits the heart intermittently during the cardiac cycle, it circulates through the vascular system more or less continuously.

Cardiac electrical activity

The cardiac electrical activity coordinates the contraction of the heart chambers and controls the pumping function and its timing [12]. A complex conduction system that controls the timing of cardiac muscle cell activation regulates how the heart contracts. Impulses produced within the cardiac muscle cause contractions to begin. The activity of the heart is autorhythmic due to the action of a small number of cardiac cells known as autorhythmic cells, which produce little or no contractile force but are essential as they provide rhythm to the heartbeat by depolarizing the heart tissue in a coordinated manner, allowing thus to make the heart carry out the pumping action.

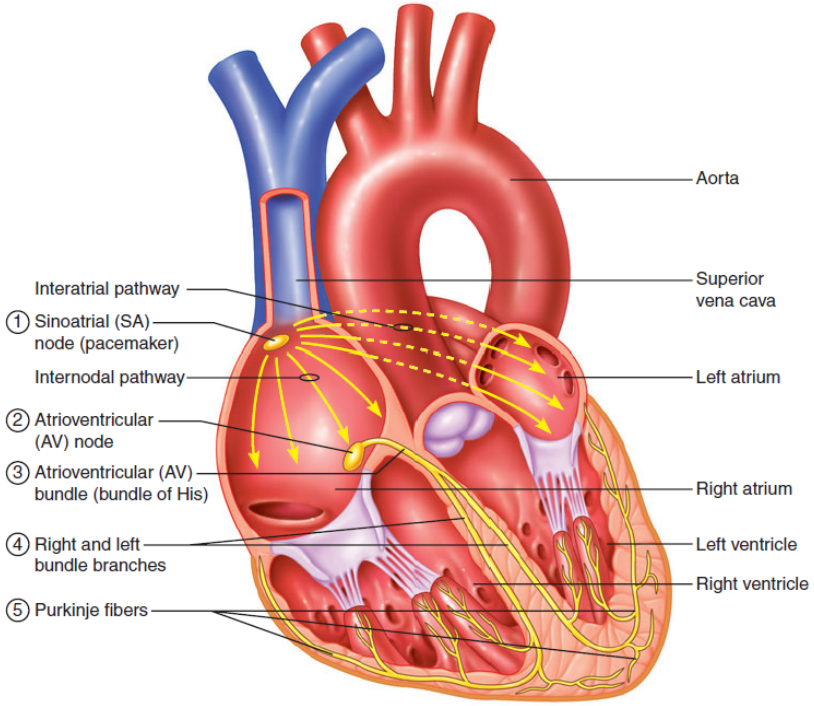

Figure 2.5: The heart's conduction system [9].

The two different types of autorhythmic cells combine to form the heart's conduction pathway. The autorhythmic cells types are the following:

- *Pacemaker cells*, which regulate the heartbeat generating spontaneously action potentials. The two regions of the myocardium where this cell type is primarily concentrated are the sinoatrial node (SA node), located in the right upper atrial wall near where the heart connects with the superior vena cava, and the atrioventricular node (AV node), located near the tricuspid valve in the atrial septum. Action potentials are produced by the SA node and AV node cells at various rates. The SA node manages and coordinates the depolarization of the cells of the AV node and of the whole heart, establishing the heart rhythm. The SA node leads the AV node as the two regions are connected by specific conducting fibers. The pacemaker cells of the SA node have a faster intrinsic rate of spontaneous depolarization than that of the AV node and therefore govern them. The sinoatrial node, therefore, acts as the heart's pacemaker.

- *Conduction fibers* are the fibers that transfer action potentials in a highly coordinated manner through the heart. These fibers are efficient at swiftly delivering action potentials produced by pacemaker cells through the myocardium, inducing contractions of the heart muscle. Conduction fiber systems known

as internodal pathways carry electrical impulses from the SA node to the AV node through the atria's walls. As these signals move through the internodal pathways, they also spread through the atrial muscle by way of interatrial pathways. The impulse passes from the AV node through the atrioventricular bundle, also known as the bundle of His, which is a compact bundle of muscle fibers placed in the interventricular septum. In order to send impulses to the left and right ventricles, the signal splits into left and right bundle branches. From the bundle branches, impulses flow through a vast network of branches known as Purkinje fibers, which extend through the ventricular myocardium from the apex onward toward the valves. In this way, the depolarization of the heart muscle cells of the ventricles occurs.

Electrocardiogram

The electrocardiogram (ECG) is a non-invasive clinical method for measuring the electrical activity of the heart, which in turn is related to its expression of mechanical activity [13]. The ECG is a record of how the electrical current flows through the heart and how is temporized during the cardiac cycle. Due to the highly coordinated electrical activity of the heart, very large amplitude electrical potentials corresponding to different electrical phases of the heart can be measured on the surface using electrodes placed on the skin.

A hypothetical, equilateral triangle that surrounds the heart serves as the base for the typical ECG procedure. The shape created by stretching the triangle until its corners touch the left leg, left arm and right arm is known as Einthoven's triangle. Pairs of electrodes put on the skin at the triangle's corners are connected to voltage-measuring equipment and this allows measuring the tracing of the surface electrical potential generated by the depolarization and repolarization of the heart. Each pair of electrodes offers an alternative electrical representation of the cardiac muscle, although all traces have the same fundamental waveforms. The basic waveforms are as follows:

- *P wave*, which is a slope upward that results from atrial depolarization.
- *QRS complex*, which consists of several abrupt upward and downward deflections brought on by ventricular depolarization. Due to the fact that it happens concurrently with the QRS complex, atrial repolarization is typically not picked up in an ECG recording.
- *T wave*, which is a slope upward that results from ventricular repolarization.

A typical ECG tracing also has a horizontal line between the waves that is known as the isoelectric line and shows that there are no changes in electrical activity.

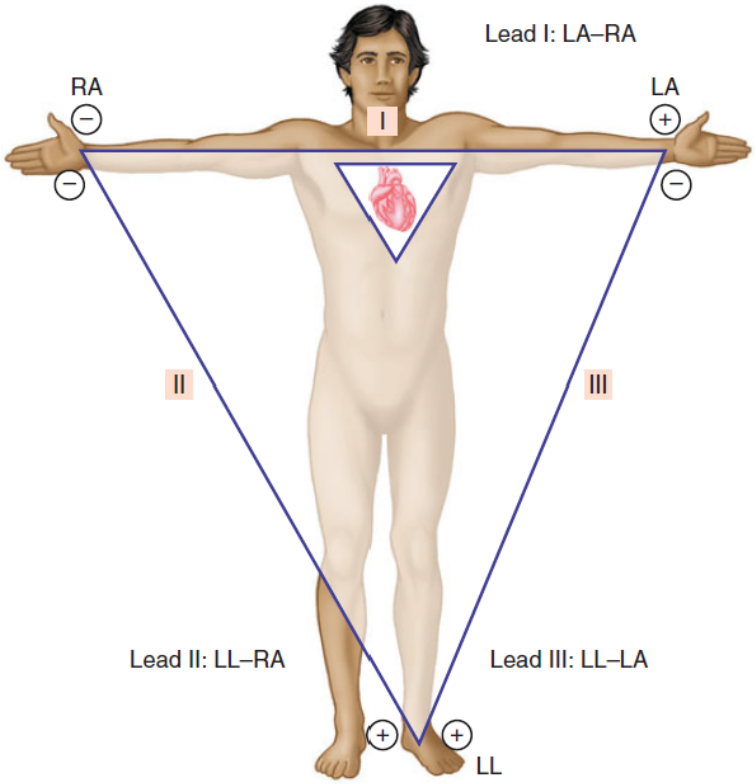

Figure 2.6: Einthoven's triangle.

Waves amplitude and length are important indicators for identifying cardiovascular disorders. Along with waves, specific timespan and segment ranges can reveal crucial details about the heart's functioning. The main intervals that can be found in an ECG trace are:

- *P-Q interval*, which is the interval that measure the time of conduction to the AV node, identified between the P wave and the beginning of the QRS complex.
- *Q-T interval*, which corresponds to ventricular systole and is defined as the time interval between the start of the QRS complex and the termination of the T wave.
- *T-Q interval*, which corresponds to ventricular diastole and referred to as the time segment between the end of the T wave and the beginning of the QRS complex.
- *R-R interval*, which represents the time interval between the peaks of two succeeding QRS complexes. It represents the duration of the cardiac cycle.

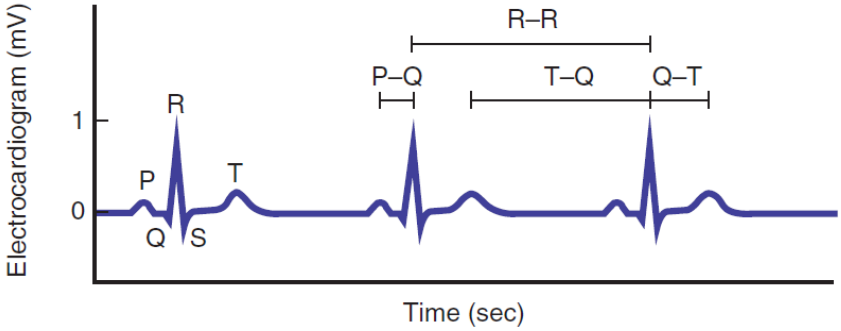

Figure 2.7: Capturing of a typical lead II ECG [9].

By analyzing the duration of the waveforms and the intervals found in an ECG trace, the health of the heart muscle can be established. The following are the standard values for a healthy heart:

Components	Duration (s)
P wave	0.10
QRS complex	0.08 - 0.12
T wave	0.16 - 0.27
P-Q interval	0.12 - 0.21
Q-T interval	0.30 - 0.43
T-Q interval	0.55 - 0.70
R-R interval	0.85 - 1.00

Table 2.1: Duration of the waveforms and intervals of the cardiac cycle for a healthy heart [9].

2.1.2 Blood vessels

The circulatory system's blood flow is governed by the same basic physical laws that govern the flow of any fluid through a network of pipes because the body's circulatory system resembles an intricate network of pipes. According to the fundamental law of fluids, the volume of liquid flowing through a pipe per unit of time, or flow rate (ΔQ) is the ratio between pressure gradient (ΔP), the difference in pressure between the two ends of the pipe, and the pipe's resistance (R):

$$\Delta Q = \frac{\Delta P}{R} \tag{2.1}$$

ΔP is the driving force that causes a liquid to flow through a pipe when pressure changes from high to low. The resistance R is a measurement of the multiple factors that prevent liquid from flowing freely through a pipe. In the circulatory system, the pressure gradient between the arteries and veins is generated by the heart which pumps blood in the arteries and, therefore, generates the increase in mean arterial pressure (MAP). This gradient is what drives blood flow through the vasculature.

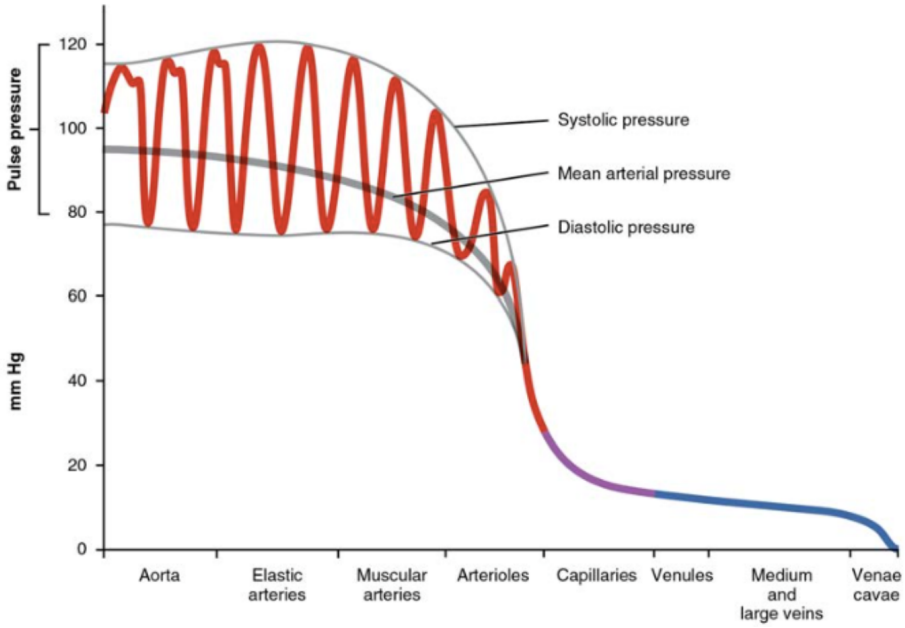

Figure 2.8: The figure shows the systolic pressure (SP), the diastolic pressure (DP), the driving force of the circulatory system which corresponds to the mean arterial pressure (MAP), and, finally, the difference between the systolic pressure and the diastolic pressure, which is called pulse pressure [14]. Systolic pressure on diastolic pressure, which for a healthy patient is approximately 110/70 (SP/DP), is a common way to measure blood pressure in clinical practice.

Both the physical characteristics of the blood vessels and the properties of the fluid that passes through them, specifically, the radius and length of the tube and the fluid's viscosity, have an impact on resistance R. Poiseuille's law explains how these factors affect blood flow [15]:

$$R = \frac{8L\eta}{\pi r^4} \tag{2.2}$$

In Equation 2.2, L is the length of the tube, r is the tube's internal radius and η is the viscosity of the fluid. It is clear that the blood vessel's internal diameter

has a significant impact on the resistance, but more generally the blood flow is strongly influenced by the anatomy of the blood vessels and their characteristics.

Blood vessels are divided into groups based on their size and whether or not they deliver blood to the heart. Blood is transported from the heart to the capillaries through the arteries and smaller arterioles, where gaseous exchange takes place with the interstitial fluid and is subsequently drained from the venules before entering the larger veins, which return blood to the heart. The microcirculation is made up of venules, capillaries, and arterioles.

The lumen, a hollow interior where blood flows, is present in all blood vessels. The endothelium, a layer of epithelium, lines the lumen of all blood vessels. The wall that surrounds the lumen varies in composition and thickness depending on the kind of vessel. A layer of endothelial cells and a basement membrane make up the tiniest blood vessels, called capillaries. The proportions of connective tissue and smooth muscle, the two layers responsible for the vessels' elasticity and stiffness, in the walls of all other blood vessels vary. The structure of blood vessels is therefore comprised of the endothelium layer, smooth muscle, and outer layer of connective tissue.

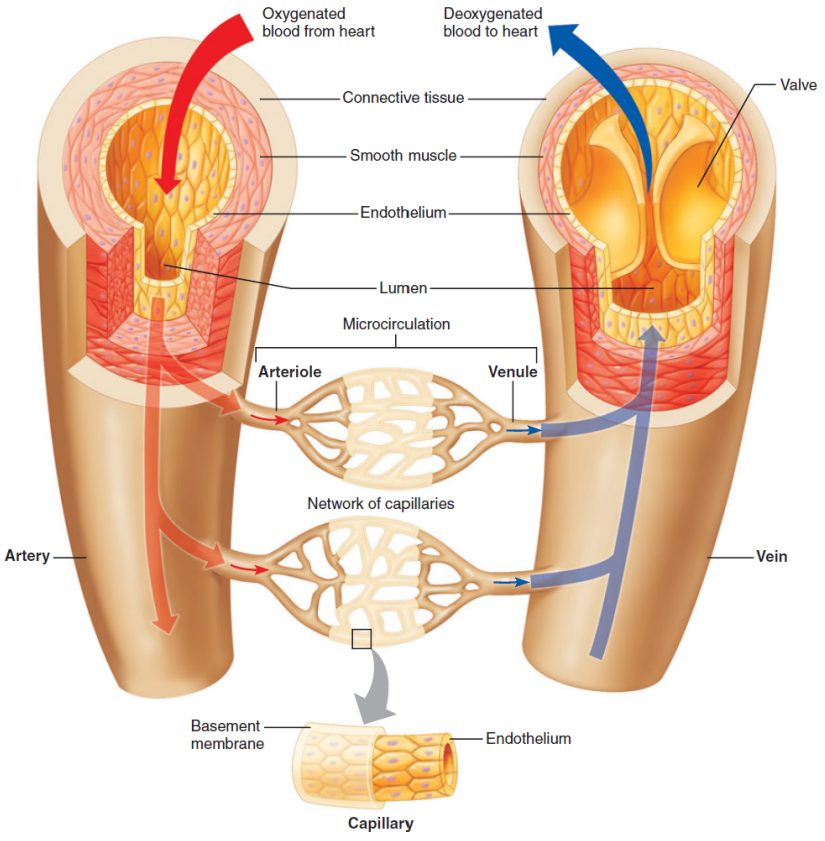

Figure 2.9: Overview of vasculature anatomy [9].

The five categories of blood vessels therefore differ in internal diameter and wall thickness:

Vessel	Average internal diameter (mm)	Average wall thickness (mm)
Arteries	4.0	1.0
Arterioles	0.03	0.006
Capillaries	0.008	0.0005
Venules	0.02	0.001
Veins	5.0	0.5

Table 2.2: The blood vessels' internal diameter and wall thickness.

The wall of arterioles is composed primarily of smooth muscle and little elastic tissue. This musculature's presence enables the vessel's diameter to be changed during contraction, modifying the flow resistance. Vasoconstriction and vasodilation are regulated by this mechanism.

Arteries, on the other hand, have a much larger internal diameter than arterioles and a stronger outer wall. The aorta, the largest artery in the human body, has a wall thickness of 2 mm and a diameter of 12.5 mm. The large diameter of arteries provides very little resistance, and the fibrous and elastic connective layers enable them to endure the high internal pressures that occur. The elastin fibers of the elastic connective tissue act like springs, storing energy during systole and releasing it during diastole, pushing the previously stored blood forward. The pressure wave produced by the blood pushed during the systole, which results in the expansion of the vessel walls, is what creates the arterial pulse that is felt by palpating the arteries. Compliance is defined as the volume of the vessels changing in response to an increase in pressure [16]:

$$Compliance = \frac{\Delta V}{\Delta(P_{inside} - P_{outside})} \tag{2.3}$$

In Equation 2.3, P_{inside} and $P_{outside}$ represent the pressures inside and outside the vessel, while ΔV represents the change in blood volume. When the pressure inside the vessel is greater than the pressure outside, a force acting outward acts on the wall and promotes its expansion. On the other hand, when the internal pressure is reduced, a force is produced that is directed inside and encourages shrinkage. Because arteries have low compliance, a small increase in volume results in a modest expansion, which is accompanied by a large variation in pressure when blood is injected into the vessel during the systole. Their low compliance is a result of the high elasticity and anatomical characteristics of the walls.

Given the elasticity, low compliance and high-pressure difference generated during systole in the arteries, it is possible to sense the arterial pulse in arterial sites of the human body.

2.1.3 Blood

In the circulatory systems of humans and other vertebrates, blood is a bodily fluid that transports nutrients and oxygen to the cells as well as metabolic waste products away from the cells. The preservation of homeostasis is another function it plays [17]. According to anatomy and histology, blood is a specific type of connective tissue. It is made up of cells and cell fragments suspended in a complex extracellular matrix. Blood is remarkable in that it is a fluid connective tissue since the extracellular matrix is fluid. Its composition always changes as it travels through the capillaries as a result of interactions with the interstitial fluid.

The blood is made up of two distinct components that can be separated by centrifugation:

- *Plasma*, which is the liquid phase of blood and constitutes 55% of blood fluid. It is an aqueous solution that contains a wide range of dissolved solutes, including proteins, micronutrients such as glucose, lipids and amino acids, metabolic waste products such as urea and lactic acid, gases such as oxygen, carbon dioxide and nitrogen, electrolytes such as sodium, potassium and chloride and hormones. Due to the similarities in composition between plasma and interstitial fluid, small solutes can be exchanged by concentration gradients across highly permeable capillary walls.

- *Erythrocytes, leukocytes and platelets*, which make up the solid phase of blood and are cells and cell-derived components. They constitute 45% of blood fluid. The majority of the blood's cells are erythrocytes, also referred to as red blood cells (RBCs) and they enable the body's organs and tissues to exchange gases by providing oxygen and absorbing carbon dioxide. RBCs are biconcave disk-shaped and anucleate and this unique form makes it easier for gas exchanges with cells. White blood cells (WBCs), also referred to as leukocytes, are an essential part of the immune system and aid in the body's defense. They are in charge of eliminating infectious pathogens and secreting elements like antibodies. Platelets or thrombocytes are engaged in the blood clotting process, enabling quick treatment for lesions and injuries. They stick to the incision and collect into clots that block the wound. They also release chemicals that attract coagulation factors and encourage the aggregation of additional platelets.

2.2 Cardiovascular disease (CVD)

Heart and blood vessel diseases all fall under the category of cardiovascular disease (CVDs). About 18 million people die from CVDs each year, making them the world's top cause of mortality with about 32% of all global deaths [2].

Two categories are used to classify the various CVDs:

- *CVDs due to atherosclerosis*, which are cerebrovascular disease (e.g. stroke), ischaemic heart disease or coronary artery disease (e.g. heart attack) and diseases of the aorta and arteries.
- *Other CVDs*, such as cardiomyopathies, congenital heart disease, cardiac arrhythmias and rheumatic heart disease.

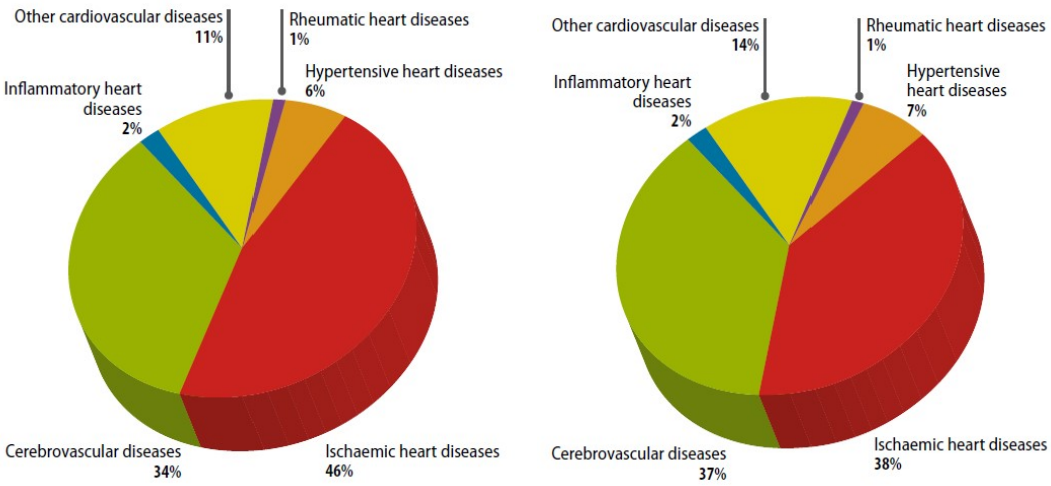

(a) Male **(b)** Female

Figure 2.10: Distribution of CVD deaths [2].

Atherosclerosis is the underlying blood vessel disease process that causes cerebrovascular disease (stroke) and coronary heart disease (heart attack). It is a complex degenerative process that affects the blood artery walls over a long period of time. Blood has a harder time passing through deposits of fatty material and cholesterol (plaques) that form in the lumen of medium- and large-sized arteries because they make the blood vessels' inner surface uneven and the lumen constrict. Blood vessels also lose some of their flexibility as a result. The plaques formed could eventually break down and cause blood clots to form. While a blood clot that forms in the brain can result in a stroke, a blood clot that forms in a coronary artery can result in a heart attack.

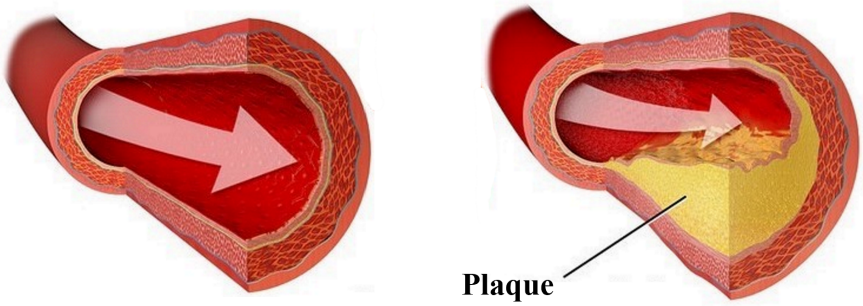

Figure 2.11: Comparison between a healthy artery and an artery affected by atherosclerosis.

Risk factors are variables that contribute to the development of atherosclerosis and are divided into two groups:

- *Behavioural risk factors*, such as tobacco and alcohol use, unhealthy diet and physical inactivity.
- *Metabolic risk factors*, such as raised blood pressure (hypertension), raised blood lipids (e.g. cholesterol), raised blood sugar (diabetes), overweight and obesity.

Congenital heart defects are another category of non-atherosclerotic CVDs that involve anomalies of the heart's structural components. Congenital heart illness can manifest as malformed heart chambers, abnormal valves, and holes in the heart's septum. Damage to the heart muscle and heart valves brought on by rheumatic fever is the hallmark of rheumatic heart disease. The prevalence of other CVDs, such as heart valve diseases, electrical conduction system disorders, and abnormalities of the heart muscle (such as cardiomyopathy), is lower than that of heart attacks and strokes.

Due to population growth and aging, prevalent cases and deaths of cardiovascular diseases have increased in previous years and are likely to increase significantly in the coming years (Figure 2.12). Furthermore, clinical procedures and healthcare expenses are significantly impacted by the global trend of CVDs. In the United States alone, adult-related spending on cardiovascular disease grew by more than $100 billion between 1996 and 2016, totaling about $320 billion each year in direct costs such as inpatient costs, ambulatory costs, expenses for prescribing drugs, nursing care facility costs and expenses for the management of the emergencies [4]. Additionally, because early retirement and labor force loss result in lower income, the overall costs of CVD are higher than the direct expenses of hospitalization and care.

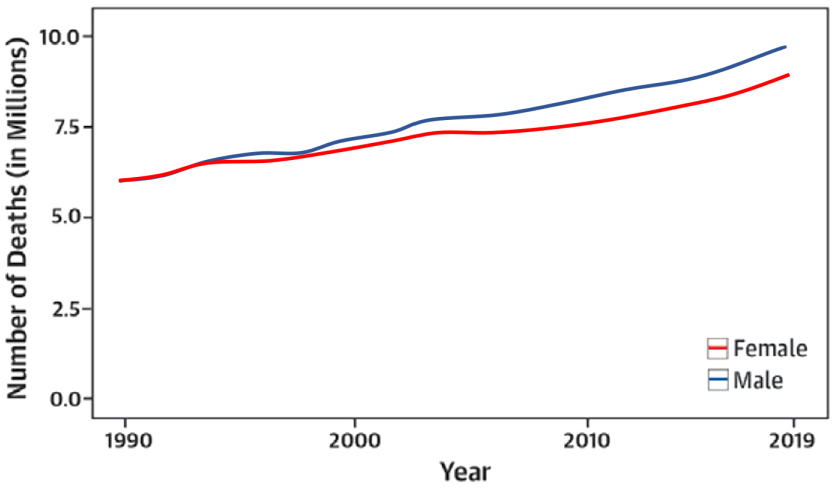

Figure 2.12: Number of CVD deaths in the world from 1990 to 2019 divided by sex [3].

Given this circumstance, it is imperative to put into practice workable and affordable techniques for the prevention, early diagnosis, and control of diseases, as well as to monitor the results in order to reduce premature death and limit other adverse effects caused by CVD.

2.2.1 Hypertension and arterial stiffness

One of the risk factors for CVD that has the strongest evidence for a causal relationship and is the primary preventable cause of cardiovascular disease is high blood pressure, also known as hypertension [6]. Blood pressure that is consistently higher than normal at rest, more than 120 mm Hg (systolic) and more than 80 mm Hg (diastolic), is referred to as hypertension. Although it is not possible to establish exactly why someone develops high blood pressure, the condition of hypertension is known to be associated with a number of risk factors, such as genetic predisposition, smoking, high cholesterol levels, and obesity.

Atherosclerosis, or artery hardening, and hypertension are closely related conditions. Atherosclerosis is characterized by the buildup of fatty plaque in the artery walls, which lessens their elasticity and narrows the lumen. The blood vessel's increased resistance as a result of the reduced lumen leads to hypertension. However, hypertension also weakens the artery walls, making them more susceptible to atherosclerosis. As a result, a vicious cycle occurs in which each condition, atherosclerosis and hypertension, feeds the growth of the other. The cardiovascular system is impacted negatively by hypertension in several ways. Since it puts more strain on the heart, elevated arterial blood pressure can increase the risk of myocardial infarction, or a heart attack. It can also lead to heart failure,

renal dysfunction, peripheral vascular disease, damage to the blood vessels in the retina, and vision loss.

Category	Systolic (mmHg)	Diastolic (mmHg)
Optimal	< 120	< 80
Normal	120 – 129	80 – 84
High normal	130 – 139	85 – 89
Grade 1 hypertension	140 – 159	90 – 99
Grade 2 hypertension	160 – 179	100 – 109
Grade 3 hypertension	> 180	> 110

Table 2.3: Office blood pressure classification and hypertension definitions grade [6].

Blood pressure monitoring and the analysis of several predictive parameters can help with early diagnosis and lower the chance of developing additional hypertension-related problems or CVD deaths [18]. The arterial stiffness, a crucial component of cardiovascular physiology and a significant prognostic index and potential therapeutic target in patients with hypertension, is a key predictive parameter for the outcome of CVDs [5]. Several studies have established arterial stiffness as an independent predictor of cardiovascular events and a strongly related parameter to the condition of hypertension. Greater stiffening over time is thought to be caused by a number of aging-related degenerative changes in the walls of the large elastic arteries, but complications from hypertension and cardiovascular diseases, in general, can also be avoided by treating hypertension before the first symptoms of stiffening appear. Consequently, it becomes crucial to quantify arterial stiffness using clinical techniques.

2.3 Arterial pulse

An essential vital sign is the arterial pulse. The quick ejection of blood into the aorta and its transmission across the arterial system cause an artery to abruptly expand, made possible thanks to the elasticity of the blood vessels [19]. Every time the heart contracts, blood is ejected into the arteries throughout the body, where it is converted to flow and pressure. Although any such pulsation can be referred to as a pulse, a clinician will only be able to detect the pressure pulse in a large, accessible artery.

A pressure wave known as a sphygmic wave is created by the heart's systole

and spreads through the peripheral system because of arterial elasticity when blood is pushed into the aorta. The pressure wave is perceptible superficially at the level of the arterial sites. The arterial pulse reflects the heart's contraction and, for this reason, is strongly related to the electrocardiogram. The arterial pulse measures the mechanical contraction of the heart while the electrocardiogram reflects its electrical contraction. In this way, it is feasible to use a tactile technique to determine the heartbeat from the arterial pulse. This signal can also be used to measure several other clinical characteristics.

2.3.1 Morphology of the arterial pulse

The arterial pulse shape depends on the heart phase and can be divided into the anacrotic limb, which is the rapid-rising portion of the arterial pressure curve and corresponds to the systolic phase, and the dicrotic limb, which is the decrease of aortic pressure as further runoff in the peripheral circulation during the diastolic phase [19].

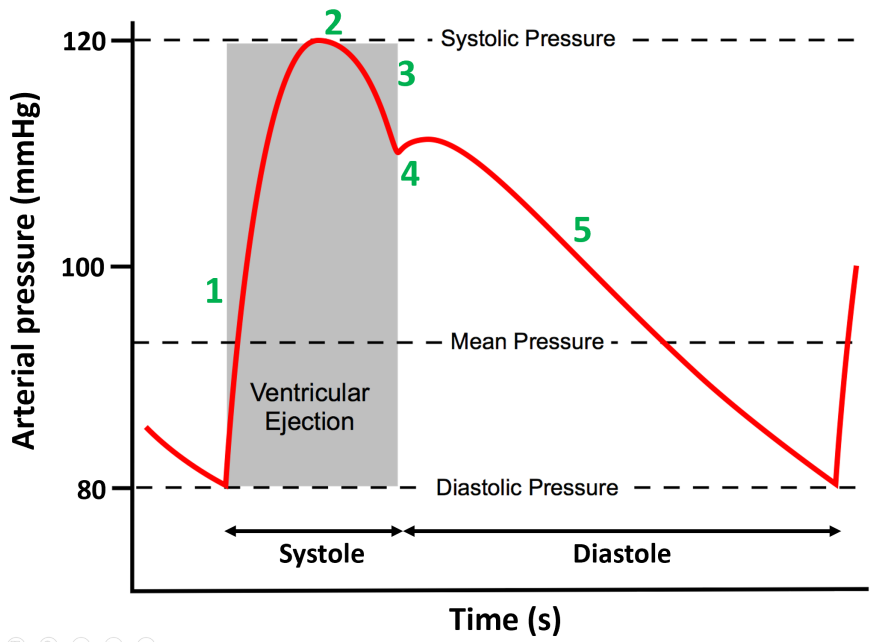

Figure 2.13: Picture of the characteristic waveform of the arterial pulse.

The main characteristics of the arterial pulse waveform are as follows [20]:

1. *Systolic upstroke*, which is the abrupt rise in signal from the bottom of the waveform to its peak, which is indicative of ventricular ejection. This component, which is produced by the peak in aortic blood flow during the

aortic valve's opening, shows how the aorta's walls store energy as pressure. The effectiveness of the aortic valve and pressure changes within the left ventricle both affect this segment's slope.

2. *Systolic peak pressure*, which stands for the highest pressure produced during ventricular ejection. Its shape is the result of the interaction between reflected waves that are generated into the vascular system and the hydraulic resistance of the artery, which rises as the radius falls. Therefore, when the collecting point is moved further from the heart, the peak pressure rises. According to the collection site, in some instances, the waves are forced back towards the aortic valve, even generating an anacrotic notch along the systolic upstroke.

3. *Systolic decline*, which is the rapid drop in pressure that occurs in the final stage of systole. It happens when the influx of blood from the ventricle is slower than the efflux of blood from the artery.

4. *Dicrotic notch*, which stops the pressure from dropping and marks the beginning of diastole. The incisura on the descending limb of the arterial pulse pressure is connected to a transient reversal in blood flow from the central arteries toward the ventricle just prior to aortic valve closure. The second smaller positive wave after the dicrotic notch is due to the aorta and aortic valve elastic rebound when the latter closes at the end of the ventricular ejection, but it is also influenced by reflected waves from more distal arteries.

5. *Diastolic runoff*, which is the pressure drop that is noticed following the closing of the aortic valve and during the diastolic runoff in the peripheral circulation. The pressure inside the aorta gradually drops as the ventricle stops pumping blood there. It occurs because the artery's flexibility maintains a high pressure during the early diastole phase, forcing blood into the systemic circulation.

After the R wave on the ECG, the arterial waveform's systolic upstroke can be seen, reflecting the time the pulse takes from electrical initiation to the ventricle's expulsion of blood to reach the arterial site of interest. This interval represents the time needed for the mechanical pressure wave to travel to the collection point.

The arterial pulse waveform can provide the following informations:

- *Area under the curve (AUC)* is strongly related to mean arterial pressure. MAP is the driving pressure of the cardiovascular system and it is a mean over time of pressure in the arterial system in a specific site.

- *Pulse amplitude* is measured as the difference between the arterial pulse signal's baseline and systolic peak pressure. It is employed as a vasoreactivity and blood volume indicator since it is connected to vascular distensibility. A high

amplitude indicates vasodilatation, or a rise in blood volume, close to the sample site, whereas a low amplitude indicates vasoconstriction, or a reduction in blood volume. It can also be used as a tool to estimate blood pressure.

- *Cardiac cycle* is the time of activity of the human heart from the start of one heartbeat until the start of the following. It is therefore identified as the time between two systolic upstrokes. The heart rate can be calculated using the duration of the cardiac cycle.

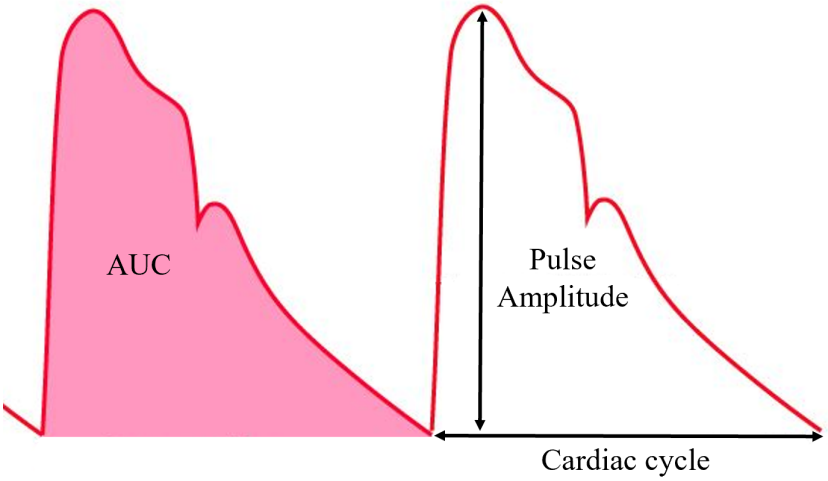

Figure 2.14: Picture of the area under the curve (AUC), pulse amplitude and cardiac cycle [21].

2.3.2 Collecting sites of the arterial pulse

A number of locations on the body can be used to collect arterial pulses, which are further classified into peripheral and central pulses depending on how close to the heart the signal is acquired. The arterial pulse alters as it moves from the central aorta to the peripheral arteries as a result of the impedance and harmonic resonance of the vascular tree. The systolic pressure rises even if the mean blood pressure and diastolic pressure fall as the pulse travels from the central aorta to the peripheral arteries. The arterial pulse's peripheral distortion increases with the distance between the heart and the artery in question. On the carotid site, a central pulse, the anacrotic notch is more noticeable than on the peripheral sites. The systolic upstroke also gets sharper as it moves through the arterial tree towards the peripheral because the smaller artery has a larger resistance. The dicrotic notch refers to a progressively decreasing pressure value, and it occurs more slowly than the systolic peak pressure. With growing distance from the aortic valve, both the

systolic peak pressure and pulse pressures are increased. The process in the aorta where kinetic energy is first transformed into potential energy during systole and the following diastolic recovery of this accumulated energy is what leads to the transformation of the ventricular pressure pulse to the peripheral pulse, with its continuous flow and minor pressure variations.

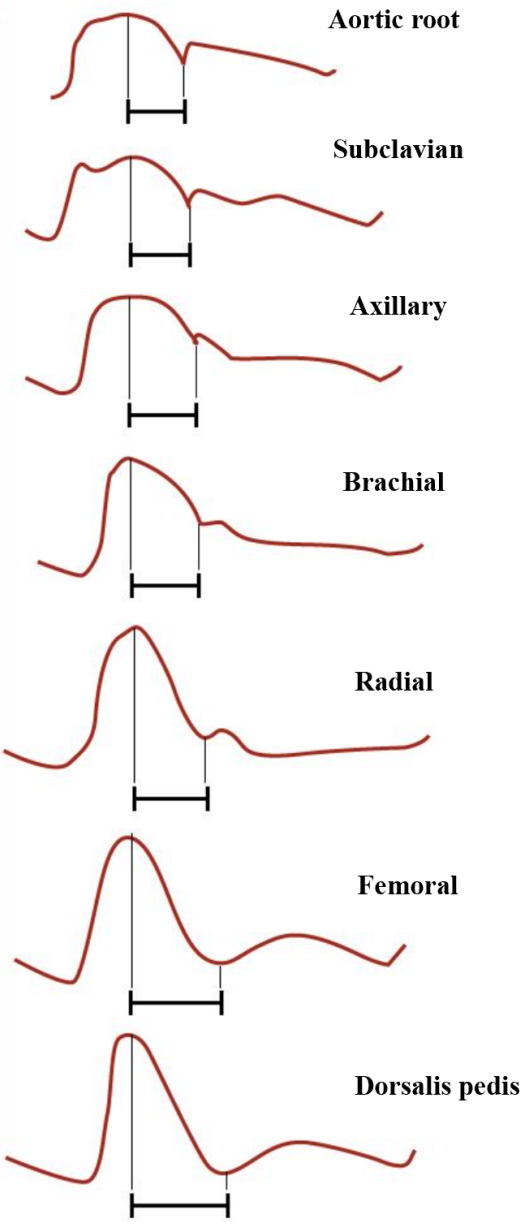

Figure 2.15: Influence of the collecting site on the arterial pulse waveform [21].

The main accessible collection sites of the arterial pulse along the body at central and peripheral sites are classified below:

Type	Artery
Central pulse	Carotid
	Brachial
	Femoral
Peripheral pulse	Radial
	Posterior tibial
	Dorsalis pedis

Table 2.4: Main places where the arterial pulse can be collected easily and their classification.

The arterial pulse pressure wave propagates to the surface and is perceptible by palpation or by instruments that use pressure, force or other physical quantities transducers. The arterial pulse is perceived as a variable displacement overlaid on the baseline displacement caused by the pressure applied to the artery to produce the perception of the pulse itself. When the peripheral arteries are sufficiently close to the skin surface to be compressed, they can be palpated.

2.4 Pulse Wave Velocity (PWV)

Pulse Wave Velocity (PWV) is defined as the gold standard for the measurement of arterial stiffness by the "Expert consensus document on the measurement of aortic stiffness in daily practice using carotid-femoral pulse wave velocity" [22]. Particularly, the greater the PWV, the stiffer the arterial tree is. PWV represents the rate at which the blood pressure pulse, which is produced by the heart's systolic contraction during each cardiac cycle, propagates through the arterial tree.

The method most approved by the literature and used in the clinic is the carotid-femoral Pulse Wave Velocity (cfPWV), where the carotid artery, located close to the neck, serves as the location for the proximal site and the distal site is the femoral artery, located midway between the symphysis pubis and the anterior superior iliac spine. In particular, cfPWV is a measure of regional arterial stiffness of the arterial territory between the two sampling sites and, therefore, is closely related to the elastic property of central arteries. The velocity is obtained by the ratio between the direct distance that separates the two collecting sites, which is multiplied by a corrective factor of 0.8 to approximate the path length of the arterial tree between the carotid artery and femoral artery, called Pulse Wave Distance (PWD) [23], and

the Pulse Transit Time (PTT). This last corresponds to the amount of time the pulse needs to travel between the two acquisition sites. The linear ratio between the PWD and the PTT is used to calculate the PWV parameter [24]:

$$PWV = \frac{PWD}{PTT} \Longrightarrow cfPWV = \frac{0.8 \cdot d}{PTT} \tag{2.4}$$

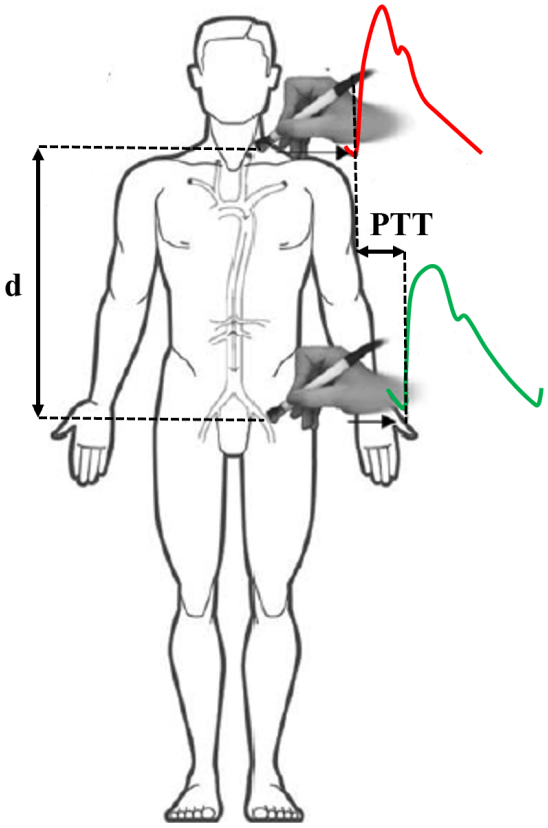

Figure 2.16: Illustration of the cfPWV measuring [22].

The extraction of PWV therefore focuses on accurately detecting the PTT, as the PWD parameter is obtained in a classical way by the clinician by measuring it with a measuring tape. Depending on the withdrawal instrument being used, there are two alternative ways to retrieve the PTT: [25]:

- *Two-steps method*, which requires the ECG signal integration. This method divides the PTT examination into two steps and uses the R peak of the ECG as a reference point since it is representative of ventricular ejection. Firstly, the carotid PTT (cPTT) is extracted, which is the amount of time needed for the blood pulse to go from the heart (ECG reference - R peak) to the

carotid (mechanical wave detection). Secondly, the sensor is moved to the femoral site for the femoral PTT (fPTT) and the same procedure is repeated. The difference between the two acquired intervals is the PTT that is finally considered for the PWV evaluation ($cfPTT = fPTT - cPTT$):

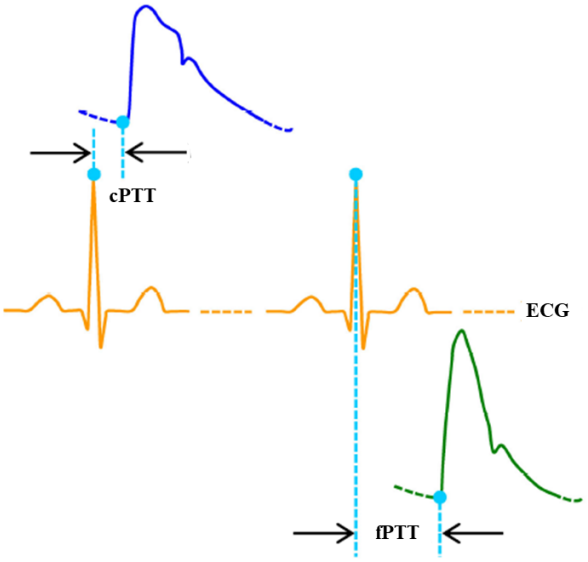

Figure 2.17: Measurement of PTT using the two-steps method.

- *One-step method*, which involves a single simultaneous collection of the pulse waves on carotid and femoral sites without the ECG, allowing an immediate evaluation of the differential PTT.

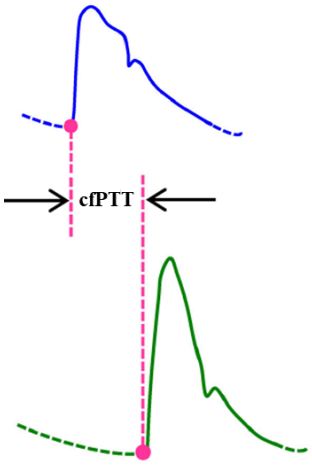

Figure 2.18: Measurement of PTT using the one-step method.

As previously mentioned, PWV serves as a measure of the arterial territory's stiffness between two collecting sites. Actually, this metric depends not only on the elastic module of blood vessel walls (E), which depicts the wall's inherent stiffness, but also on the arterial geometry, such as the radius (r) and the thickness (h), and blood density (ρ). Moens and Korteweg defined the relationship showed below in order to correlate all the parameters mentioned with the PWV [26]:

$$PWV^2 = \frac{Eh}{2r\rho} \tag{2.5}$$

Later, Bramwell and Hill used vascular physiology to extend the Moense-Korteweg equation and described how relative changes in volume ($\Delta V/V$) and pressure (ΔP) correlate following the relationship [27]:

$$PWV^2 = \frac{\Delta PV}{\Delta V\rho} \tag{2.6}$$

In order to quantify the arterial capacity to expand and contract with cardiac pulsation and relaxation, arterial distensibility is introduced, defined by the following formula [28]:

$$Distensibility = \frac{\Delta V\rho}{\Delta PV} = \frac{1}{PWV^2} \tag{2.7}$$

As PWV is the square of the inverse of distensibility, it may be inferred that it is a direct indicator of arterial stiffness. Therefore, a lesser distensibility and compliance are indicated by a greater PWV value, which in turn suggests a higher stiffness.

The Pulse Wave Velocity reference value is approximately 6 m/s for healthy adults [29]. However, this value rises with aging and the presence of additional complications, such as diabetes (about 9 m/s). The European Society of Hypertension's most recent recommendations suggests that in middle-aged hypertension patients, a measured PWV of more than 10 m/s can be regarded as a conservative estimate of significant alterations of aortic function [6]. Consequently, being able to recognize reliable PWV values in asymptomatic patients would enable early arterial stiffness assessment, which would then provide a better estimate of cardiovascular risk and enable timely therapy targeting [30].

2.5 Clinical devices for PWV estimation

Several devices using different techniques have been developed in the years for the PWV evaluation in a non-invasive manner. Applanation tonometry is the most widely used approach to detect the pressure wave generated by the systolic ejection of the heart at two distinct locations. A tonometer is a pressure sensor that can

be used to detect changes in surface tension brought on by the pulse of blood in an artery when placed on skin near the artery. According to the Laplace law, this variation is closely related to the change in blood pressure that occurs inside the vessel [31]. Piezoelectric mechanotransducer, cuff-based oscillometry, ultrasound, and photoplethysmography are other types of less widely used technologies in this field. Commercial devices for the PWV estimation are usually costly, requiring considerable operating skills, which could deeply affect the measurement. For these reasons, the widespread use in clinical environments is limited.

The main commercial devices for evaluating PWV are illustrated below [22]:

- **SphygmoCor**® (AtCor Medical, Sydney, Australia) employs a tonometric sensor mounted to a pen-like support and is considered the clinical golden standard for PWV estimation. It implements the two-steps method so, to synchronize the R peak with the two distinct pulse waves, an ECG recording is required.

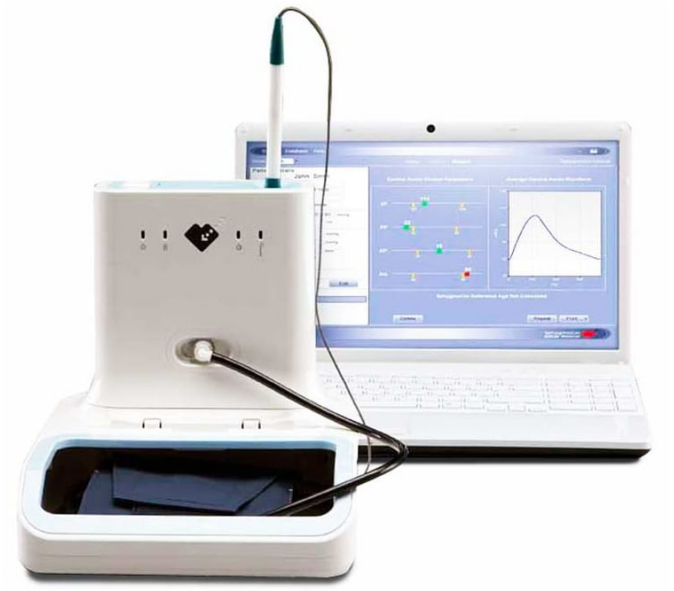

Figure 2.19: Illustration of the SphygmoCor device [32].

- **PulsePen**® (DiaTecne, Milano, Italy) consists of a wireless receiver, an ECG unit because pulse wave registration is not simultaneous, and high-definition tonometry. A two-tonometer version has been available since 2014, enabling an ECG-free PWV evaluation.

Figure 2.20: Illustration of the PulsePen device [33].

- **Complior Analyse**® (Alam Medical, Paris, France) includes two piezoelectric mechanical transducers, and two pulse waves are simultaneously acquired. Sensors are placed at the carotid and femoral sites. Radial and distal additional probes are included, enabling simultaneous PWV evaluation on three separate segments and allowing the peripheral arteries state assessment.

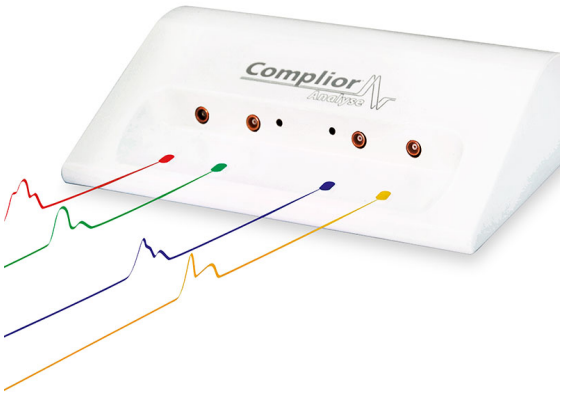

Figure 2.21: Illustration of the Complior Analyse device [34].

A non-commercial device, but of considerable interest, is Athos (Arterial sTiffness faitHful tOol aSsessment) [35], an instrument developed by "Politecnico di Torino" that uses the one-step method and which implements two MEMS pressure sensors produced by STMicroelectronics incorporated in two pen-shaped probes. The two tonometers are connected to the main unit, which controls the signal acquisition, and are built inside two ergonomic cases for simple handling. The data are transmitted

to a laptop via Bluetooth and displayed in real-time on a graphical user interface. The device could be equipped with an external electrocardiograph, which therefore allows for two-step measurement.

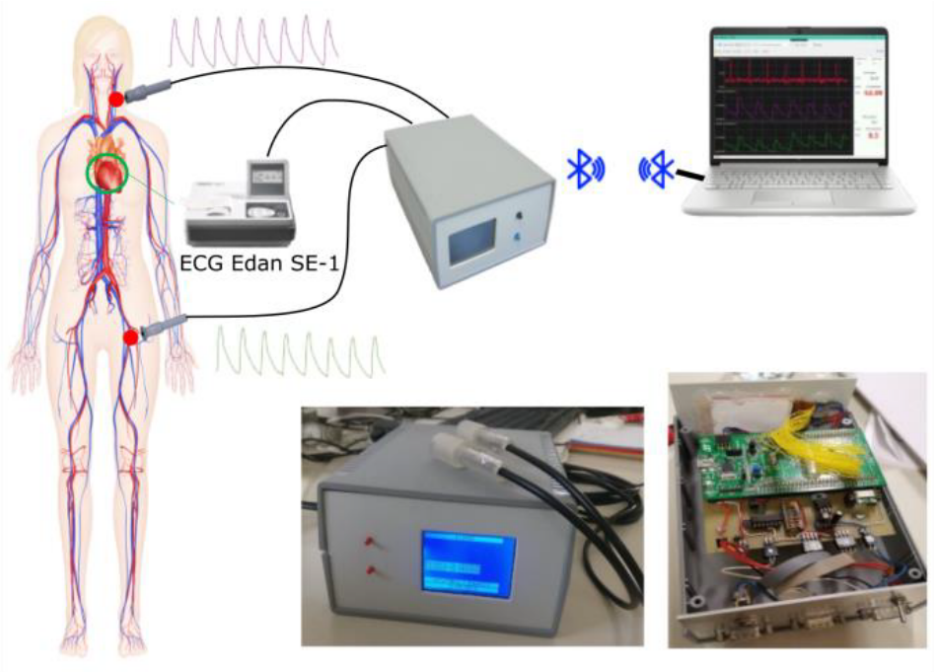

Figure 2.22: Illustration of the Athos device [35].

The piezo-resistive and ultra-compact MEMS nano pressure sensor LPS35HW, made by STMicroelectronics, functions as a digital output barometer and is the sensitive component of the device [36]. The sensor has been changed into a force sensor by incorporating a resin into the sensitive element. The sensor, which is a silicon membrane implanted in a Wheatstone bridge structure, deflects when pressure is applied. The bridge becomes imbalanced as a result of the induced resistance change, producing an output signal that passes through a certain conditioning circuit. The core component of the conversion chain is a low-noise amplifier that uses an analog-to-digital converter (ADC) to turn resistance changes caused by pressure and temperature into digital values. Additionally, there is an integrated circuits (IC) interface that enables I2C or SPI communication directly with a microcontroller.

Analyzed the state of the art regarding the devices in this field, this thesis presents an innovative Pulse Wave Velocity estimation system using a Force Sensing Resistor (FSR) in a biomedical wearable configuration, which can overcome the limitations avoiding the operational skill that today's technologies demand. Other advantages of the presented device are that it simultaneously carries out the one-step PWV

evaluation and, compared to other PWV technologies, the budget of the system's components and overall construction is cost-effective.

2.6 Utilized software

The following is a description of the software tools needed to develop the presented system:

- **LabVIEW** (Laboratory Virtual Instrumentation Engineering Workbench) is the development environment for the visual programming language (G language) of National Instruments. It is utilized for data collection and analysis, process control, and industrial automation using a graphical syntax. The data structures and algorithms are composed of icons and other graphic elements that are connected by a wire to create a kind of flow diagram. Because the execution sequence is specified and represented by the data flow through the monodirectional wires that connect the functional blocks, this form of language is known as dataflow. In this thesis, LabVIEW has been used to acquire data directly from the Agilent 34411A multimeter, plot them on a graph and save them in a specific Excel file. In particular, the multimeter has been used to measure the resistance of the various FSR sensors characterized during this work as the weights applied to the sensors themselves vary.

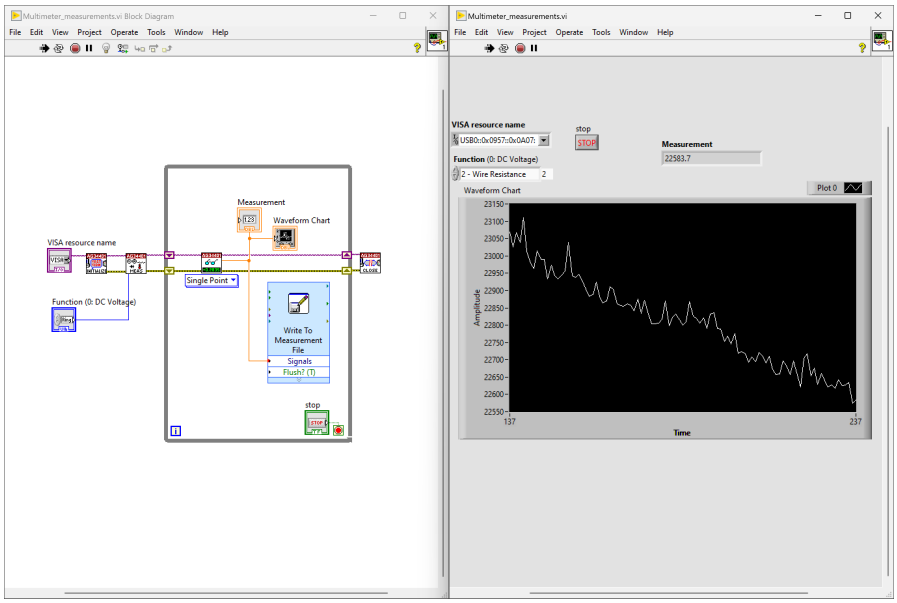

Figure 2.23: Picture of front panel and block diagram of the graphic interface developed on LabVIEW for the resistance measurements of the FSRs carried out by Agilent 34411A multimeter.

- **Keil μVision® IDE** is a window-based software development platform for Arm®-based microcontrollers that includes editor and debug embedded applications. It includes a C/C++ compiler, macro assembler, linker/locator, and a HEX file generator, as well as all the other tools needed to design embedded applications. In this work, Keil has been used to program the Arm® Cortex®-M4 core-based STM32F429 microcontroller using C language.

- **LTSpice®** is a open-source software developed by Analog Devices for modeling and analyzing the behavior of analog electrical circuits. It carries out a number of circuit simulation investigations, including Bode diagrams, waveform viewers, and DC and AC transfer functions. In this project, it has been used for simulating and optimizing each stage of the conditioning system focusing, in particular on the filtering stage in order to choose the best filters for this specific application.

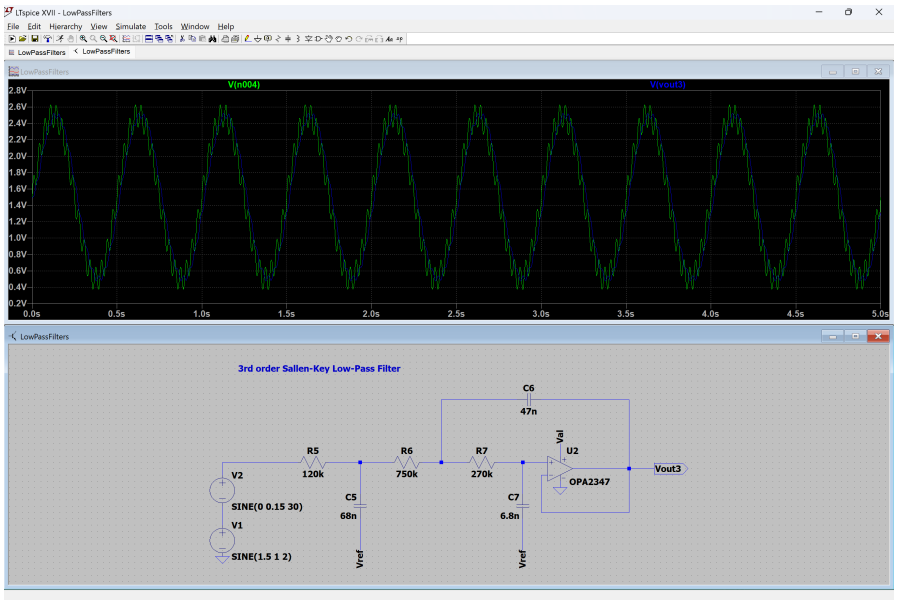

Figure 2.24: A simulation on LTSpice® of a low-pass filter is shown. The blue sinusoid represents the filtering stage's output, displaying its actual filtering capabilities, while the green sinusoid shows the filtering stage's input.

- **Microsoft Visual Studio** is a Microsoft integrated development environment (IDE). It is employed in the creation of computer programs such as web applications, websites, web services, mobile applications, and graphical user interfaces. This environment has been utilized in this work to create the graphical user interface with the use of C# language. The interface allows

visualizing the signals taken from the devices on the carotid and femoral sites and to save the data in a binary file.

- **Altium Designer®** is an electronic design automation software package for printed circuit boards (PCB), developed by Altium Limited. 3D PCB design, schematic capture, field programmable gate array development and release/data management are the four primary functional areas covered by the suite of Altium Designer®. In this work, Altium Designer® has been used to develop the read-out circuit on a specific PCB.

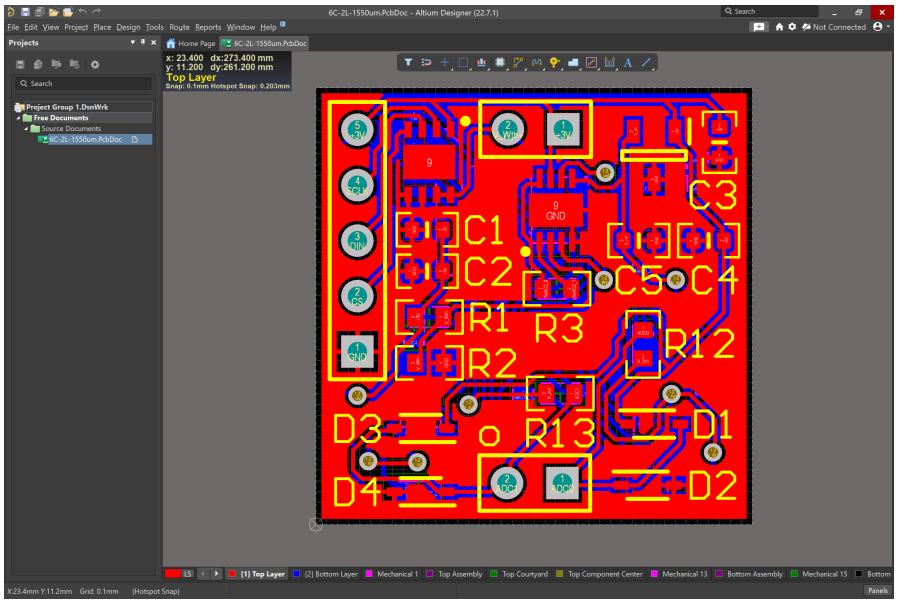

Figure 2.25: Picture of the development environment in Altium Designer®, with a focus on the top layer of the developed PCB.

- **MATLAB®** is a high-level programming language and a numerical computing environment created by MathWorks. It enables matrix manipulation and is based on C. Thanks to the different toolboxes customized for each application, it is utilized all around the world for implementing algorithms, analyzing data, and developing control systems. In this thesis, it has been mainly used to implement the intersecting tangent method algorithm for PWV extraction starting from the binary file in which are saved the two pulse waves. In addition, it has been also used to conduct statistical analysis between the results obtained from the device under test and the gold standard for PWV evaluation, SphygmoCor.
- **SolidWorks** is a solid modeling computer-aided design (CAD) application developed by Dassault Systèmes. It has been used to produce supports in

order to characterize the FSR sensors before they have been integrated into the system and to draw 3D models of the holders for FSR and PCB. After being designed, the model has been printed in resin using a Form3 3D printer.

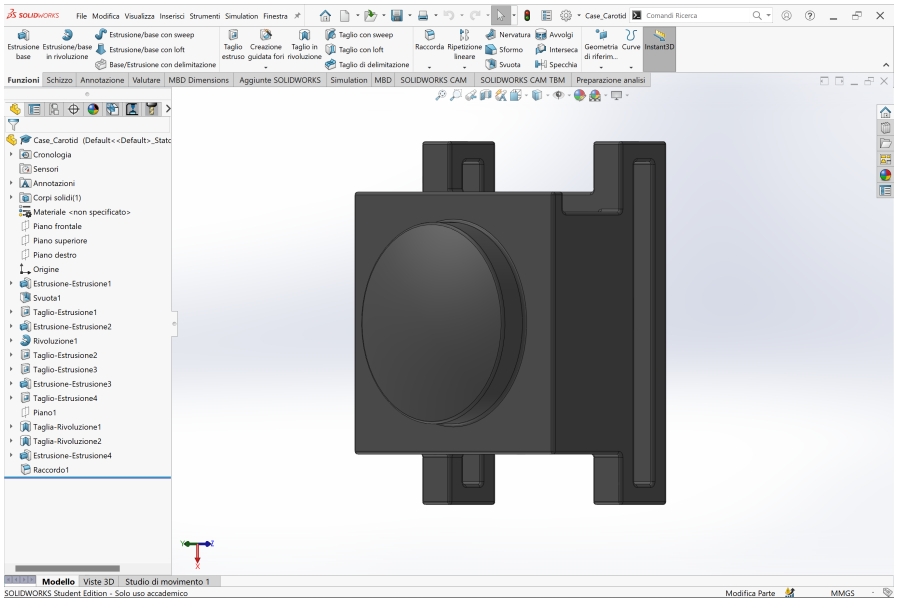

Figure 2.26: The SolidWorks workspace is shown. The model visualized is the carotid FSR holder.

Chapter 3

Force Sensing Resistor (FSR)

This chapter describes the Force Sensing Resistor (FSR) which is the sensing element of the presented device, whose purpose is to evaluate the cfPWV, and an in-depth study is made on the different construction methods of this type of force sensor. In order to select the most suitable type of FSR for the application, the characterization carried out on commercial sensors is presented.

3.1 FSR overview

Force Sensing Resistors (FSR) is a piezoresistive sensor that enables measuring both static and dynamic forces applied to its surface [37]. The response of the transducer exhibits a change in its electrical resistance varying according to applied force. The FSR has an extremely high resistance when no force is applied to it, on the order of MΩ, but under applied force, its resistance is significantly reduced [38]. It is considered as a promising type of sensor for wearable biomedical applications because it requires small surface area for activation, is low-cost, flexible, easy-to-integrate and is highly tolerant to temperature, chemicals and moisture [39]. All these attributes led to its being chosen to detect the vessel wall movement in the arterial site in a wearable configuration.

In general, the FSR sensor category falls into the largest force sensor family. There are a variety of transducers available on the market and in the scientific literature that convert force into an electric quantity.

The main types of force sensors are:

- *Strain gauges*, which are based on the variation of resistance of a deformed conductor, since the electrical resistance of a conductor is a function of its mechanical dimensions. In this way, a strain is converted into a resistance variation. Additionally, within certain bounds, a material's strain and force have a clear relationship, making it easy to determine the actual force using the strain gauge's measurement of deformation.

Figure 3.1: Picture of a strain gauge.

- *Piezoelectric sensors*, which depend on the ability of particular materials to produce an electric charge while under stress, known as piezoelectric effect. A sophisticated electronic is needed to extract the charge information from the material because parasitic effects frequently combine the charge, quickly bringing the material to neutrality. This means that measuring static or slowly fluctuating forces is difficult to do with these transducers. Additionally, the electronics must be protected because when a sensor is activated with a strong impulsive drive, large voltages of up to thousands of volts can result.

- *Piezoresistive sensors*, which are resistive sensors, like strain gauges, but they operate differently as they are based on a different physical mechanism. In fact, piezoresistive sensors are based on variations in the conductor's conductivity, whereas strain gauges are based on variations in the conductor's length and width. Piezoresistivity, then, is the general term used to characterize a material's ability to modify its conductivity in relation to the applied pressure. This sort of sensor has the benefit of being easily constructed utilizing flexible materials, as well as being very resistant to noise and having simple conditioning electronics. In addition, they are transducers that can be used in a single-point implementation, so they are able to sense pressure or force in a small area. As a result, they are compact and inexpensive, with a single output.

As already mentioned, FSR is a piezoresistive sensor, and therefore the operating principle is based on a change in the conductivity of the sensor itself as the force varies. This type of behavior is possible thanks to the construction method with which the sensor is made. The basic concept of the construction mode provides

that the FSR is typically made out of two conductive layers separated by a spacer. Applying a force to the surface of the FSR causes layers to touch themselves and, in this way, the sensor's overall resistance declines in a non-linear pattern (Figure 3.2).

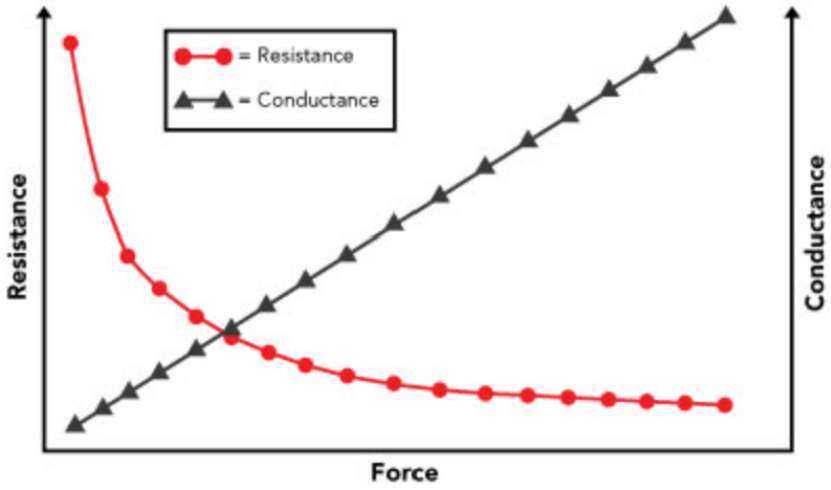

Figure 3.2: Typical FSR Force vs. Resistance and Conductance characteristic curve. It is noticed that the resistance declines with a non-linear trend whereas the conductance increases linearly as the force applied to the sensor increases.

The way in which the two layers are constructed differentiates commercial FSRs into two categories, shunt mode and thru mode [40], which will be analyzed in the next sections. These FSR types exhibit different Force vs. Resistance characteristics.

3.1.1 Shunt mode

Shunt mode is a construction method for FSR that consists of a polyethylene terephthalate (PET) external layer and three main internal layers. The top layer inside the PET materials is made of FSR conductive ink, which contains both electrically conducting and non-conducting particles suspended in a matrix, followed by a spacer and a silver conductive interdigitated circuit layer. By composing all the layers of the sensor, a thickness typically of less than 0.5 mm results. The result is a flexible sensor due to the extremely low height and robustness of the materials even when bent.

Applying a force to the FSR causes particles to touch the conducting electrodes, so the traces on the opposing layer are bridged or shunted by the FSR ink on one layer (hence the name shunt mode). In this manner, a current is produced, and the sensor's overall resistance is reduced.

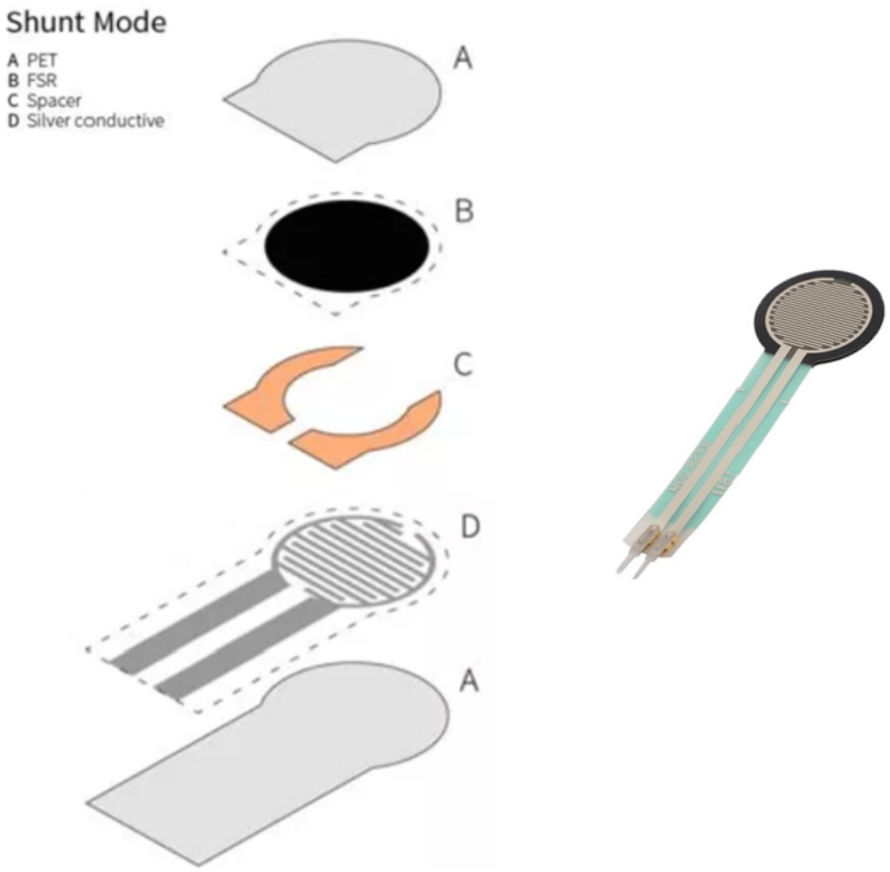

(a) Shunt mode layers

(b) Commercial FSR shunt mode device: FSR® 402

Figure 3.3: Overview of FSR shunt mode

3.1.2 Thru mode

Thru mode is another construction method that uses FSR ink and a silver conductive sheet in five total layers sandwiched between the external flexible PET material. FSR ink is placed above the spacer and is followed by a silver conductive sheet. Below the spacer, the layer is specular. In this way, there are two identical basic components separated by the spacer.

When a force is applied, the two layers come into contact and a current is generated and passes across the spacer (hence the name thru mode). As also happens for the shunt mode, the greater the contact between the two layers and therefore the highest the force applied to the sensor, the more current flowing between the two layers and therefore the lower the overall resistance.

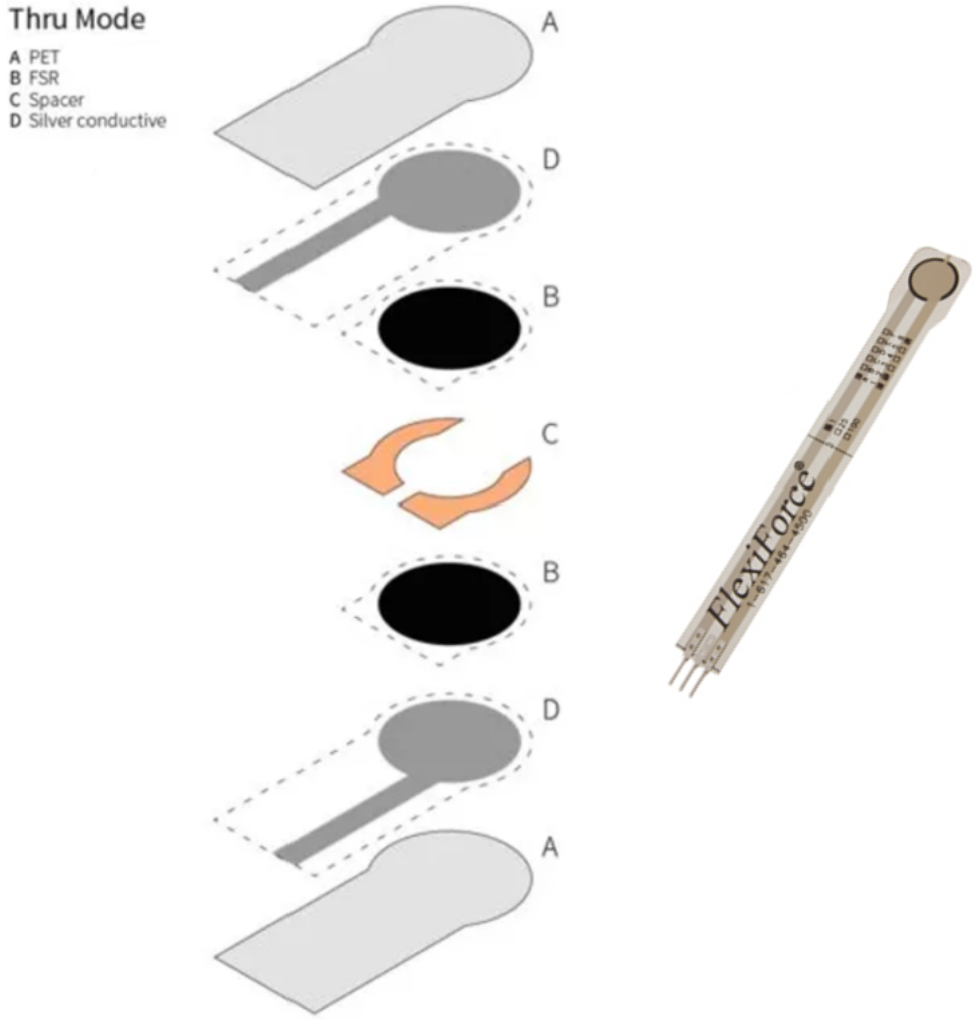

(a) Thru mode layers

(b) Commercial FSR thru mode device: FlexiForce™ A201

Figure 3.4: Overview of FSR thru mode

3.2 Sensors characterization

In order to select the most suitable commercial FSR for detecting the pulse pressure waves to calculate the PWV, a characterization of the main commercial sensors has been carried out both for the shunt construction mode and for the thru mode. The objective has been to determine which of the two construction techniques would best suit the application based on the Force vs. Resistance characteristic curve

and on the dynamic behavior. In particular, given the blood pressure values of the human body and the variability introduced by the thickness of the tissues [41] and considering the average active area of the FSR sensors, the range of force with which it is possible to perceive the pulse wave on the skin is 0-5 N. It is also important to understand the effect of the static force present when applying the sensitive element on human skin on the measurement range in which the measurement is made. The average static force applied in this type of measurement is around a few Newtons (1-2 N). Starting from these peculiarities, it is possible to study the characteristic curve of the sensors to understand which is best suited to the application.

The commercial sensors studied have been the following:

- *FSR® 400* (Interlink Electronics, Camarillo, United States) is a shunt mode FSR. It has a 5.1 mm diameter active area and its dynamic force sensing range spans from 0.1 N to 20 N [42].
- *FSR® 402* (Interlink Electronics, Camarillo, United States) is a shunt mode FSR. It has a 14.7 mm diameter active area and its dynamic force sensing range spans from 0.1 N to 20 N [43].
- *FlexiForce™ A201-1lb* (Tekscan, Norwood, United States) is a thru mode FSR. It has a 9.5 mm diameter active area and its dynamic force sensing range spans from 0 N to 4.4 N (low range) [44].
- *FlexiForce™ HT201* (Tekscan, Norwood, United States) is a thru mode FSR. It has a 9.5 mm diameter active area, its dynamic force sensing range spans from 0 N to 222 N and is capable of measuring force and pressure in environments as hot as 200 °C [45].

Figure 3.5: From left to right: FSR® 400, FSR® 402, FlexiForce™ A201-1lb, FlexiForce™ HT201

Analyzing the four sensors previously described, a static characterization has been carried out using a set of weights composed of masses of 10 g, 20 g, 50 g, 100 g, 200 g, 250 g, 500 g and 750 g (corresponding to about 0.1 N, 0.2 N, 0.5 N, 1 N, 2 N, 2.5 N, 5 N and 7.5 N). Since FSRs are force sensors, their resistive output is very sensitive to the area on which the force is applied. For this reason, a 3D-printed support for the weights has been designed that would allow to standardize the applied force over the entire area of the FSR under investigation. The support is shown in Figure 3.6.

Figure 3.6: Support used to uniform the force applied by the weights (resting on the upper face of the support) on the FSR (inserted between the two pieces of the support).

For each FSR and for each weight, a static resistance measurement has been conducted for 60 seconds, acquiring the resistance value recorded by the Agilent 34411A multimeter on a program developed ad hoc on LabVIEW that allows saving the data on an Excel sheet for later processing (Figure 2.23). By acquiring all the measurements, it has been possible to plot the Force vs. Resistance curve for each sensor to be characterized, using the mean value of the resistance measured in 60 seconds. The curves obtained are shown in Figure 3.7, with the characteristic curve for each sensor and zoom in the average working range of the application. The baseline line indicates the average static pressure applied to the FSR.

In order to have a numerical value indicating the signal-to-noise ratio (SNR) of the sensor in the range of interest (1-2 N) the following quality coefficient (q) has been implemented:

$$q = \frac{slope_{(1N-2N)}}{\sigma_{(1N-2N)}} \tag{3.1}$$

The slope of the curve indicates the sensor response to the variation of the applied force, while σ is the standard deviation of the resistance measurements.

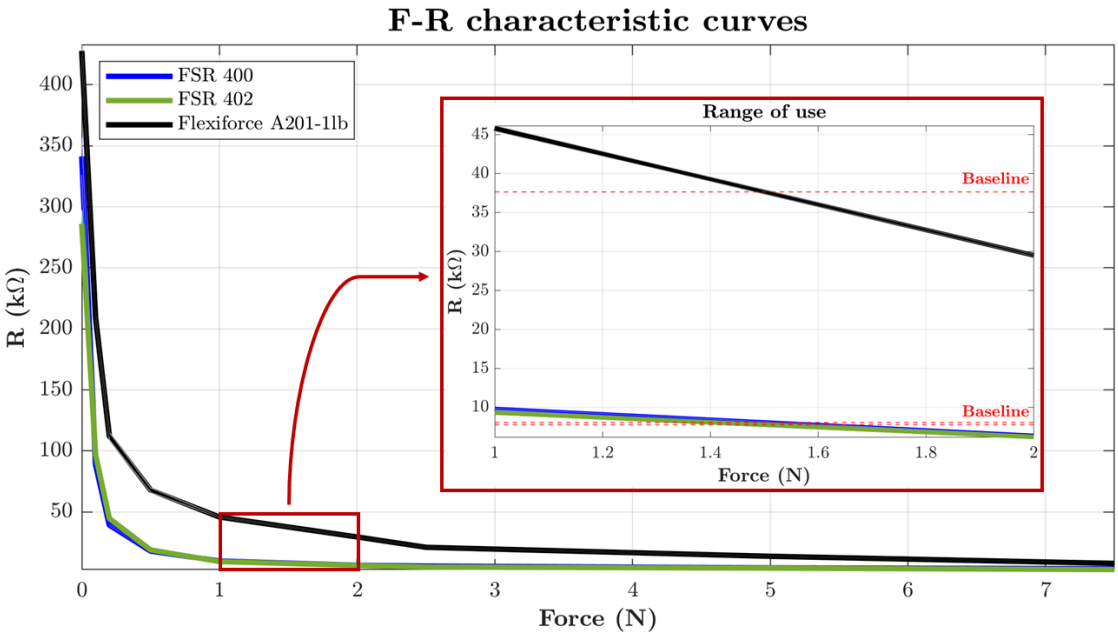

Figure 3.7: Force vs. Resistance characteristic curves for the analyzed sensors.

The characteristic curve of the FlexiForce™ HT201 sensor is not shown as it has very dissimilar resistance ranges (of the order of MΩ) with very high standard deviations. For this reason, the sensor has not been considered in the final choice, although its quality coefficient has been calculated.

Using the coefficient q indicated in Equation 3.1, the following values have been get:

Sensor	q
FSR® 400	30.634
FSR® 402	32.528
FlexiForce™ A201-1lb	69.266
FlexiForce™ HT201	27.552

Table 3.1: Quality coefficient values obtained for each sensor to be characterized.

The greater the q coefficient, the highest amplitude and stability of the response of the sensor will be under a static load.

By analyzing the values obtained, a relative comparison can be made between the various sensors. In particular, it is clear that the best static response among the sensors studied is that of the FlexiForce™ A201-1lb, as it has the greatest

variation in resistance as the force applied varies with a low standard deviation. This results in a very high quality coefficient compared to other sensors.

In order to analyze the dynamic behavior of the various types of FSR, a literature analysis has been conducted on this topic. According to considerations taken up by C. Lebossè et al. [46][47], the FlexiForce thru mode dynamic behavior is not as performant as shunt mode since the signal decreases with time exponentially with a loss that can reach 80% of the sensor's initial response after 20 minutes of dynamic acquisition. This behavior is much less noticeable in shunt mode, then Interlink Electronics FSR sensors appear to be the best option for force detection in dynamic applications.

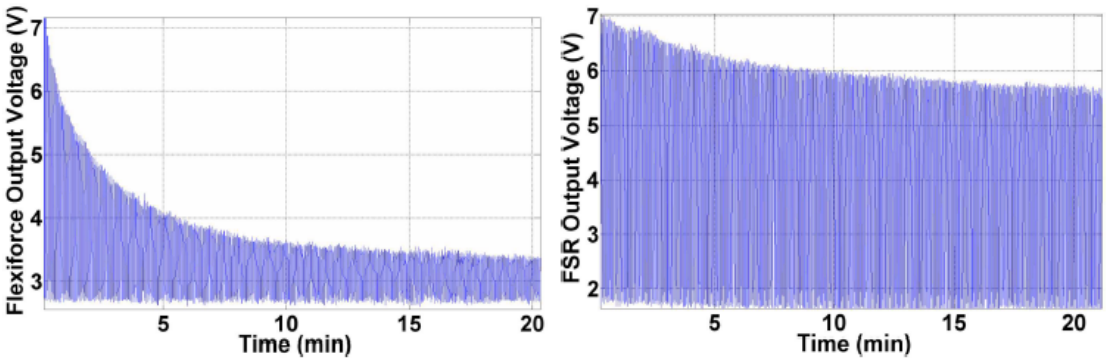

Figure 3.8: Response of the sensor to a sinusoidal stimulation that has been applied for 20 minutes at 0.25 Hz with a force between 1.3 and 4.4 N. [47].

Given the dynamic nature of the pulse wave signal that has to be acquired and the considerations cited, the Interlink Electronics FSR shunt mode has been chosen due to its better response under dynamic loads. The FSR® 402 has been subsequently selected considering the quality coefficient higher than the FSR® 400. The FlexiForce thru mode sensors present interesting static properties, certified by the high quality coefficient obtained for the FlexiForce™ A201-1lb. Hence, these sensors have a better response than FSRs produced by Interlink Electronics for applications with quasi-static conditions, while for dynamic applications the shunt mode is more suitable.

Figure 3.9: FSR® 402 selected for the detection of the pulse waves.

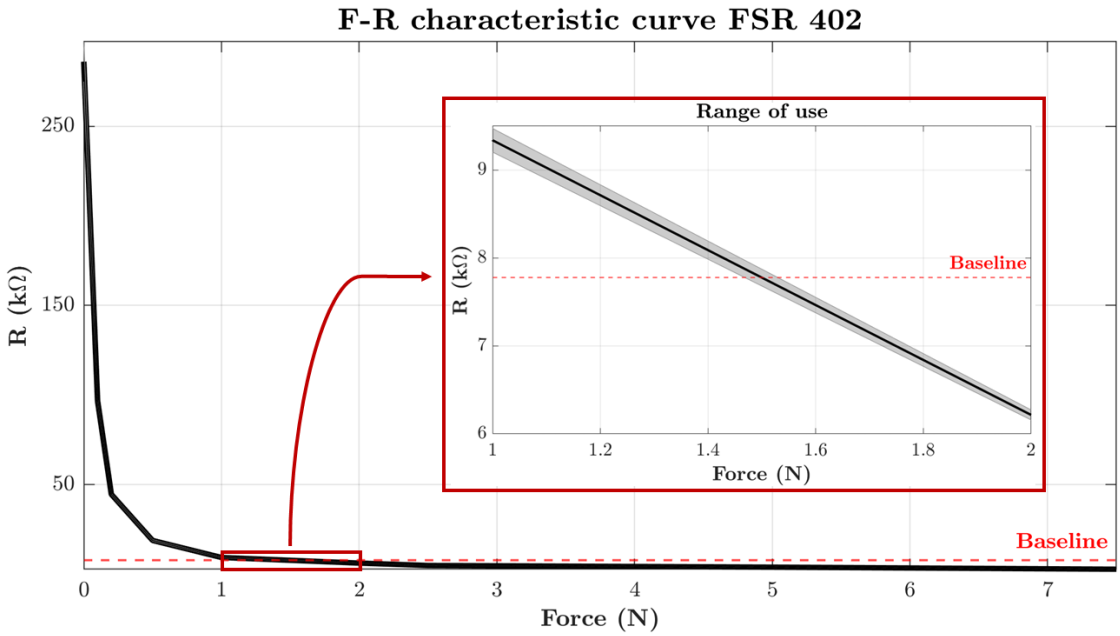

Figure 3.10: FSR® 402 Force vs. Resistance characteristic curve.

Chapter 4

Read-out circuit

This section provides the hardware implementation overview of the designed device for PWV estimation, with components and stages of the read-out circuit that have been investigated and improved to get a high-quality signal, and the relative PCB design.

4.1 Read-out circuit design

The two main components of the read-out circuit for the pulse waves detection are the Discovery Kit STM32F429I, which is the board responsible for the power supply of the conditioning circuit, the acquisition of the sampling data and the communication with the Graphical User Interface (GUI), and the conditioning circuit connected to the board. The two components are analyzed below.

4.1.1 Discovery Kit STM32F429I

The Discovery Kit STM32F429I (shown in Figure 4.1) is an integrated development board which allows users to develop programs and applications with the STMicroelectronics Arm® Cortex®-M4 core-based STM32F429 high-performance microcontroller. The board has a power supply line and a data transmission line via USB, which in the presented device allows to exchange data packets sampled by the MCU with the PC. Either an external 5V power supply or the host PC can provide the power supply via a USB cable to the board. Furthermore, can provide 3V or 5V supply voltage and in the case of this application, the 3V supply voltage has been used to power the entire conditioning circuit that interfaces with the FSR sensor. The adopted Discovery Kit includes a 2.4" LCD and communication

peripherals such as I2C and SPI, as well as numerous GPIO pins. The main peripherals used have been USB for the data transmission, SPI for communication with some components of the conditioning circuit and GPIO pins working as ADC input pins for the signal sampling. The entire acquisition system presented in this thesis is managed by the board.

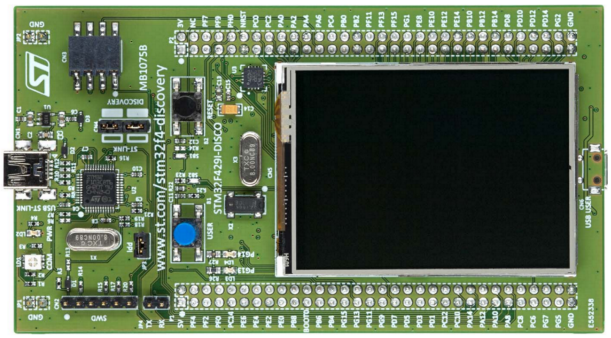

Figure 4.1: Picture of the Discovery Kit STM32F429I [48].

The main peripherals used are described below:

- **Microcontroller unit (MCU)**
  The microcontroller embedded into the Discovery Kit, produced by STMicroelectronics, is the STM32F429ZI [49], based on the Arm® Cortex®-M4 32-bit RISC core, that can operate up to 180 MHz frequency. The Cortex-M4 core features a Floating point unit (FPU) single precision which supports all Arm® single-precision data-processing instructions and data types. The MCU includes high-speed embedded memories as flash memory up to 2 Mbyte and SRAM up to 256 Kbytes. The microcontroller offers up to 17 timers: up to twelve 16-bit and two 32-bit timers up to 180 MHz. It also includes up to 168 I/O ports with interrupt capability and up to 6 SPIs (45 Mbits/s). As advanced connectivity, it implements a USB 2.0 full-speed.

- **Analog-to-digital converter (ADC)**
  The microcontroller offers three 12-bit ADCs and each ADC shares up to 16 external channels. Four of them have been used to sense and convert the voltage from the two FSR conditioning circuits, with two ADC channels for the carotid FSR and two for the femoral FSR. The converted data is stored in a 12-bit variable. Conversions can be made using the single-shot or scan

modes by the three ADCs. Automatic conversion is carried out in scan mode on a predetermined selection of analog inputs. In the device used, the four ADC channels are used in single-shot mode.

- **Serial peripheral interface (SPI)**
  The SPI is a high-speed synchronous serial communication interface that is commonly seen in embedded devices. Devices using the SPI communication protocol interact in full-duplex mode with a single master using a master-slave architecture. The communication mode is, therefore, established by the master device. Individual chip select (CS) can be used to support several slave devices and to select the device with which to communicate. The master sets up the clock at a frequency that the slave device can support, usually up to a few MHz, to start communication. The slave device is subsequently chosen by the master, and the CS line is established. A full-duplex data transmission happens once each SPI clock cycle. While the slave sends a bit on the Master In Slave Out data line (MISO) and the master receives it, the master sends a bit on the Master Out Slave In data line (MOSI). Even when only one-directional data transfer is intended, this sequence is kept. In the full-duplex configuration, the SPI uses a four-wire serial bus, that are:

  – *SCLK*, Serial Clock. It is the output clock set by the master.
  – *MOSI*, Master Out Slave In. It is the data output line from master.
  – *MISO*, Master In Slave Out. It is the data output line from slave.
  – *CS*, Chip Select. It is a line output from the master to indicate slave which to communicate.

  There is also the possibility to use the SPI in half-duplex mode. In this data communication, there is only one data line. The MOSI of the master connects to the MISO of the slave and the line is called DI/O. When communication is bidirectional, the master can not communicate with the slave and vice versa, however when communication is unidirectional, there are no timing issues. So the configuration uses three wires to communicate:

  – *SCLK*, Serial Clock. It is the output clock set by the master.
  – *DI/O*, Data Input/Output. It is the data input and/or output line from both master and slave.
  – *CS*, Chip Select. It is a line output from the master to indicate slave which to communicate.

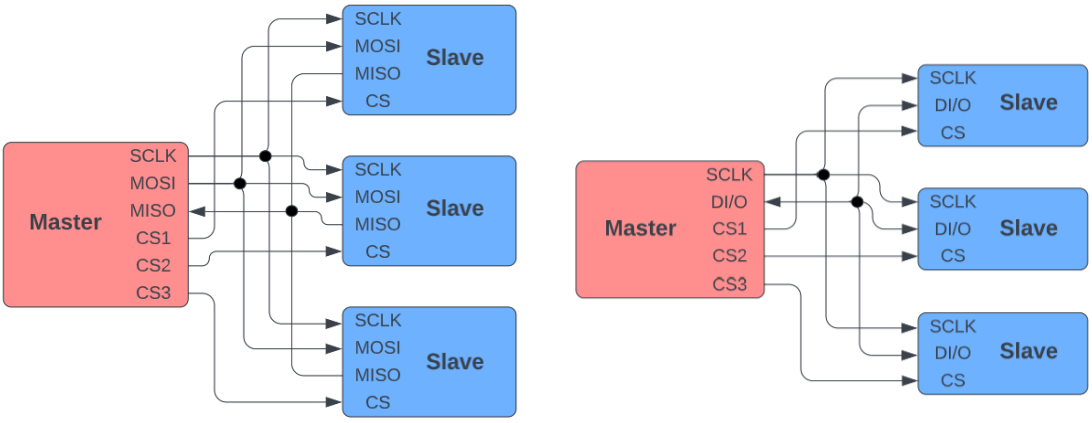

(a) Full-duplex configuration **(b)** Half-duplex configuration

Figure 4.2: Picture of SPI configuration modalities.

SPI communication's main benefit is that it offers fast transmission rates, which lead to high throughput [50].

In this application, SPI has been used in half-duplex mode (only with the Master Out Slave In direction) in order to set the resistance of a digital potentiometer integrated into the system. This communication allows for calibrating the entire system. The calibration mode will be explained in the next sections.

4.1.2 Conditioning circuit

The signal conditioning circuit consists of seven main stages, shown in Figure 4.3.

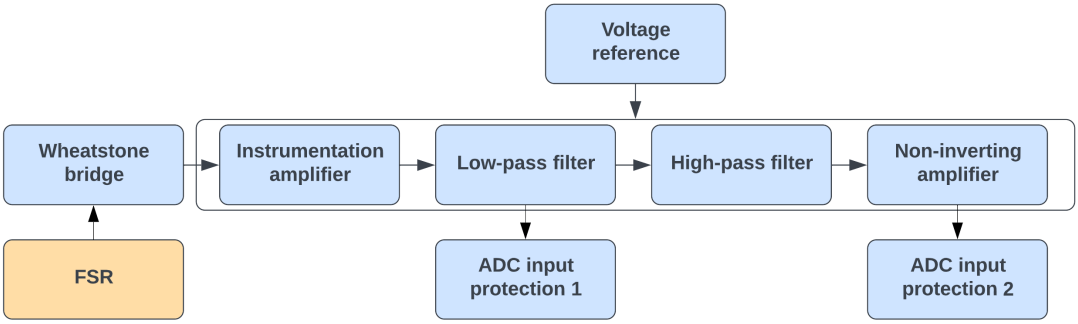

Figure 4.3: Block diagram of the system conditioning circuit. The voltage reference is connected to the instrumentation amplifier, the filter stages and the final amplifier block.

Each stage of the conditioning circuit is analyzed below:

- **Voltage reference**
  A voltage reference is an electronic device that ideally produces a fixed voltage regardless of the device's load, variations in the power supply, changes in temperature, or the passage of time. The voltage reference is useful for working with a mid-range voltage concerning the working dynamic of the ADC of the microcontroller used. By using a mid-range voltage it is possible to work with a single power supply provided by the microcontroller in order to create a wearable, low-consumption device that could be powered directly from a laptop. To make the best use of the ADC dynamic, all signals are centered on the output of the voltage reference. In particular, the dynamics of the ADC of the microcontroller used is 0-3V, consequently the chosen voltage reference supplies a fixed voltage of 1.5V. The 3V single supply voltage is taken from the Discovery Kit. The component that has been used to function as a voltage reference is ISL21080CIH315Z-TK manufactured by Renesas (Tokyo, Japan), which has characteristics that make it ideal for use in general portable applications [51].

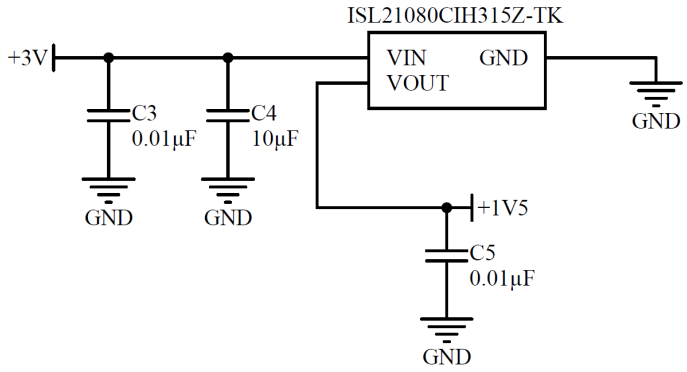

Figure 4.4: Schematic of the voltage reference circuit.

- **Wheatstone bridge**
  A Wheatstone bridge is an electrical circuit consisting of two branches. The overall goal of this circuit is to measure an unknown electrical resistance by balancing the two legs of the circuit, with one of which contains the unknown component. Compared to a simple voltage divider, the circuit provides extremely accurate measurements in resistance measurement. In the case of the device described, the unknown resistance is represented by the FSR transducer and the goal is to record as accurately as possible the variations that the sensor induces on the output voltage from the Wheatstone bridge.

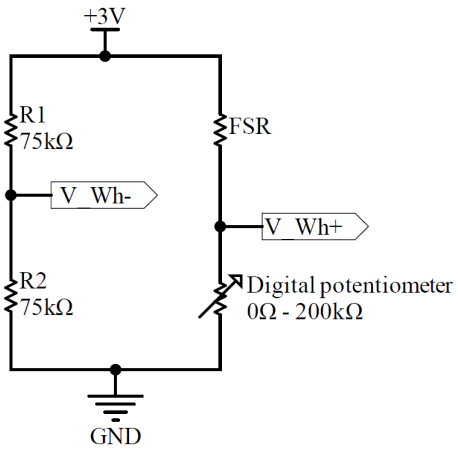

Figure 4.5: Schematic of the Wheatstone bridge circuit.

The equation that describes the output voltage from the Wheatstone bridge is:

$$V_0 = V_{Wh+} - V_{Wh-} = 3V \frac{R_1 R_{POT} - R_2 R_{FSR}}{(R_{POT} + R_{FSR})(R_1 + R_2)} \tag{4.1}$$

In Equation 4.1, R_{POT} represents the resistance of the digital potentiometer in series with the FSR, while R_{FSR} is precisely the resistance of the sensor. Choosing R_1 and R_2 equal to each other the following relationship is obtained:

$$V_0 = 3V \frac{R_{POT} - R_{FSR}}{2(R_{POT} + R_{FSR})} \tag{4.2}$$

Studying the sensitivity (S) of the output voltage from the bridge, the following results are obtained:

$$S = \frac{dV_0}{dR_{FSR}} = -3V \frac{R_{POT}}{(R_{POT} + R_{FSR})^2} \tag{4.3}$$

$$\frac{dS}{dR_{POT}} = -3V \frac{R_{FSR} - R_{POT}}{(R_{POT} + R_{FSR})^3} \tag{4.4}$$

The sensitivity is maximum when its derivative with respect to the variable to be studied (R_{POT}) is equal to zero:

$$\frac{dS}{dR_{POT}} = 0 \Longrightarrow S_{MAX} \rightarrow R_{POT} = R_{FSR} \tag{4.5}$$

Therefore, by analyzing the formulas obtained, it can be deduced that when the resistance of the digital potentiometer is equal to the resistance of the FSR, then the bridge works at the point of maximum sensitivity. The digital potentiometer's inclusion in the system is intended to allow it to be periodically set according to different acquisition conditions and the FSR's working conditions. Regardless of the static pressure applied on the sensor and therefore the resistance shown by it, the Wheatstone bridge thanks to the presence of the digital potentiometer will always be able to work around the equilibrium point by setting $R_{POT} = R_{FSR}$. The problem, therefore, is to measure the resistance of the FSR. This value, given the application in which a dynamic physiological parameter must be taken, is not fixed, but varies over time. For this reason, it is necessary to extract a point resistance value in order to set the digital potentiometer and this is possible through the extraction of a trend resistance (R_{TREND}), obtained by averaging the resistance values of the last 5 seconds of the signal taken. The value of the trend resistance is extracted from the trend voltage (V_{TREND}) sampled after the instrumentation amplifier stage and the low-pass filter stage, and for this it will be illustrated below. The used digital potentiometer is a MAX5424ETA+T produced by Maxim Integrated (San Jose, United States). The full range of resistance is 0-200 kΩ, the wiper position has 256 taps (8-bit register) and can be stored in a nonvolatile memory (EEPROM) and recalled upon power-up or interface command. This resistance range has been chosen as the FSR values for the application studied fall within this range with safety margins. The potentiometer has only one data input line (DIN) and is programmable via SPI since it has an SPI-Compatible Serial Interface up to 5 MHz [52]. To communicate with the potentiometer, SCLK has been set to a frequency of 2.8125 MHz. The serial timing diagram is shown below.

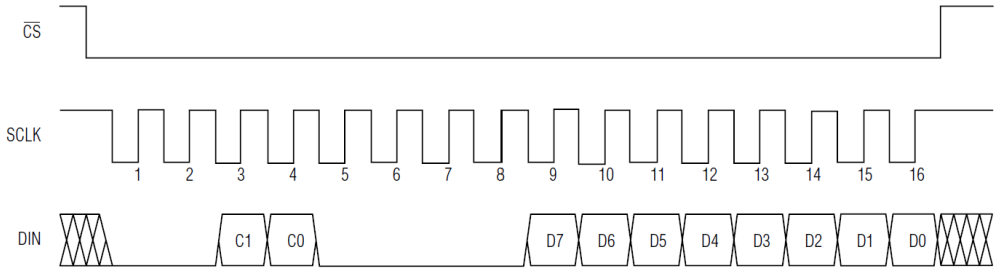

Figure 4.6: MAX5424ETA+T serial timing diagram [52].

The diagram shows how to set a resistance value; the potentiometer becomes sensitive to information when CS is at a low logic level. After that, it needs an 8-bit command indicating the wiper register write instruction (C0, C1

= 00), and an 8-bit value that indicate the value to be set (D0-D7). The entire information is transmitted after 16 clock cycles. In this way, therefore, the system can be calibrated, being able to set the resistance value of the potentiometer and work at the point of maximum sensitivity.

- **Instrumentation amplifier**
  The output voltage of the Wheatstone bridge (V_0) is read through an instrumentation amplifier INA333AIDRGT produced by Texas Instruments (Dallas, United States).

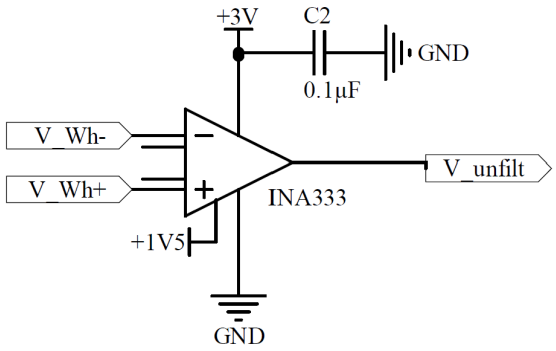

Figure 4.7: Schematic of the instrumentation amplifier circuit.

The used instrumentation amplifier offers a low offset voltage, high common-mode rejection, and excellent precision over the industrial temperature range, making it particularly suitable as a bridge amplifier. Additionally, it has a 50 μA quiescent current [53]. The amplifier has been left with unity gain, so as not to risk the saturation of the signal taken. In addition, the voltage generated by the voltage reference is used to refer the differential output signal to the mid-range of the ADC dynamic. The output voltage from the instrumentation amplifier is:

$$V_{unfilt} = V_0 + 1.5V = 3V\frac{R_{POT}}{R_{POT} + R_{FSR}} \tag{4.6}$$

- **Low-pass filter**
  As for the subsequent filtering and amplification stages, the operational amplifier OPA4347, produced by Texas Instruments (Dallas, United States), has been used. Rail-to-rail input and output, along with low power consumption, are the main characteristics of this operational amplifier, which, when combined with its high speed, ensures the required performances [54]. As regards the low-pass and high-pass filtering stages, the typical frequency range of the

pulse wave signal has been considered, which is on average 0.5-10 Hz. For this reason, a cut-off frequency of 20 Hz has been chosen for the low-pass filter to remove mains interference and any high-frequency noise. In order to select an analog filter with the best introduced delay-attenuation characteristics, numerous configurations of low-pass filters have been simulated on LTSpice®, all with cut-off frequency at 20 Hz. The table below shows the theoretical delay introduced by the filter a decade before the cut-off frequency.

Low-pass filter type	**Theoretical delay (ms)**	**Reverse output**
RC	7.973	-
Sallen-Key	15.947	-
3rd order Sallen-Key	15.950	-
Multiple feedback	15.254	✓
3rd order Multiple feedback	15.777	✓

Table 4.1: Delay introduced by the simulated low-pass filters on LTSpice®.

Considering that multiple feedback filters introduce an inversion of the signal in addition to delaying it and considering the delay introduced comparable to Sallen-Key type filters, the second type of filters has been preferred. Since the attenuation in the 3rd order Sallen-Key filter is much greater than in the RC filter (first order filter) and Sallen-Key filter (second order filter), and considering the delay introduced greater than a negligible amount compared to the other filters, the 3rd order Sallen-Key filter with cut-off frequency at 20 Hz has been chosen as the low-pass filter to be implemented in the system.

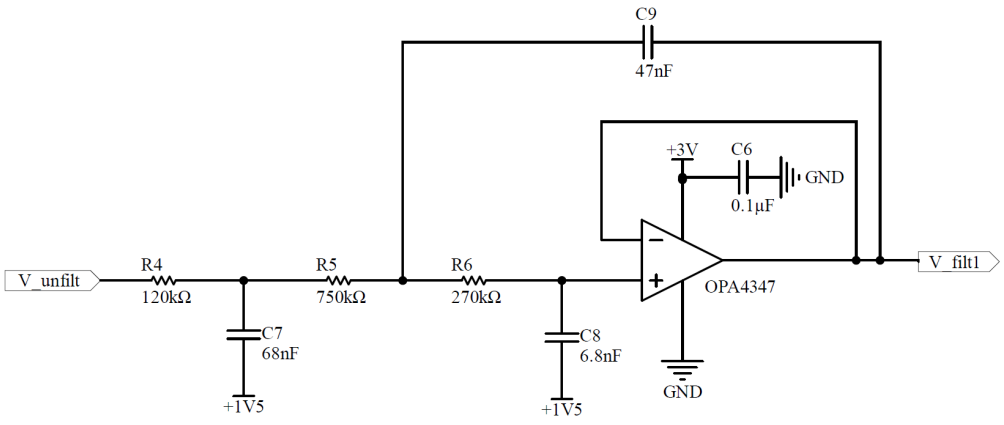

Figure 4.8: Schematic of the 3rd order Sallen-Key low-pass filter circuit.

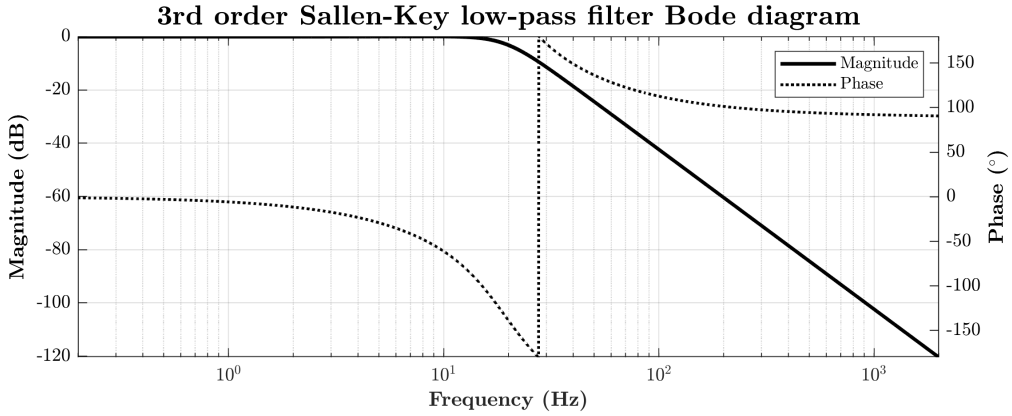

Figure 4.9: Bode magnitude and phase diagrams of the 3rd order Sallen-Key low-pass filter implemented.

As mentioned above, the output voltage at the low-pass filter stage is used to calibrate the system, i.e. to set the resistance of the digital potentiometer. The low-pass filtered voltage maintains the trend of the signal and therefore, having been removed at high-frequency noises, it can be used for the extraction of V_{TREND}. This punctual voltage is then the low-pass filtered voltage averaged over the last 5 seconds of the signal and is used to extract the average FSR resistance (R_{TREND}) of the same time interval. Therefore, using Equation 4.6 and V_{TREND} as the average in the last 5 seconds of V_{filt1}, it results:

$$V_{TREND} = 3V \frac{R_{POT}}{R_{POT} + R_{TREND}} \Longrightarrow R_{TREND} = R_{POT} \left(\frac{3V}{V_{TREND}} - 1 \right) \quad (4.7)$$

Since R_{POT} is initially known, using Equation 4.7 the average resistance of the FSR sensor over the last 5 seconds of measurement is obtained. Knowing R_{TREND} and knowing that by setting $R_{POT} = R_{FSR}$ the Wheatstone bridge works at the point of maximum sensitivity, the value of the digital potentiometer is set via SPI to be equal to the obtained R_{TREND} value. Therefore, to calibrate the system the resistance value to be set for the digital potentiometer is the following:

$$R_{POT\ NEW} = R_{TREND} = R_{POT\ OLD} \left(\frac{3V}{V_{TREND}} - 1 \right) \quad (4.8)$$

Since each time the system is calibrated the new resistance of the potentiometer is saved, the procedure can be performed several times.

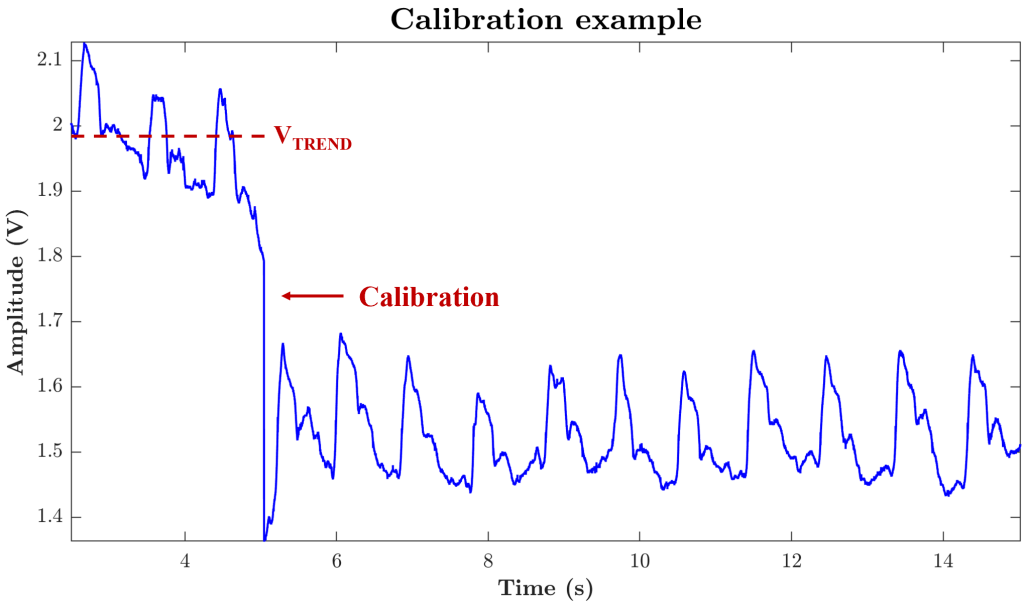

Figure 4.10: Example of a signal trace acquired during the calibration phase. It is noted that initially the signal is not centered at the mid-range voltage of 1.5V, while after calibration the system works at the point of maximum sensitivity.

- **High-pass filter**
  A cut-off frequency equal to 0.2 Hz has been then selected and some filters have been tested to evaluate the delay and attenuation introduced a decade after the cited frequency. The results of the simulations on LTSpice® are shown in the following table:

High-pass filter type	Theoretical delay (ms)	Reverse output
RC	7.699	-
Sallen-Key	15.397	-
3rd order Sallen-Key	16.373	-
Multiple feedback	15.786	✓
3rd order Multiple feedback	15.707	✓

Table 4.2: Delay introduced by the simulated high-pass filters on LTSpice®.

For the same kind of considerations made for the low-pass filter stage, the 3rd order Sallen-Key high pass filter is selected.

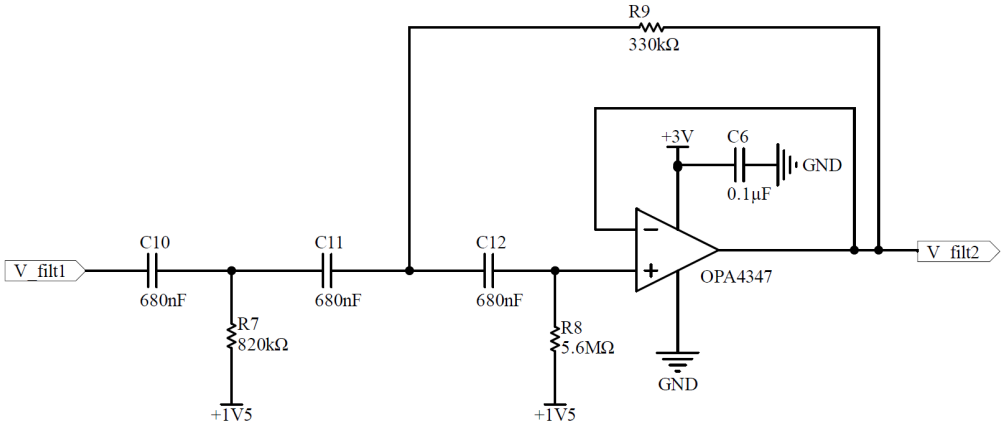

Figure 4.11: Schematic of the 3rd order Sallen-Key high-pass filter circuit.

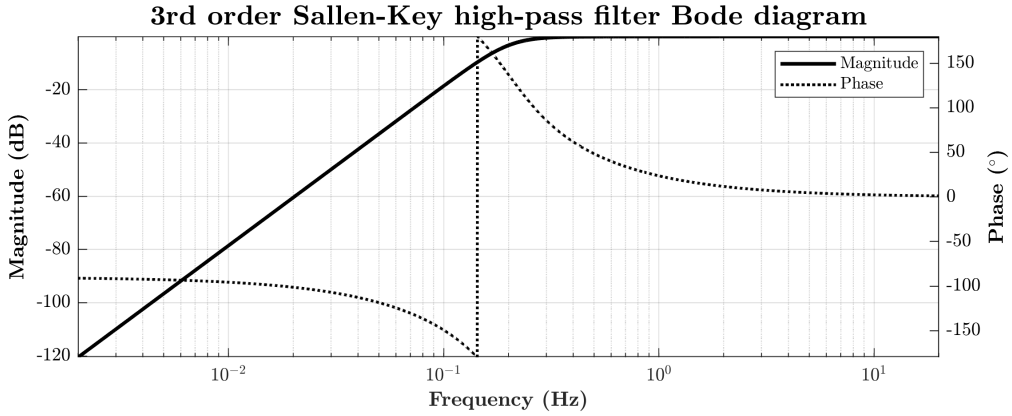

Figure 4.12: Bode magnitude and phase diagrams of the 3rd order Sallen-Key high-pass filter implemented.

- **Non-inverting amplifier**
  With the aim of using a single power supply, it has been decided to implement a non-inverting post-filtering amplification stage, so as not to reverse the sign of the acquired signal. The operational amplifier used is always OPA4347. The non-inverting amplifier's gain is calculated using the following formula:

$$G = 1 + \frac{R_{11}}{R_{10}} \tag{4.9}$$

  To achieve a gain of 2, the resistance values R_{10} and R_{11} have been chosen to be equal (30 kΩ).

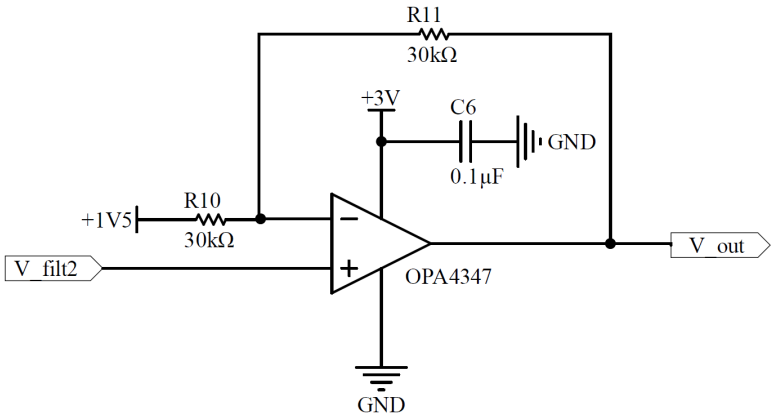

Figure 4.13: Schematic of the non-inverting amplifier circuit.

- **ADC input protection**
  The diodes that have been used in the ADC input protection circuit are BAT42WS Schottky diodes manufactured by Panjit (Taipei, Taiwan). The circuit allows to protect the ADC input from voltage swings too far above the positive rail (3V), or too far below the negative (ground) rail and to avoid damage to the ADC itself. Schottky diodes are typically advised for fast switching because modern ADCs can typically tolerate voltages of at least one or two volts above the maximum voltage and one or two volts below ground without experiencing any negative effects. The idea is, when the input voltage is within the range both the diodes are reverse biased, and only the marginal reverse leakage current flows through them. When the input voltage goes above the positive rail plus forward voltage, the upper diode conducts, and shorts the signal to the upper voltage line. When the input voltage goes below ground minus forward voltage, the lower diode conducts and shorts the signal to the ground line. Hence the ADC never sees out-of-range voltages.

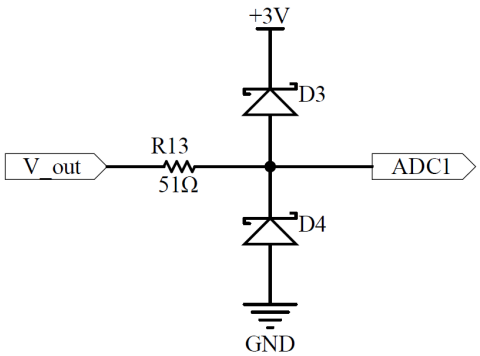

Figure 4.14: Schematic of the ADC input protection circuit.

The same protection circuit is used for the low-pass filtered voltage input into the ADC (voltage used to calibrate the system). In this way, two ADC channels are used for each FSR sensor used.

The overall schematic of the read-out circuit of the system is shown in Appendix A. The read-out circuit is the same for both the carotid FSR and the femoral FSR.

4.2 Printed Circuit Board (PCB) design

In order to reduce the size of the system to make it wearable and to position the Wheatstone bridge as close as possible to the transducer used to minimize any noise due to the wires connection, a Printed Circuit Board (PCB) has been designed using Altium Designer®, as shown in Figure 2.25.

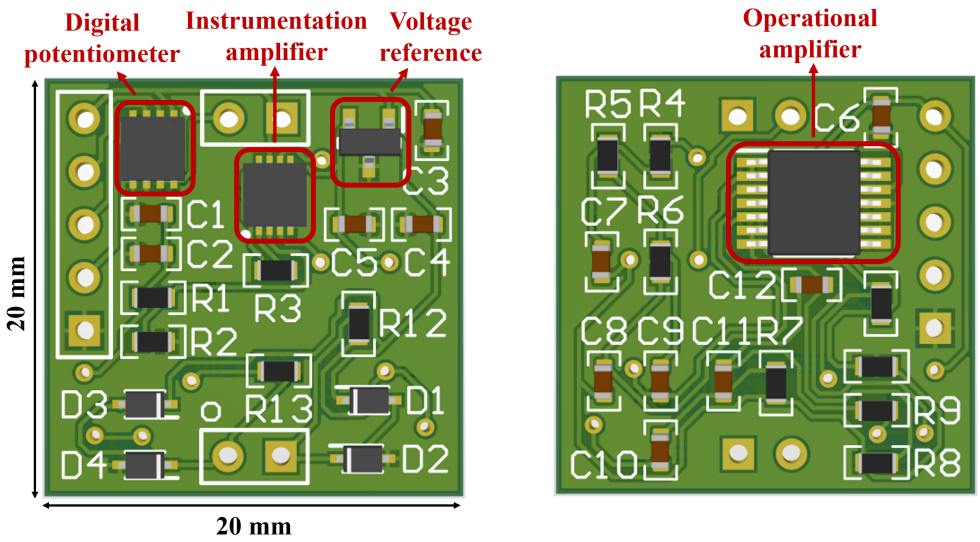

(a) Top layer **(b)** Bottom layer

Figure 4.15: PCB layout with an overview of top and bottom layers.

Since the conditioning circuit is the same for both FSRs, two identical PCBs have been produced for use in the final system, each of which is connected to its own FSR.

Figure 4.15 shows the top layer and the bottom layer of the designed PCB, and the main components are indicated. The dimensions of the PCB are 20mm x 20mm, so the overall size of the conditioning circuit is very small. On the PCB the presence of 9 headers allows connecting the board with external devices. In particular, 2 headers are used to connect the two ends of the FSR and the other 7

headers interface with the Discovery Kit. Of these 7 headers, 2 are used for the power supply (3V and ground), 2 for the ADC input channels and, finally, 3 for the SPI connection of the digital potentiometer (SCLK, DIN, CS).

The following figure reports the block diagram of the connections between the FSRs, the PCBs, the Discovery Kit STM32F429I and the PC.

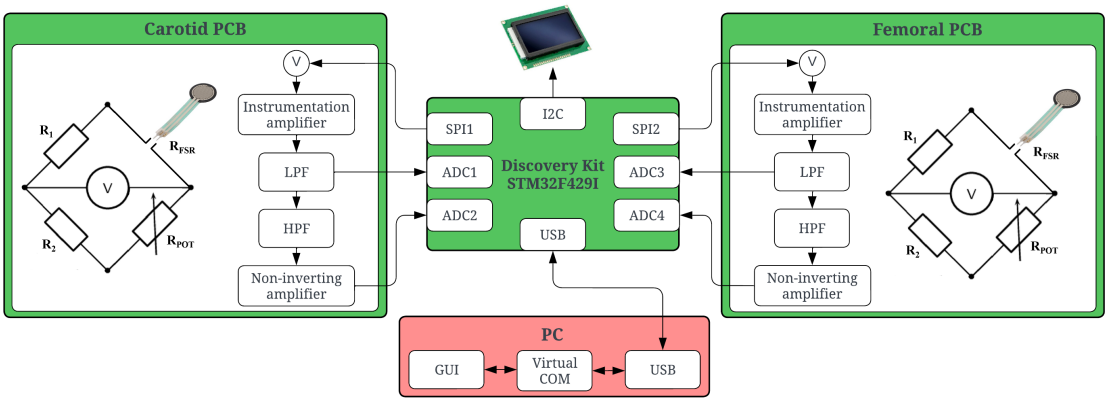

Figure 4.16: Block diagram of the system connections.

Chapter 5

System implementation

In order to acquire the voltages collected by the read-out circuits, a specific firmware has been developed for the Discovery Kit. The entire read-out system has been then incorporated into a holder that optimizes the detection of the pulse wave signal. Furthermore, thanks to the development of a Graphical User Interface (GUI), the acquired data can be displayed in a user-friendly way on a PC. All these aspects are covered in the following sections.

5.1 Firmware implementation

The specific firmware for the application has been developed in C language in the Keil μVision® development environment. The firmware designed for this application manages multiple aspects simultaneously.

Once the device is turned on, i.e. connected the Discovery Kit to the PC via USB, the first step of the implemented firmware is to initialize the peripherals of interest, which are a timer, the three ADCs with the use of 4 channels, two SPI channels and the USB for the data transmission. Subsequently, to avoid finding an unknown resistance set in the digital potentiometer, the command is sent via SPI to set the component with a resistance of 20 kΩ. This value has been chosen as it reflects the mean resistance value of the sensor used in the application of interest. In this way, the system is not too far from the equilibrium point of the Wheatstone bridge. Then the microcontroller waits for a command from the graphical user interface. When the command arrives, the firmware decodes the string and performs the actions, indicated in Figure 5.1.

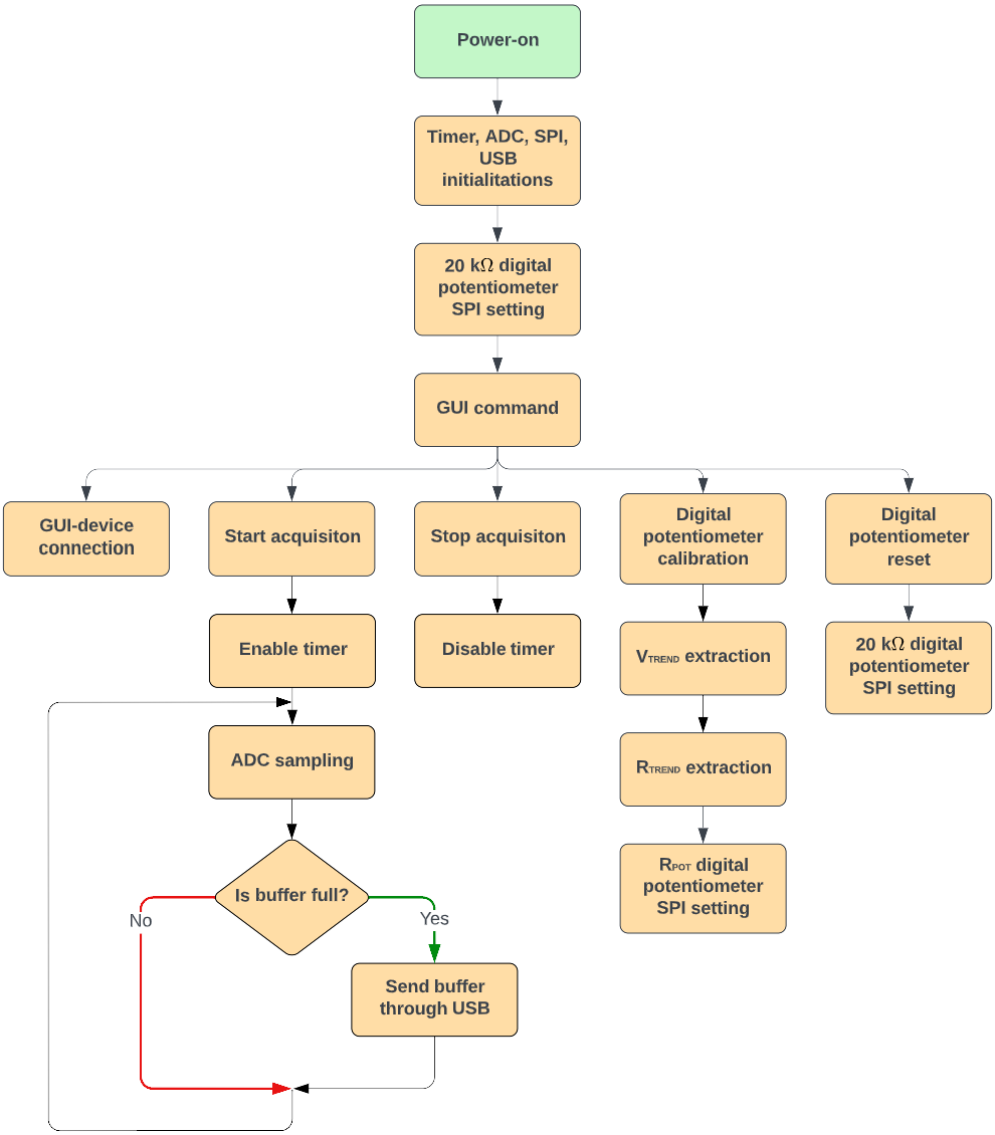

Figure 5.1: Operation diagram of the implemented firmware.

The first command to perform to allow the device-GUI communication is to connect them through an exchange of strings between the two entities, so that there is mutual recognition. If there are no USB communication errors, the connection is made. After that, the acquisition can begin. Using the "Start acquisition" command, the timer that controls the timing of the ADC sampling is enabled. The timer is set to generate an interrupt each 1 ms and each interrupt triggers the sampling of the four ADC channels in sequence. This results in a sampling rate of 1 kHz, with a temporal resolution of 1 ms more than sufficient for this type of

application. The conversion of the ADC generates data of 12 bits length for each sample. When the sampling of the four channels has taken place, the sampled data is stored in a buffer structure, in order to optimize data transmission. In particular, the buffer is filled with the data sampled from the output voltages from the read-out circuits after all the filtering and amplification stages (V_{out}) and with the data of a fictitious sawtooth signal used for debugging. In this way, there are 3 samples to insert into the buffer each timer interrupt. This buffer is the buffer to be sent to the GUI, and is 300 bytes in size, allowing the allocation of 50 samples for each signal (dummy signal, V_{out} carotid FSR, V_{out} femoral FSR) for a total of 150 cells of 16 bits each. The buffer is thus filled every 50 ms and then the transmission takes place via USB. The two voltages obtained after the low-pass filtering stage and used to calibrate the system are sampled and inserted in two separate buffers, as they are data for which there is no need to be transmitted, but are only used to extract R_{TREND}. These two buffers (one for the carotid signal and one for the femoral signal) must store data relating to the last 5 seconds, and for this reason they are composed of 5000 cells (sampling rate of 1 kHz) of 16 bits each.

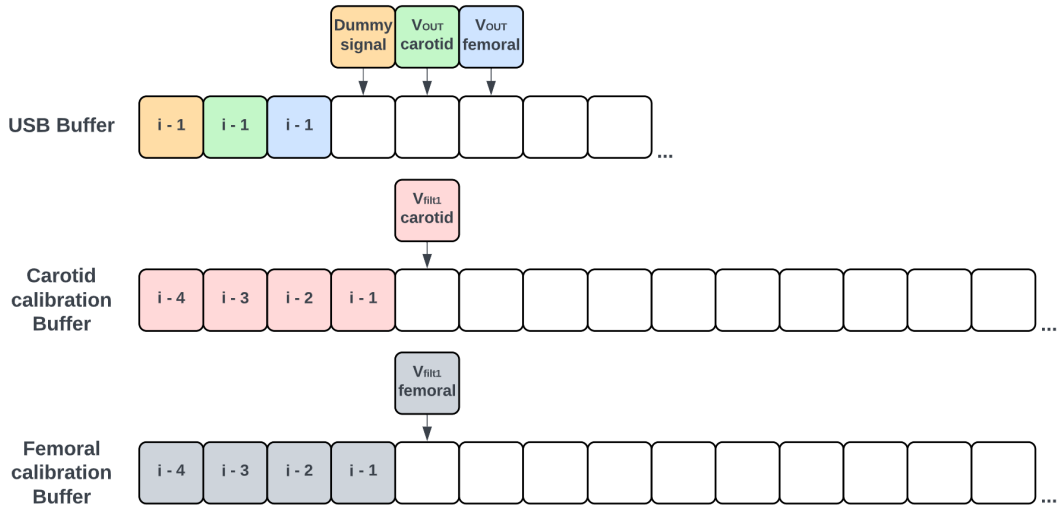

Figure 5.2: Figure of how the buffers used are filled with samples of the various signals at each timer interrupt.

When the acquisition stopping is intended, the timer is disabled and with it also the sampling of the ADC is stopped. The system calibration or reset command can occur in parallel with the acquisition process. In the case of calibration, the firmware uses the 5000 sample calibration buffer to extract the average voltage (V_{TREND}) and then it extracts R_{TREND} through Equation 4.8. After calculating the resistance value to be set to make the system work at the point of maximum sensitivity, it is necessary to transmit the data via SPI to the digital potentiometer.

This procedure is done both for the collection system of the carotid pulse wave and for the femoral pulse wave. The reset command, on the other hand, allows to simply send the default value of 20 kΩ to the digital potentiometer.

Being implemented in this way, the firmware allows the data collected to be transmitted in an optimized way through a buffer structure and allows it to be flexible to any type of command received by the operator through the GUI.

5.2 Holder design

Two holders have been developed, one for the sensor that detects the carotid pulse wave and one for the femoral sensor, with the goals of making the acquisition of PWV wearable and of obtaining pulse waves with adequate quality. The two holders have buttonholes so that they can be used with elastic bands to be wrapped around the neck and the pelvis, respectively. This makes the application wearable because the clinician only needs to place the sensors on the sampling sites. The holders' design has been developed in SolidWorks and then they have been printed with the 3D printer Form3.

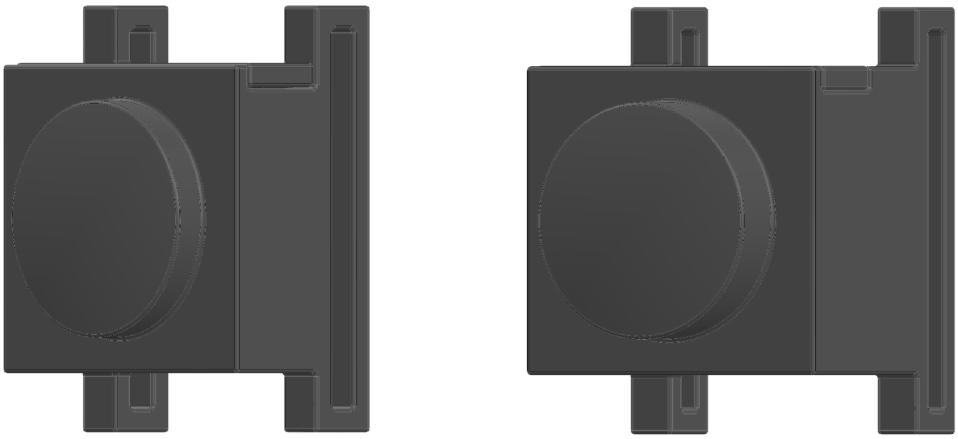

(a) Carotid FSR holder **(b)** Femoral FSR holder

Figure 5.3: Picture of FSR holders.

The holder includes a convex circular thickness on which the FSR sensor is attached. The circular thickness is convex to allow the flexible sensor to better adhere to the subject's skin. Attached to the extent there is a case that serves to hold the PCB, which in turn is connected to the FSR sensor. Being the FSR flexible, it can be easily soldered directly to the PCB and, through a small hole in the upper part of the holder, it can come out of the case to attach to the convex

support. At the bottom of the holder there is a larger hole that allows the wires connected to the PCB to come out and connect to the Discovery Kit.

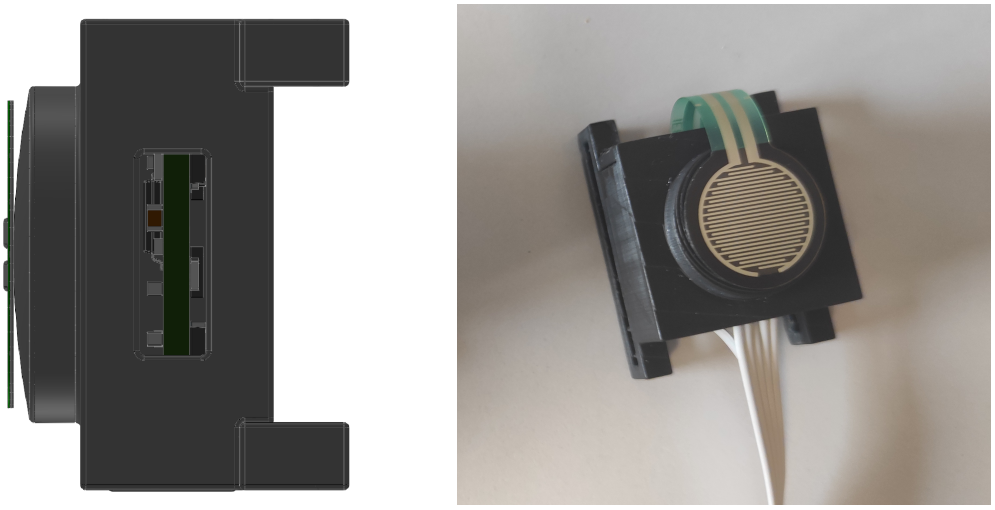

(a) Bottom part of the holder. It is visible the hole for the wires, the circular thickness and the FSR.

(b) Fully assembled holder.

Figure 5.4: Image of the holder's details and the assembled system.

The important function of the circular thickness is to apply the static pressure necessary for the FSR to have acceptable resistance values suitable for the type of application. For this reason, as can be seen in Figure 5.3a and 5.3b, the total thickness of the carotid holder is different from the femoral one. The height of the femoral holder (both of the circular thickness and of the PCB case) is greater as the amplitude of the pulse wave on the femoral site is generally reduced due to the presence of more evident soft tissues compared to the carotid site. To ensure that greater static pressure is applied to cope with this physiological problem, the total thickness of the femoral support is therefore greater.

Holder	**Circular thickness (mm)**	**PCB case (mm)**	**Total thickness (mm)**
Carotid	4	11	15
Femoral	6	19	25

Table 5.1: Thicknesses of the holders.

5.3 Graphical User Interface (GUI) design

The user can easily interact with the device thanks to the Graphical User Interface (GUI) that is implemented in the Microsoft Visual Studio environment in C#. It has been created with the help of the declarative markup language XAML. When used with the .NET Core programming model, XAML streamlines the process of developing an app's user interface. The primary purpose of the GUI is the real-time signal display, which provides immediate feedback on the accuracy of the sensor placement and the quality of the acquired pulse waves. Secondly, the GUI allows saving the data relating to the pulse waves received on the USB port for subsequent analysis, in particular, to extract the PWV parameter afterward.

Since the signals from the femoral and carotid sites are collected simultaneously, there are two main dedicated graphs on the interface. it is also possible to display a graph showing both the acquired pulse waves at the same time and a graph showing the fictitious signal sent by the MCU to verify that the transmission takes place correctly.

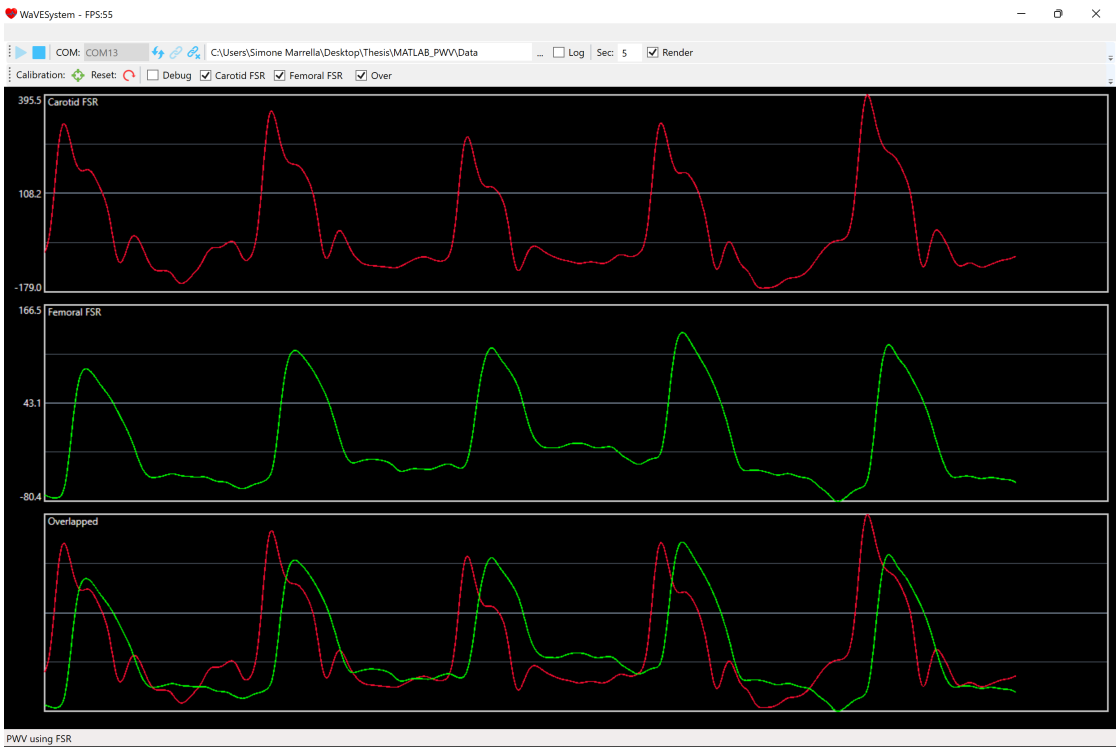

Figure 5.5: Figure of the main window of the GUI implemented. The screen displays the toolbar at the top, two graphs for the carotid and femoral pulse waves, and a graph showing the overlap of the two signals.

The first step to be carried out in order to show the received data is the creation of a virtual COM, performed by the interface itself. Subsequently, through the choice of the COM and the connection with the device (GUI-device connection shown in Figure 5.1), by pressing the "Start" button the interface receives the data buffer of 300 bytes every 50 ms via USB, which has the structure shown in Figure 5.2. If the "Log" button is checked, the interface allows saving the input buffer with the same structure as it arrives in a binary file (.bin). This binary file is the one that will then be used to extract the PWV parameter through a post-processing algorithm on MATLAB®. At the same time, the interface allows showing the signals present in the incoming buffer in the graphs, reorganizing the packets and filling the appropriate buffers. In particular, there are three buffers, one for each signal of interest (dummy signal, carotid pulse and femoral pulse) which are filled by extracting the samples from the buffer arriving on the USB. The rearrangement of the incoming buffer is shown in the figure below.

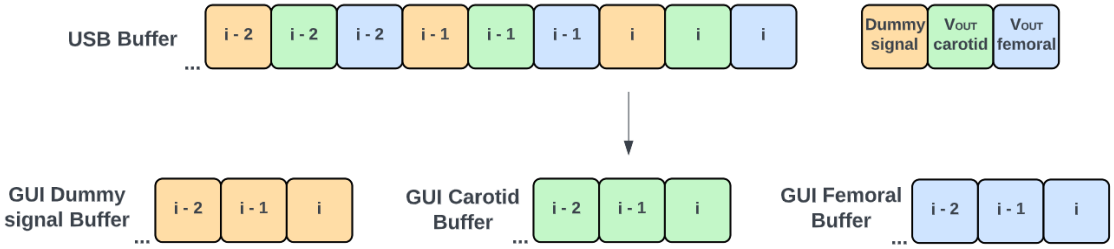

Figure 5.6: Image showing how the GUI rearranges the incoming buffer to display the data.

Before being shown, the data is digitally filtered to allow a better visualization with a low-pass filter with a cut-off frequency of 10 Hz and a high-pass filter with a cut-off frequency of 0.5 Hz. Both filters are Butterworth filters of order 4.

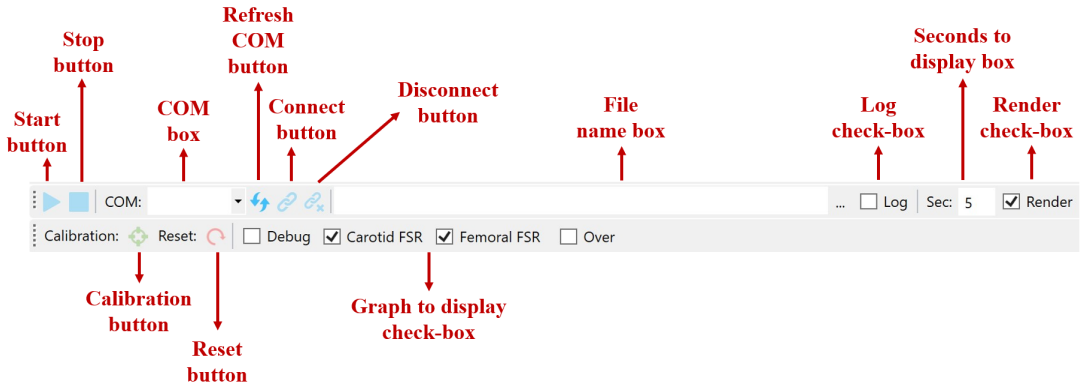

Figure 5.7: GUI toolbar with a focus on each button present.

Another fundamental interaction that can be done with the GUI is to calibrate or reset the system using the two dedicated buttons “Calibration” and “Reset”. Using these two commands, the firmware activates the routines explained in the section 5.1 for setting the resistance of the digital potentiometer.

Therefore, using the toolbar shown in Figure 5.7, the GUI allows for visualizing the signals, saving the data of the pulse waves arriving from the acquisition system and adapting to the clinician’s requests to enable efficient use.

The entire scheme of the device is shown in the figure below after analyzing all of the points to be developed for the proposed device.

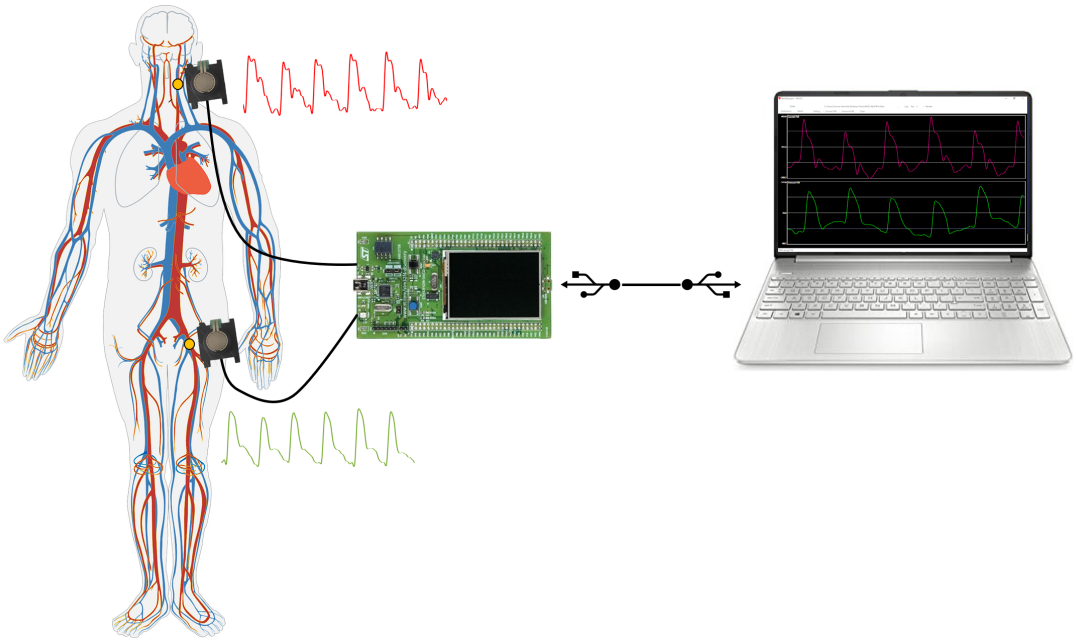

Figure 5.8: Device scheme. It is noted the two holders, that contain the PCBs, with the respective FSRs. The two sensors are connected to the Discovery Kit which manages the acquisition and communicates via USB with the GUI, which is run on the PC.

Chapter 6

Results and discussion

This chapter is divided into two sections. The first part explains the algorithm for the PWV extraction starting from the collected pulse waves. The second part shows the experimental protocol and the clinical tests for the validation of the system. The validation has been performed in collaboration with the hospital "A.O.U. Città della Salute e della Scienza" in Turin. The analysis of the data and results obtained are then presented.

6.1 Intersecting tangent method

In order to extract a PWV value, it is necessary to extrapolate from each heart cycle the characteristic that allows detecting the passage of the pulse wave due to the heartbeat. The intersecting tangent method is the most well-known technique used in literature, and it delivers the most reliable and consistent outcomes [55]. The intersecting tangent method extracts the intersecting tangent point (ITP), also known as the "foot" of the signal. ITP corresponds to the point obtained by projecting on the signal the intersection between the tangent to the point of maximum first derivative, identified during the systolic rise and the horizontal line passing through the minimum during the late diastolic phase and before the beginning of the systolic upstroke [35]. By extrapolating the foot of the carotid pulse wave and the foot of the femoral pulse wave it is possible, for each cardiac cycle, to calculate the differential PTT. The time interval between the ITP detected on the femoral arterial pulse wave and the ITP of the carotid pulse wave is the differential PTT:

$$PTT = t_{ITP\ femoral} - t_{ITP\ carotid} \tag{6.1}$$

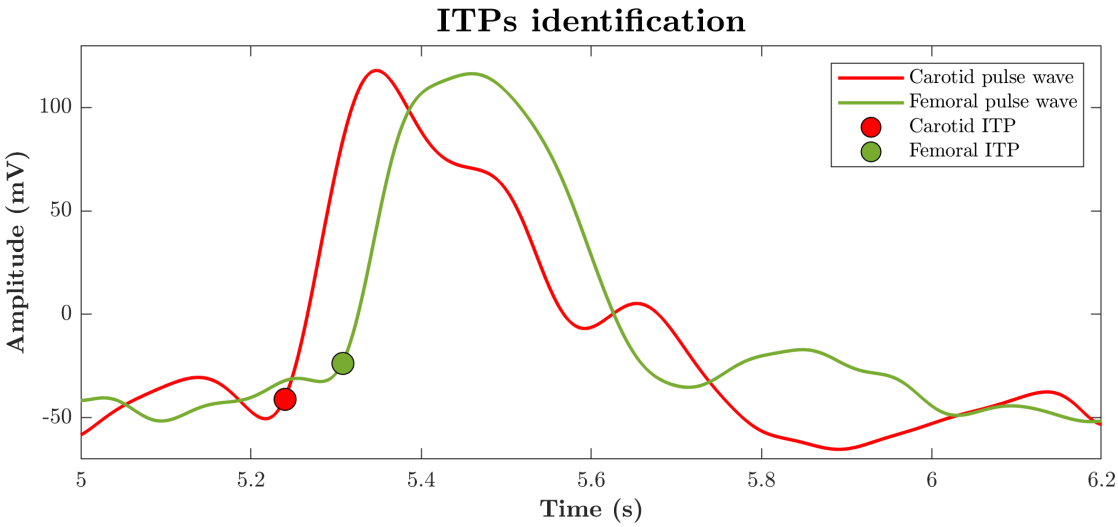

Figure 6.1: Figure showing a cardiac cycle and the two identified ITPs, one for the carotid artery signal and one for the femoral artery signal.

The intersecting tangent algorithm is implemented in MATLAB® using the binary file (.bin) generated by the GUI during the signal acquisition and includes the following steps:

1. **Pre-processing**
   The pulse waves saved in the binary file are read, then remove the last 2 seconds and extract 10 seconds of signal, as done in commercial devices. These signals are the ones that will then be used by the ITP extraction algorithm. Subsequently the carotid and femoral signals are digitally filtered through IIR filters to remove low frequency trends and high frequency noise. The cut-off frequencies used are 0.5 Hz for the high-pass filter and 10 Hz for the low-pass filter. Zero-phase forward and reverse digital filtering is used to avoid adding distortion to the signals.

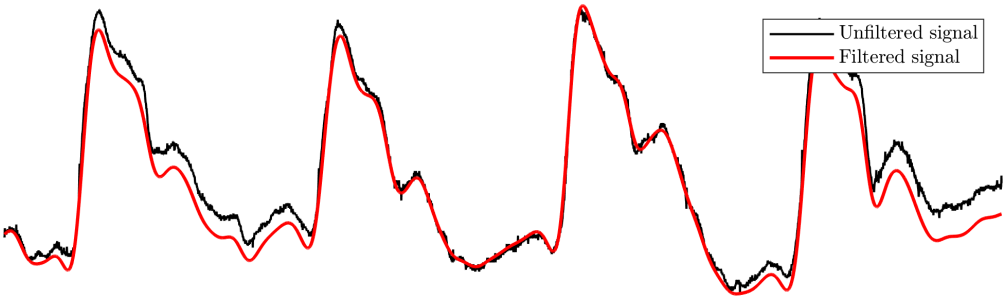

Figure 6.2: Signal obtained after pre-processing filtering.

2. **Event starters detection**
   In order to calculate the number of blood pulses, or events, that have occurred in the pulse wave being evaluated, the original signal is low-pass filtered with a filter at a cut-off frequency of 1.5 Hz. The relative minimums of the low-pass filtered signal are the event starters, which correspond to the array indices that identify the initiation of blood pulses. Once the instants of the heartbeat's onset have been determined, the average of the intervals between the event starters can be used to calculate the duration of the cardiac cycle (T).

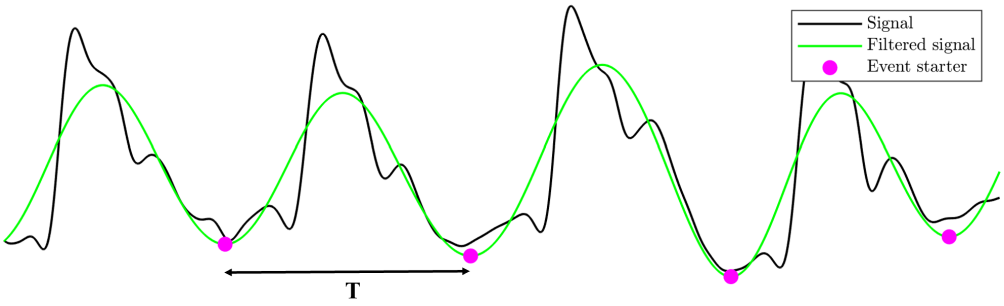

Figure 6.3: Event starters detection and cardiac cycle evaluation.

3. **Minimum selection**
   Only a $\pm T/3$ signal portion, starting from each event starter previously detected, is taken into account. The local minimum just before the systolic upstroke, which is the closest to the edge's maximum slope and serves as the best minimum for the extraction of intersecting tangent algorithm features, is selected after finding all of the minimums in this interval. If there are some minimums found in the interval that are greater than the 40% threshold of the lowest minimum's y-coordinate among all those found, they are not taken into account. The presence of multiple relative minimums before each systolic upstroke is due to the fact that the signal has local oscillations and noise.

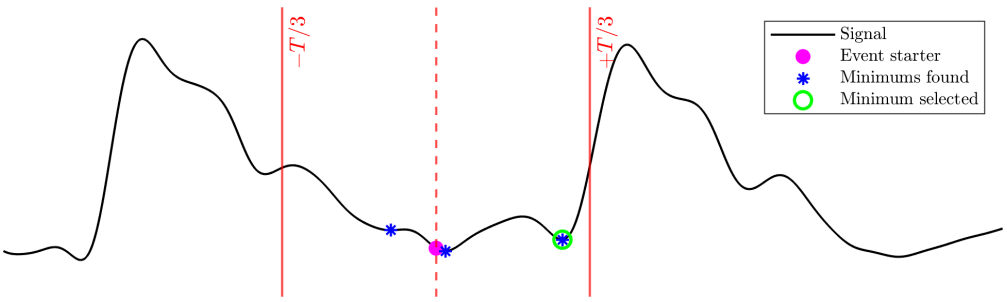

Figure 6.4: Identification of the minimum points in the studied interval and selection of the best minimum.

4. **Maximum derivative point identification**
   In this step, each blood impulse has to be considered separately in order to then proceed with the extraction of the ITP for each cardiac cycle. For this reason, a window of length equal to T has to be examined separately starting with each event starter. Analyzing the signal in this window and based on each relative minimum extracted in the previous step, the first derivative is calculated and then the point where the first derivative is maximum is found. Finally, the tangent passing through the identified point is drawn.

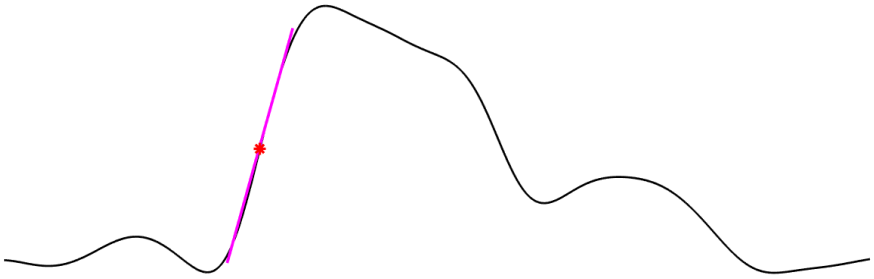

Figure 6.5: Identification of maximum point of first derivative and tangent through the point.

5. **Intersecting tangent point extraction**
   After obtaining the tangent passing through the maximum of the first derivative and tracing the horizontal line passing through the minimum identified previously, the x-coordinate of the intersection of the two straight lines can be achieved. By projecting on the signal the point of the intersection of the two lines, the foot of the wave is obtained. The x-coordinate of the ITP is indicative of the timing of the pulse wave passage.

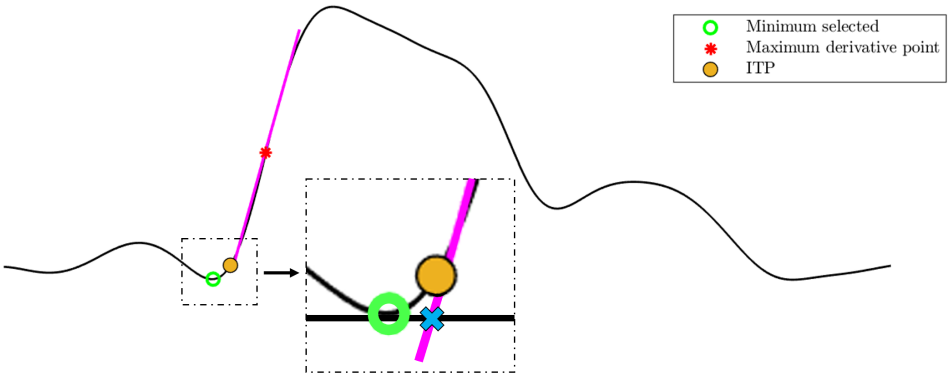

Figure 6.6: Intersecting tangent point (ITP) extraction.

After extracting the ITPs for each cardiac cycle for both the carotid and femoral pulse waves, three checks are carried out to eliminate any ITP erroneously detected:

- The first test is performed on the number of ITPs detected. In particular, it is verified that the number of carotid ITPs detected is equal to the number of femoral ITPs.
- The second test is done to verify that each femoral ITP arrives after its associated carotid ITP. This investigation is executed for a physiological obviousness, since the carotid pulse wave always precedes the femoral pulse wave.
- The last test verifies that two successive carotid ITPs are not too far apart. In particular, it is verified that the next ITP falls within the mean range plus standard deviation of all carotid ITPs compared to the previous ITP.

At the end of the checks performed, there is an ITP number for the carotid pulse and an ITP number for the associated femoral pulse. Using Equation 6.1, it is possible to calculate a PTT value for each heartbeat and, having measured the PWD, obtain the relative PWV value. Since more than one heartbeat is present in the signal being analyzed, more PTT values are available for each measurement, allowing for the calculation of a PTT's average value and standard deviation.

After calculating the mean value and standard deviation of the PTT, an exclusion method is implemented in order to obtain more accurate results. In particular, the method provides for a check for each individual PTT value obtained. PTT values that comply with the following formula are discarded:

$$|PTT_i - PTT_{mean}| \geq 0.9 \cdot PTT_{std} \tag{6.2}$$

In this way, by eliminating anomalous values or values that are further away from the mean value, a more accurate and stable PTT value is obtained and this is automatically reflected on the PWV value.

6.2 Clinical tests

The system has been tested and validated on 28 volunteer subjects at "A.O.U. Città della Salute e della Scienza di Torino", comparing the obtained results with those provided by SphygmoCor® in a trial authorized by the "University of Turin Bioethical Committee". Subsequently, a statistical analysis has been executed comparing the results obtained by the two devices used and evaluating the goodness of the measurements acquired with the device presented which uses FSR.

6.2.1 Experimental protocol

For each subject, two clinical operators switched between the two instruments to complete the cfPWV acquisitions. After updating the anamnesis data, the two operators use tactile arterial palpation to determine the ideal carotid and femoral locations. To prevent the acquisition sites for the two instruments from shifting after they are found, the two locations are marked. The femoral-carotid distance is then measured using a measuring tape. PWD is obtained by multiplying the directly measured distance by a constant of 0.8 and it stands for a more accurate representation of the real arterial pathway. At this point, the two-steps acquisition with SphygmoCor® is performed, with the first operator taking the carotid pulse first and then the femoral pulse. Next, the second operator uses the FSR device to perform simultaneous acquisition of the femoral and carotid arteries. The FSR device is positioned on the subject using two elastic bands, as shown in Figure 6.7b. This type of use makes the application quickly wearable, involving the operator only in the correct positioning of the sensor at the beginning. After the correct placement, the system is calibrated, the pulse waves are acquired and PWV is calculated afterwards.

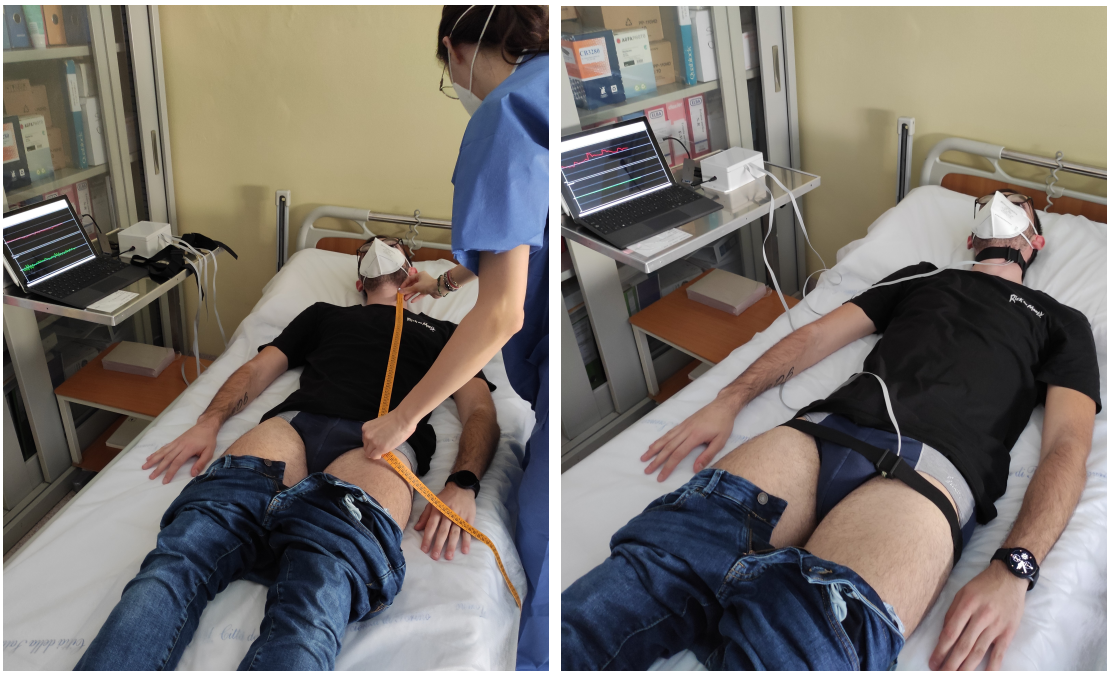

(a) Direct distance measurement between the two collecting sites.

(b) Acquisition of pulse waves using the wearable configuration.

Figure 6.7: Picture of the main steps of the experimental protocol for the FSR device.

For statistical reasons and to be consistent with standard clinical PWV evaluation practices, this procedure is repeated three times on each subject. Indeed, the average of three consecutive acquisitions is what clinicians typically consider to be the actual PWV value. For each FSR device acquisition, the implemented intersecting tangent algorithm allows to generate a report that contains all the data of the subject, the acquired pulse waves and the calculated PWV value. This allows making a quick comparison with the values obtained by SphygmoCor®.

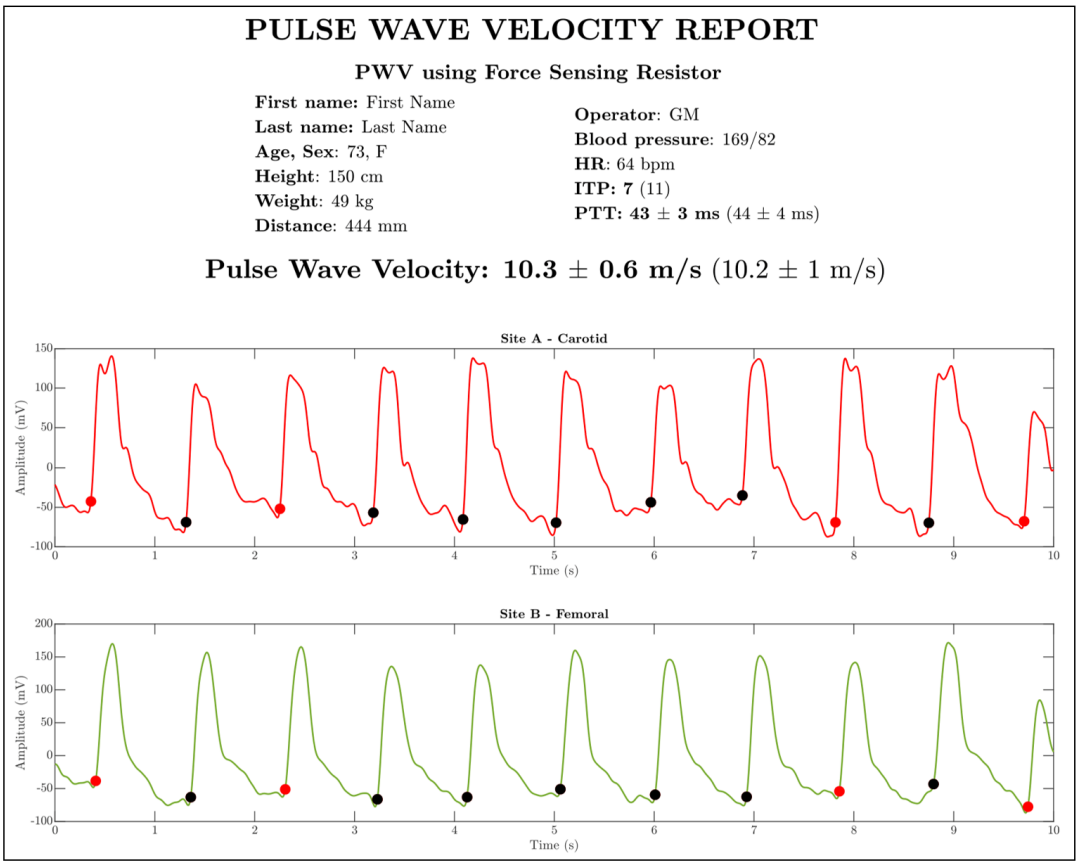

Figure 6.8: Example of a report generated for the PWV estimation. It is noticed the ITPs considered for the calculation of the PWV (in black) and the ITPs discarded for the criterion of Equation 6.2 (in red).

6.2.2 Results and statistical analysis

The following table shows the physiological parameters of the population under evaluation and the relative results regarding the PWV estimation obtained by the device using FSR and SphygmoCor®. The results are presented as the mean value and standard deviation of the three acquisitions made for each device.

Subject	Age	Gender	Weight (kg)	Height (cm)	FSR (m/s)	SphygmoCor® (m/s)
1	41	M	75	179	6.1 ± 0.3	6.8 ± 0.4
2	32	F	73	173	5.6 ± 0.2	5.9 ± 0.4
3	24	M	72	179	6.7 ± 0.2	6.3 ± 0.2
4	24	M	73	181	6.1 ± 0.2	6.2 ± 0.3
5	68	F	125	166	8.8 ± 0.6	9.5 ± 0.9
6	64	M	70	167	7.4 ± 0.8	8.2 ± 0.6
7	63	F	72	156	9.0 ± 0.5	9.7 ± 0.7
8	57	M	103	171	7.1 ± 0.7	7.7 ± 0.3
9	47	F	79	163	5.8 ± 0.7	6.2 ± 0.4
10	48	M	65	171	7.8 ± 0.5	7.6 ± 0.4
11	48	F	57	159	7.6 ± 0.5	7.7 ± 0.6
12	50	F	50	158	6.7 ± 0.3	6.4 ± 0.4
13	50	F	65	157	8.3 ± 1.4	8.7 ± 0.7
14	74	F	52	147	11.3 ± 2.1	11.6 ± 1.7
15	75	M	87	165	7.1 ± 1.4	7.5 ± 0.3
16	56	F	60	162	6.3 ± 0.4	5.9 ± 0.3
17	63	F	83	183	7.8 ± 1.0	8.1 ± 0.8
18	60	F	76	166	7.1 ± 0.6	7.4 ± 0.7
19	63	F	79	164	7.0 ± 1.5	6.6 ± 0.8
20	21	M	69	169	6.8 ± 0.7	6.4 ± 0.5
21	56	F	70	173	7.2 ± 0.7	7.4 ± 0.4
22	54	F	83	155	7.8 ± 0.7	7.5 ± 0.7
23	63	M	89	171	9.5 ± 1.0	9.9 ± 0.8
24	73	F	49	150	9.3 ± 1.4	10.0 ± 0.6
25	59	F	73	155	9.6 ± 2.0	9.2 ± 0.8
26	19	F	50	162	5.8 ± 0.3	6.6 ± 0.3
27	28	M	63	168	7.1 ± 0.7	6.7 ± 0.5
28	28	F	61	162	6.6 ± 0.6	5.9 ± 0.3

Table 6.1: Table containing the data for each patient and the PWV estimation obtained as the average of the three measurements for both devices used.

From the table, it can be seen that cfPWV values are comparable with those obtained by the gold standard for estimating PWV in the clinic.

In order to obtain an objective measure of the goodness of the results obtained

from the device that uses FSR, a statistical analysis has been carried out. Figure 6.9 reports the mean values and standard deviations, represented as error bars, of the PWV measurements. From the graph it is observed how the results obtained are highly comparable, noting how the measurement ranges of the two instruments are, in most cases, overlapping. It is noted that also the standard deviation of the measurements of the device using FSR are comparable to those of the gold standard, showing excellent repeatability. Higher standard deviations are seen for higher mean PWV values, and this is a behavior that affects both devices. For some subjects, however, the standard deviation is greater than in SphygmoCor®, and this can be explained as the application presented in this thesis is wearable and therefore is more affected by motion artifacts that influence the repeatability of some measurements.

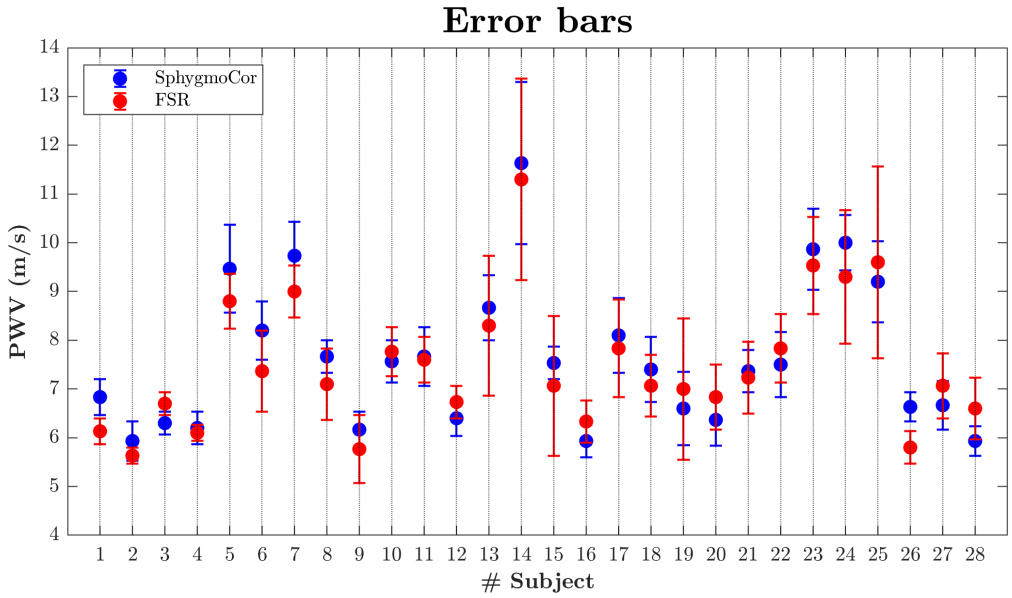

Figure 6.9: Picture of PWV mean values and standard deviations for the subjects undergoing analysis. Standard deviations are indicated by the error bars.

The linear correlation calculated using the final PWV data supplied by both devices is then shown in Figure 6.10 in the scatter plot. A scatter plot can infer different kinds of correlations between two variables with a specific confidence interval. Using best-fit methods, it is possible to derive an equation for the correlation between the variables. Of the various best-fit methods, linear regression is the best approach for a linear correlation. The coefficient of determination (R^2), which is derived from the linear model, is the proportion of the variation in the dependent variable that is predictable from the independent variable. This coefficient is equivalent to the square of the correlation coefficient between two

variables, so the closer it is to 1, the more correlated the two variables are. The high R^2 coefficient calculated, equal to 0.905, indicates a strong linear correlation between the two devices.

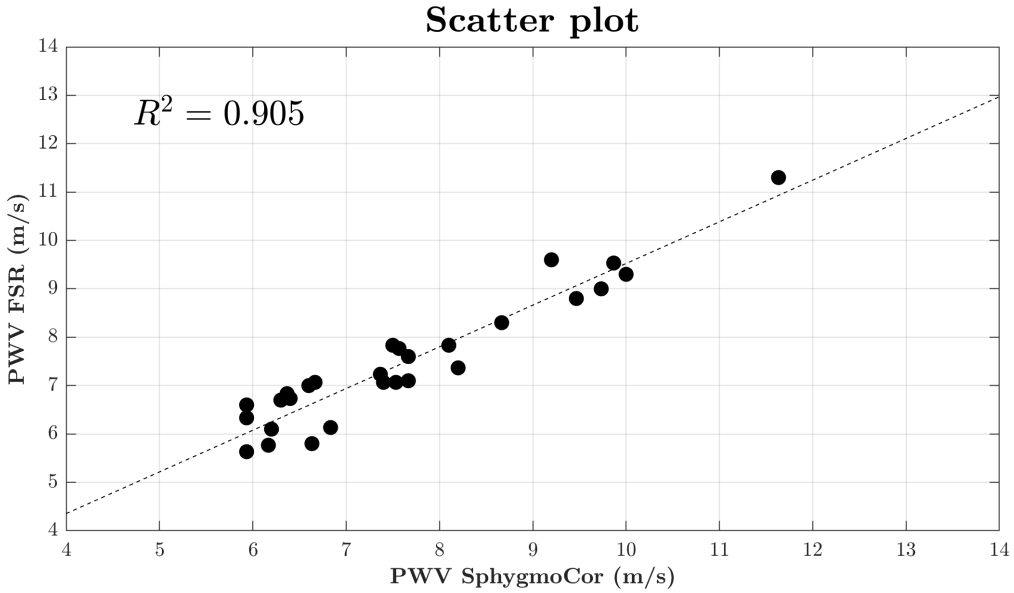

Figure 6.10: Scatter plot with PWV values acquired by the two devices across all subjects.

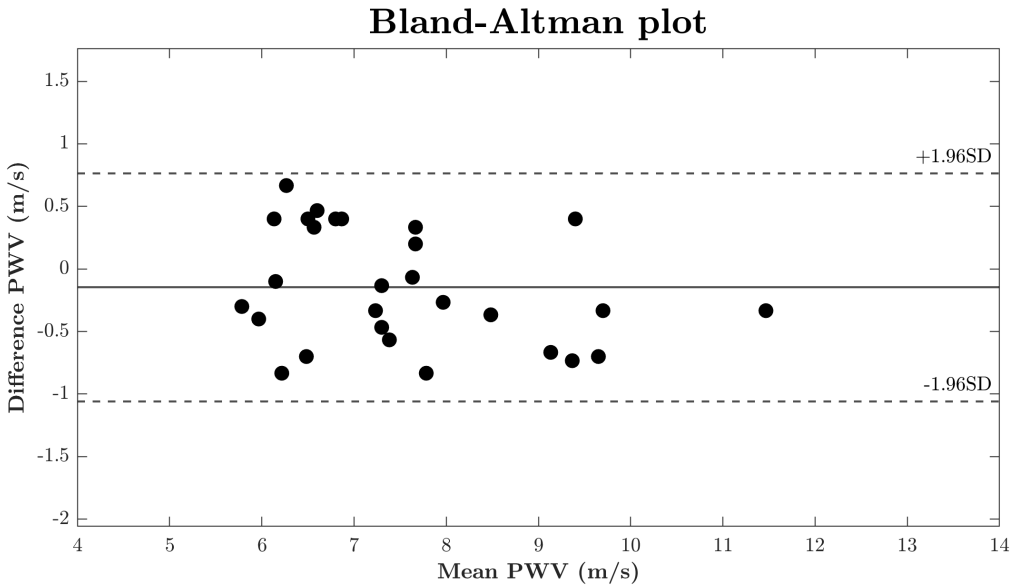

Figure 6.11: Bland-Altman plot that compares the performance of the suggested system and those offered by SphygmoCor®.

The Bland-Altman plot, which illustrates the agreement between results acquired from two different devices, is reported in Figure 6.11. The Bland-Altman plot makes it possible to spot any systematic discrepancy between the measurements (fixed bias or offset) or potential outliers. The estimated bias is represented by the mean difference, and the random fluctuations around this mean are measured by the differences' standard deviation. Calculating the 95% limits of agreement for each comparison (mean difference ± 1.96 of standard deviation of the differences) it is possible to understand how far apart measurements made using two different methods are typically more likely to be for most samples. Analyzing the graph, it is noticed a small offset error of -0.15 m/s and an acceptable standard deviation equal to 0.47 m/s. Furthermore, there is again a strong correlation and the absence of anomalous values (outliers).

The study and the results obtained showed how the proposed device's performance is consistent with the gold standard for PWV estimation since there is a strong linear correlation between the data obtained from the two devices, the offset error is very slight and the standard deviations are comparable. Furthermore, according to the Artery guidelines established by Wilkinson et al. [56], the accuracy of the presented device can be classified as excellent as the mean difference, compared to the gold standard for the PWV estimation, is less than 0.5 m/s (0.15 m/s in absolute value) and the differences' standard deviation is less than 0.8 m/s (0.47 m/s).

Chapter 7

Conclusion

The aim of this thesis is the development of an innovative clinical low-cost and wearable device for Pulse Wave Velocity (PWV) estimation using Force Sensing Resistor (FSR). Since FSR is a low-cost, flexible, and ultra-thin sensor and can interface with human skin, it is suitable to be used in a wearable application. A wearable approach is needed in this field to make the measurement less operator-dependent.

Furthermore, the purpose behind the research in this field is to increase the use of PWV assessment as an important parameter for assessing cardiovascular risk, independent of other widely recognized risk factors. To achieve this goal, a significant cost reduction on adoptable measuring devices is strongly required, while maintaining high standards of accuracy and reliability.

Both the issues of wearability and cost reduction have been addressed in this thesis, developing a wearable device engaging the operator only in positioning, and using low-cost components. Additionally, the capability of calibrating the system and operating at the point of maximum sensitivity permits the preservation of the quality of detected pulse wave signals based on the working condition, which differs between each subject.

The development of the device involved, in the first phase, the characterization of the various FSR product types available on the market and the selection of the best type of sensor for the application. Afterward, a read-out circuit has been studied and implemented around the chosen sensor, the FSR® 402 produced by Interlink Electronics. The read-out circuit has been developed on a Printed Circuit Board (PCB) to significantly reduce the dimension of the device. The PCB is linked with the Discovery Kit STM32F429I produced by STMicroelectronics, for which a specific firmware has been developed that enables the acquisition, calibration and transmission of pulse wave data to the PC. On the PC side, a Graphical User Interface (GUI) has been developed to visualize in real-time the signals taken from the carotid and femoral sites in a user-friendly way and with the possibility of

saving data for the subsequent PWV extraction carried out on MATLAB® by the intersecting tangent algoritmh.

Finally, the system has been validated on 28 volunteer subjects at "A.O.U. Città della Salute e della Scienza di Torino" and statistical analysis has been conducted to compare the obtained results with those provided by SphygmoCor®, which is considered the commercial gold standard of reference equipment in the industry.

The results obtained showed how the proposed device's performance is consistent with the gold standard since the two instruments exhibit strong similarities in PWV values. Furthermore, according to general guidelines, the accuracy of the presented device can be classified as excellent. These considerations show how devices using FSR have the potential to evolve into a highly affordable sensing technology that performs accurate, simple-to-conduct and wearable PWV estimation.

However, some types of improvements can be made to the system in order to have even more stable PWV values, lower standard deviations and make sensor use and wearability even more effective. A crucial point, considering the good results in the proposed device's performance, is the possibility of making the device more wearable by implementing Bluetooth communication technology, thus removing the clutter of the wires and allowing for easier use by the clinician. Furthermore, the conditioning circuit can be optimized, improving the gains implemented in the various amplification steps and adding a pre-filtering amplification of the instrumentation amplifier based on the amplitudes of the signals detected during use in the hospital environment. The implementation of the Graphical User Interface can also be improved, adding a criterion of maximum standard deviation after which the pulse wave signals cannot be acquired in order to improve the quality of the extracted signals and adding the possibility to generate a report with the PWV estimation value immediately after the GUI acquisition, without the need for MATLAB® post-processing. These system improvements would greatly increase the usability of the entire system by the clinical operator and, therefore, could lead to even more reliable PWV estimation results.

Appendix A

Schematic

In this section the read-out circuit diagram of the developed system is shown.

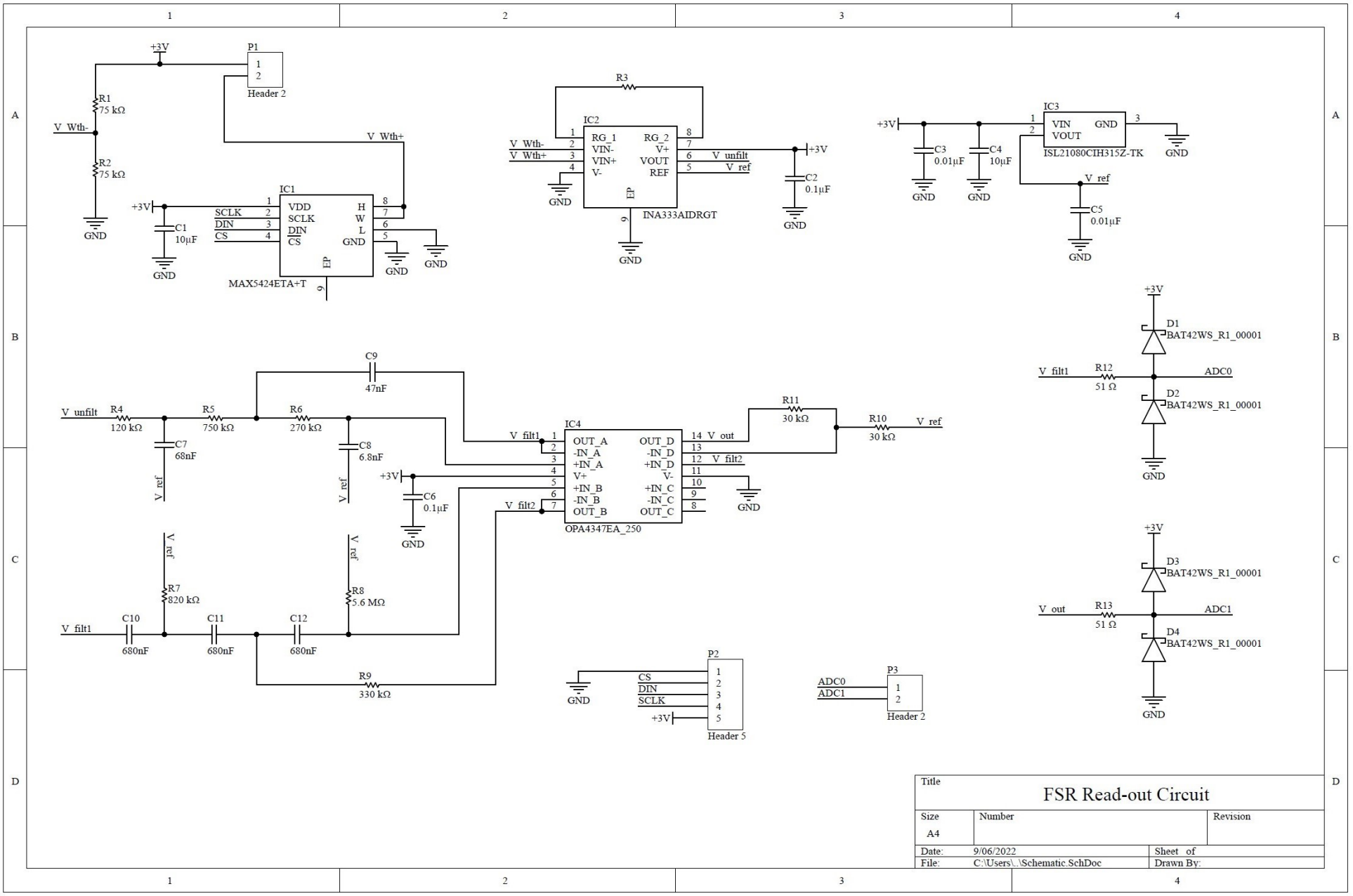
+3V
P1
Header 2
R1
75 kΩ
V_Wth-
V_Wth+
R2
75 kΩ
GND
IC1
SCLK
DIN
CS
VDD
SCLK
DIN
CS
H
W
L
GND
EP
MAX5424ETA+T
C1
10µF
R3
IC2
RG_1
VIN-
VIN+
V-
RG_2
V+
VOUT
REF
V_unfilt
V_ref
INA333AIDRGT
C2
0.1µF
IC3
VIN
GND
VOUT
ISL21080CIH315Z-TK
C3
0.01µF
C4
10µF
C5
0.01µF
V_ref
C9
47nF
V_unfilt
R4
120 kΩ
R5
750 kΩ
R6
270 kΩ
C7
68nF
C8
6.8nF
C6
0.1µF
IC4
OUT_A
-IN_A
+IN_A
V+
+IN_B
-IN_B
OUT_B
OUT_D
-IN_D
+IN_D
V-
+IN_C
-IN_C
OUT_C
V_filt1
V_filt2
V_out
R11
30 kΩ
R10
30 kΩ
OPA4347EA_250
R7
820 kΩ
R8
5.6 MΩ
R9
330 kΩ
C10
680nF
C11
680nF
C12
680nF
P2
CS
DIN
SCLK
Header 5
P3
ADC0
ADC1
Header 2
D1
BAT42WS_R1_00001
D2
BAT42WS_R1_00001
R12
51 Ω
D3
BAT42WS_R1_00001
D4
BAT42WS_R1_00001
R13
51 Ω
Title
FSR Read-out Circuit
Size
A4
Number
Revision
Date:
9/06/2022
Sheet of
File:
C:\Users\..\Schematic.SchDoc
Drawn By:

Bibliography

[1] World Health Organization. *Cardiovascular diseases (CVDs)*. 2022. URL: https://www.who.int/en/news-room/fact-sheets/detail/cardiovascular-diseases-(cvds) (cit. on p. 1).

[2] Norrving B. Mendis S. Puska P. *Global Atlas on cardiovascular disease prevention and control*. World Health Organization, 2011 (cit. on pp. 1, 21).

[3] Roth G.A. et al. «Global Burden of Cardiovascular Diseases and Risk Factors, 1990-2019: Update From the GBD 2019 Study». In: *Journal of the American College of Cardiology* 76.25 (2020), pp. 2982–3021. DOI: 10.1016/j.jacc.2020.11.010 (cit. on pp. 2, 23).

[4] Maxwell B. et al. «Spending on Cardiovascular Disease and Cardiovascular Risk Factors in the United States: 1996 to 2016». In: *Circulation* 144.4 (2021), pp. 271–282. DOI: 10.1161/CIRCULATIONAHA.120.053216 (cit. on pp. 2, 22).

[5] Webb D.J. Payne R.A. Wilkinson I.B. «Arterial Stiffness and Hypertension». In: *Hypertension* 55.1 (2010), pp. 9–14. DOI: 10.1161/HYPERTENSIONAHA.107.090464 (cit. on pp. 2, 24).

[6] Bryan W. et al. «2018 ESC/ESH Guidelines for the management of arterial hypertension». In: *European heart journal* 39.33 (2018), pp. 3021–3104. DOI: 10.1093/eurheartj/ehy339 (cit. on pp. 2, 23, 24, 32).

[7] Cardoso J. Pereira T. Correia C. «Novel Methods for Pulse Wave Velocity Measurement». In: *J Med Biol Eng* 35.5 (2015), pp. 555–565. DOI: 10.1007/s40846-015-0086-8 (cit. on p. 2).

[8] Paterson D.J. Herring N. *Introduction to Cardiovascular Physiology*. CRC Press, 2018 (cit. on pp. 4, 5, 7).

[9] Stanfield C.L. *Principles of Human Physiology*. Pearson, 2012 (cit. on pp. 5–7, 10, 11, 13, 16, 18).

[10] Freed J.K. Pagel P.S. «Chapter 4 - Cardiac Physiology». In: *Kaplan's Essentials of Cardiac Anesthesia (Second Edition)* (2018), pp. 62–79. DOI: 10.1016/B978-0-323-49798-5.00004-8 (cit. on p. 9).

[11] Athanasiou L.S. et al. «1 - Introduction». In: *Atherosclerotic Plaque Characterization Methods Based on Coronary Imaging* (2017), pp. 1–21. DOI: 10.1016/B978-0-12-804734-7.00001-4 (cit. on p. 9).

[12] Johns Hopkins Medicine. *Anatomy and Function of the Heart's Electrical System*. URL: https://www.hopkinsmedicine.org/health/conditions-and-diseases/anatomy-and-function-of-the-hearts-electrical-system (cit. on p. 12).

[13] Mayo Clinic. *Electrocardiogram (ECG or EKG)*. 2022. URL: https://www.mayoclinic.org/tests-procedures/ekg/about/pac-20384983 (cit. on p. 14).

[14] OER services. *Blood Flow, Blood Pressure, and Resistance*. URL: https://courses.lumenlearning.com/suny-ap2/chapter/blood-flow-blood-pressure-and-resistance-no-content (cit. on p. 17).

[15] Kędzia A. Gabryś E. Rybaczuk M. «Blood flow simulation through fractal models of circulatory system». In: *Chaos, Solitons & Fractals* 27.1 (2006), pp. 1–7. DOI: 10.1016/j.chaos.2005.02.009 (cit. on p. 17).

[16] Cardiovascular Physiology Concepts. *Vascular Compliance*. URL: https://www.cvphysiology.com/Blood%5C%20Pressure/BP004 (cit. on p. 19).

[17] American Society of Hematology. *Blood Basics*. URL: https://www.hematology.org/education/patients/blood-basics (cit. on p. 20).

[18] Gulec S. «Early diagnosis saves lives: focus on patients with hypertension». In: *Kidney Int Suppl* 3.4 (2011), pp. 332–334. DOI: 10.1038/kisup.2013.69 (cit. on p. 24).

[19] Maddury J. «Arterial Pulse». In: *Indian J Cardiovasc Dis Women* 110 (2017), pp. 2–99 (cit. on pp. 24, 25).

[20] Pinsky M.R. Esper S.A. «Arterial waveform analysis». In: *Best Pract Res Clin Anaesthesiol* 28.4 (2014), pp. 363–380. DOI: 10.1016/j.bpa.2014.08.002 (cit. on p. 25).

[21] Yartsev A. *Normal arterial line waveforms*. 2015. URL: https://derangedphysiology.com/main/cicm-primary-exam/required-reading/cardiovascular-system (cit. on pp. 27, 28).

[22] Milan A. et al. «Current assessment of pulse wave velocity: comprehensive review of validation studies». In: *J Hypertens* 37.8 (2019), pp. 1547–1557. DOI: 10.1097/HJH.0000000000002081 (cit. on pp. 29, 30, 33).

[23] «Reference Values for Arterial Stiffness' Collaboration. Determinants of pulse wave velocity in healthy people and in the presence of cardiovascular risk factors: 'establishing normal and reference values'». In: *Eur Heart J* 31.19 (2010), pp. 2338–2350. DOI: 10.1093/eurheartj/ehq165 (cit. on p. 29).

[24] Patrick S. et al. «How to Measure Arterial Stiffness in Humans». In: *Arteriosclerosis, thrombosis, and vascular biology* 40.5 (2020), pp. 1034–1043. DOI: 10.1161/ATVBAHA.119.313132 (cit. on p. 30).

[25] Nabeel P.M. et al. «Local Pulse Wave Velocity: Theory, Methods, Advancements, and Clinical Applications». In: *IEEE Rev Biomed Eng* 13 (2020), pp. 74–112. DOI: 10.1109/RBME.2019.2931587 (cit. on p. 30).

[26] Boutouyrie P. et al. «Assessment of pulse wave velocitys». In: *Artery Research* 3.1 (2006), pp. 3–8. DOI: 10.1016/j.artres.2008.11.002 (cit. on p. 32).

[27] Westenberg J.J. et al. «Bramwell-Hill modeling for local aortic pulse wave velocity estimation: a validation study with velocity-encoded cardiovascular magnetic resonance and invasive pressure assessment». In: *J Cardiovasc Magn Reson* 14.1 (2012), p. 2. DOI: 10.1186/1532-429X-14-2 (cit. on p. 32).

[28] Godia E.C. et al. «Carotid artery distensibility: a reliability study». In: *J Ultrasound Med* 26.9 (2007), pp. 1157–65. DOI: 10.7863/jum.2007.26.9.1157 (cit. on p. 32).

[29] Van Hout M.J. et al. «Normal and reference values for cardiovascular magnetic resonance-based pulse wave velocity in the middle-aged general population». In: *J Cardiovasc Magn Reson* 23.1 (2021), p. 46. DOI: 10.1186/s12968-021-00739-y (cit. on p. 32).

[30] Webb D.J. Wilkinson I.B. Cockcroft J.R. «Pulse wave analysis and arterial stiffness». In: *J Cardiovasc Pharmacol* 32 (1998) (cit. on p. 32).

[31] Saksena F. B. Ranganathan N. Sivaciyan V. *The Art and Science of Cardiac Physical Examination: With Heart Sounds and Pulse Wave Forms on CD*. Humana Press, 2007 (cit. on p. 33).

[32] AtCor. *SphygmoCor® Platform*. URL: https://atcormedical.com/technology/sphygmocor/ (cit. on p. 33).

[33] DiaTecne. *PulsePen®*. URL: https://www.pulsepen.com/pulsepen.html (cit. on p. 34).

[34] Alam Medical. *Complior Analyse*. URL: http://www.complior.com/products (cit. on p. 34).

[35] Buraioli I. et al. «A New Noninvasive System for Clinical Pulse Wave Velocity Assessment: The Athos Device». In: *IEEE Trans Biomed Circuits Syst* 15.1 (2021), pp. 133–142. DOI: 10.1109/TBCAS.2021.3058010 (cit. on pp. 34, 35, 73).

[36] STMicroelectronics. *LPS35HW MEMS pressure sensor : 260-1260 hPa absolute digital output barometer with water-resistant package* (cit. on p. 35).

[37] Sukor J.A. Sadun A. Jalani J. «Force Sensing Resistor (FSR): a brief overview and the low-cost sensor for active compliance control». In: *First International Workshop on Pattern Recognition* (2016). DOI: 1001112.10.1117/12.2242950 (cit. on p. 40).

[38] Deshmukh M. Sundar A. Das C. «Novel Applications of Force Sensing Resistors in Healthcare Technologies». In: *Healthy World Conference* (2015). DOI: 10.13140/RG.2.1.3967.9841 (cit. on p. 40).

[39] Farella E. Giovanelli D. «Force Sensing Resistor and Evaluation of Technology for Wearable Body Pressure Sensing». In: *Journal of Sensors* (2016). DOI: 1-13.10.1155/2016/9391850 (cit. on p. 40).

[40] Laber J. Gujarati Y. Thamma R. «Technologies for Force/Torque Sensor». In: *IJISET - International Journal of Innovative Science, Engineering & Technology* 7.12 (2020) (cit. on p. 42).

[41] Jun M.H. et al. «Pulse wave response characteristics for thickness and hardness of the cover layer in pulse sensors to measure radial artery pulse». In: *BioMed Eng OnLine* 17.118 (2018). DOI: 10.1186/s12938-018-0551-z (cit. on p. 45).

[42] Interlink Electronics. *FSR 400®*. URL: https://www.interlinkelectronics.com/fsr-400 (cit. on p. 45).

[43] Interlink Electronics. *FSR 402®*. URL: https://www.interlinkelectronics.com/fsr-402 (cit. on p. 45).

[44] Tekscan. *FlexiForce A201 Sensor*. URL: https://www.tekscan.com/products-solutions/force-sensors/a201 (cit. on p. 45).

[45] Tekscan. *FlexiForce HT201 Sensor*. URL: https://www.tekscan.com/products-solutions/force-sensors/ht201 (cit. on p. 45).

[46] Lebossé C. et al. «Modeling and Evaluation of Low-Cost Force Sensors». In: *Robotics, IEEE Transaction* 27 (2011), pp. 815–822. DOI: 10.1109/TRO.2011.2119850 (cit. on p. 48).

[47] Lebossé C. et al. «Nonlinear modeling of low cost force sensors». In: *IEEE International Conference on Robotics and Automation* (2008), pp. 3437–3442. DOI: 10.1109/ROBOT.2008.4543736 (cit. on p. 48).

[48] STMicroelectronics. *Discovery kit with STM32F429ZI MCU* (cit. on p. 51).

[49] STMicroelectronics. *STM32F429ZI*. URL: https://www.st.com/en/microcontrollers-microprocessors/stm32f429zi.html (cit. on p. 51).

[50] Mishra S. et al. «Chapter 10 - Sensor Interfaces». In: *System on Chip Interfaces for Low Power Design* (2016), pp. 331–344. DOI: 10.1016/B978-0-12-801630-5.00010-4. (cit. on p. 53).

[51] Renesas. *ISL21080; 300nA NanoPower Voltage References* (cit. on p. 54).

[52] Maxim Integrated. *256-Tap, Nonvolatile, SPI-Interface, Digital Potentiometers* (cit. on p. 56).

[53] Texas Instruments. *INA333 Micro-Power (50μA), Zero-Drift, Rail-to-Rail Out Instrumentation Amplifier* (cit. on p. 57).

[54] Burr-Brown Products from Texas Instruments. *microPower, Rail-to-Rail Operational Amplifiers* (cit. on p. 57).

[55] Chiu Y.C. et al. «Determination of pulse wave velocities with computerized algorithms». In: *Am Heart J* 121.5 (1991), pp. 1460–1470. DOI: 10.1016/0002-8703(91)90153-9 (cit. on p. 73).

[56] Wilkinson I.B. et al. «ARTERY Society guidelines for validation of non-invasive haemodynamic measurement devices: Part 1, arterial pulse wave velocity». In: *Artery Research* 4.2 (2010), pp. 34–40. DOI: 10.1016/j.artres.2010.03.001 (cit. on p. 83).